The Dissertation Committee for Kevin Scott Melin
certifies that this is the approved version of the following dissertation:

Controlling the Dimensionality of the Stern-Gerlach Effect for Neutral Atom Manipulation

Committee:

Mark G. Raizen, Supervisor

John W. Keto

Greg O. Sitz

Qian Niu

Pawan Kumar

Controlling the Dimensionality of the Stern-Gerlach Effect for Neutral Atom Manipulation

by

Kevin Scott Melin

DISSERTATION

Presented to the Faculty of the Graduate School of

The University of Texas at Austin

in Partial Fulfillment

of the Requirements

for the Degree of

DOCTOR OF PHILOSOPHY

THE UNIVERSITY OF TEXAS AT AUSTIN

May 2019

For my parents.

Thank you for the many years of love and support.

Acknowledgments

First and foremost, I would like to thank my adviser Mark Raizen. I am immensely grateful for all of the support, encouragement, and mentorship that he has provided over the years to not only me but also the entire group. Since I have known Mark I have been continuously impressed with his ability to motivate his students to excel in both the laboratory and also their post-graduate endeavors. He understands and is careful to apply the appropriate balance of direction, guidance, suggestion, and finally laissez faire. His concern for the group's well-being has always extended beyond their academic lives to also include their personal lives. Having had the privilege of being a member of the Raizen group for longer than most, I will always be grateful to Mark for the countless opportunities, experiences, and knowledge that he has provided.

When I first joined the group as a senior undergraduate I was placed under the guidance of Tom Mazur to help develop the recently proposed isotope separation method, MAGIS. Tom's diligence and attention to detail as an experimentalist has been a standard that I continue to strive to achieve. It would not be hyperbole to ascribe the bulk of my experimental skills to his instruction in the brief time that I worked directly with him. Some of the many skills he passed on include vacuum techniques, custom electronics, Labview automation, CAD design, and machining. Despite having graduated five years ago, I continue to make reference of his work

and fondly speak of him with the current group members.

Early in the spring of 2013 after the success of the isotope separation experiment, I transitioned to the optical tweezer experiment to work under the tutelage of Akarsh Simha. Akarsh and I are of similar minds and we both naturally assumed a very late working schedule that only graduate school could accommodate. We spent many nights discussing all manner of topics ranging from physics to internet memes. Even after Akarsh discovered his calling in theory rather than experiment, he has continued to be a great friend long after his graduation.

I was fortunate to again realize the successful completion of yet another experiment before returning to the realm of vacuum systems in the fall of 2013 to enhance the entrainment of lithium into supersonic beams. At approximately the same time a former student, Isaac Chavez, returned from a job at Intel to resume his graduate career. Isaac tutored me on the operation of the Even-Lavie valve that I continued to use daily for the remainder of my Ph.D. research. Though he stayed only for a year, I miss his humor and expertise. After Isaac's departure I became the senior student on my experiment which required me to now manage a growing team of talented fellow graduate students. Because this was my first experience in such a role, Jianyong Mo was very influential in aiding in my transition by conveying a leader's responsibilities and duties. However, this did not overshadow his friendship during this period.

In the 2014 timeframe, while optimizing lithium entrainment and dodging exploding IGBTs, three people, Karl Burkhardt, Lukas Gradl, and Yu Lu, joined the lab and became my fellow colleagues. Karl's expertise in ion trapping provided a

significant boost to my confidence when I was becoming familiar with the details of AMO physics. Lukas initially joined the lab as a one-year research exchange student from the University of Würzburg, Germany. I was happy to see him remain at UT to obtain a Master's degree and work with us on novel entrainment methods. I continue to be impressed with his performance as he now works at the Pointsman Foundation to deploy the isotope separation methods, both new and old, on an industrial scale that Tom and I merely tested a few years earlier. Finally, Yu has been my main partner in the experiment for the past four years. He has been there at all the stages of our experiment: laser ablation of lithium, pulsed ribbon entrainment, lithium puddle vaporization, construction of the adiabatic decelerator, implementation of the cryocooler, and finally the demonstration of a one-dimensional kick. Needless to say, I have shared many long hours of sweat and solder with him and I am grateful to have had a partner as reliable and hard-working as him. It has truly been a pleasure to work alongside him and watch him develop into a formidable programmer. I wish him all the best when he returns to China to work on artificial intelligence.

Much of the last few years of my stay was funded by the W.M. Keck Foundation. This large influx of money into our group enabled us to expand and include a couple of post-docs that have been a great help during my final years with the group. Yu and I worked closely with Lichung Ha for a year as we struggled to prove the operation of the adiabatic decelerator. I really appreciated his methodical approach to experimental physics that was lacking in some of my earlier efforts before his arrival. Pavel Nagornykh was instrumental in our continuing journey to demonstrate magneto-optical cooling. He had an uncanny ability to materialize before us near

the end of the day and encourage us to work just a *little* more. We spent many late nights enjoying random discussions, watching odd Youtube videos, and squinting at questionable one-dimensional kick data. A large portion of my dissertation benefits from the initial calculations and simulations that Pavel compiled.

The Keck funding also provided us with two additional graduate students: Logan Hillberry and Yi Xu. Both are exceedingly capable and give me great hope for the future of our project. It has been a joy passing on the accumulated knowledge of those that taught me to this new generation of graduate students. I am confident that their dissertations will one day document several cycles of magneto-optical cooling.

Though I only directly worked with those listed above there have been many others on different projects in the Raizen group with whom I have interacted and spent many countless hours enjoying their camaraderie. I would like to thank Jamie Gardner and Jordan Zesch for all of the book recommendations and random rants. Erik Anciaux provided a diverse mix of random jokes, quality high-fives, and, most importantly, an impressive intuition for AMO physics. Georgios has been a great friend to bounce ideas with and discuss any troubles we experienced over the years. I appreciate Igal Bucay's continued insistence to one day drag me onto a racquetball court.

Much of the vacuum chambers, equipment, and electronics we designed in the lab were machined, fixed, or tested by the Physics machine shop, cryo shop and electronics shop. Working with the machinists was always a joy as we brainstormed how to convert my elaborate CAD drawings into reality. In particular I want to thank Jack Clifford, the supervisor for the student machine shop, for his insight and

friendliness.

Finally I would like to thank Olga Vera for the many years of help in navigating the bureaucratic and administrative complexities of UT. Whenever I had difficulty with paperwork or an odd question, she always knew just who to ask to obtain a quick answer. Though she retired only a few months ago, we already feel her absence in both the group and the Center for Nonlinear Dynamics.

I know there are many undergraduates, faculty, and administrative staff that have also contributed to my success and attainment of my doctorate. Although not explicitly called out here, I would like to express my thanks to them.

Controlling the Dimensionality of the Stern-Gerlach Effect for Neutral Atom Manipulation

Publication No. _____

Kevin Scott Melin, Ph.D.
The University of Texas at Austin, 2019

Supervisor: Mark G. Raizen

The Stern-Gerlach experiment, performed in 1922, is a seminal work of modern physics. It was the experiment that first showed the quantized nature of the spin of an atom. This dissertation returns to this early experiment and describes the design, construction, and characterization of a variation that produces a one-dimensional Stern-Gerlach effect, or 1D kick, on a beam of neutral lithium atoms. Our technique relies on the combination of a magnetic field gradient and a strong bias field to generate a one-dimensional force on lithium entrained in a supersonic helium beam. By adjusting the bias field via variable, pulsed currents, we demonstrate the transition from a purely dispersive kick to a one-dimensional kick where off-axis heating of the beam has been eliminated.

Pure one-dimensional forces enable access to new atomic and molecular cooling methods that can replace or supplement existing techniques to produce larger samples of cold atoms currently limited by evaporative cooling. Simulations suggest that the proposed magneto-optical cooling utilizing one-dimensional kicks will

increase the total number of atoms in cold atom traps by orders of magnitude, thus opening applications such as high flux atom lasers and more sensitive atom interferometry.

Table of Contents

List of Tables

List of Figures

Chapter 1

A One-dimensional Magnetic Kick

The deflection of an atomic beam in an inhomogeneous magnetic field, known as the Stern-Gerlach effect, is a textbook experiment [1] at the foundation of modern physics. In the original work [2], performed by Otto Stern and Walter Gerlach in 1922, a collimated beam of silver atoms was passed through a permanent, spatially varying magnetic field (see Figure 1.1). The deflected trajectories detected on a screen downstream showed two distinct lines, thereby demonstrating the quantized nature of atomic angular momentum and the existence of electron spin.

The effect has since found application in atom optics [4, 5, 6, 7, 8, 9, 10], atom interferometry [11, 12], and isotope separation [13]. The collimating slit used in the original experiment minimized the beam divergence expected from Maxwell's equations which forbid a purely one-dimensional magnetic field gradient. Creating a one-dimensional Stern-Gerlach effect has practical implications for the ability to control atoms with magnetic fields [14] and the design of "flat" mirrors capable of reflecting particles specularly without the dispersion of wave vectors [4, 5, 6]. Another exciting application is the potential to simulate microgravity conditions. Using a one-

The experiment, analysis, and results presented in this dissertation substantially expand upon the body of work documented in our recently published paper [3]. Furthermore, the introductory paragraphs here are based on the paper's introduction.

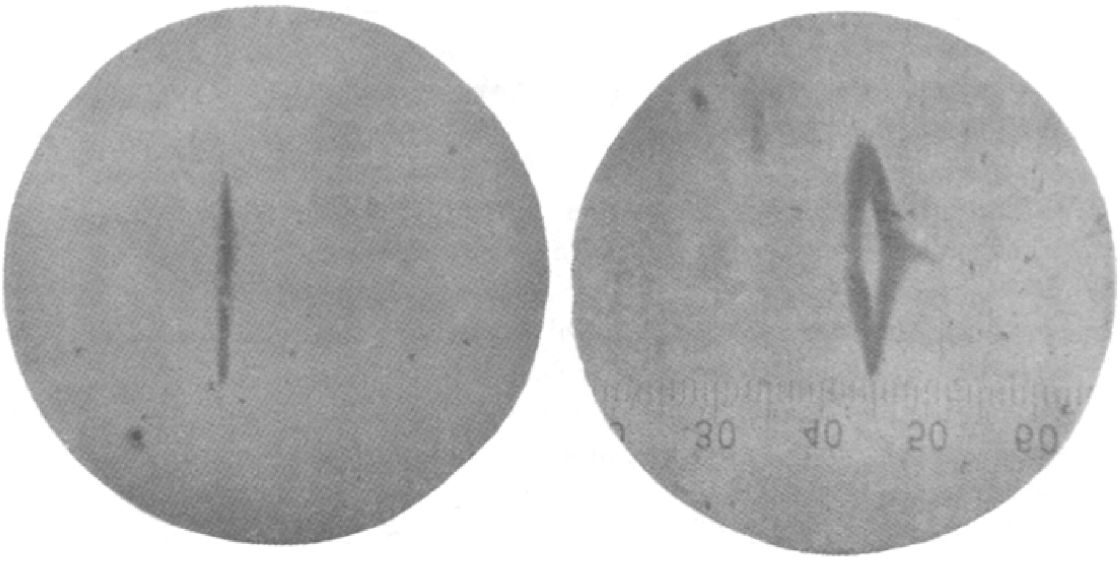

Figure 1.1: Results of the original Stern-Gerlach experiment where the magnetic deflection of silver atoms was shown to be quantized. On the left is an image that shows an exposure of the silver beam on the detector plate (black silver sulfide) without magnetic fields. On the right the inhomogeneous field was included and split the silver beam into two distinct lines [2].

dimensional force to cancel gravity, one may conduct non-contact studies of levitated magnetic nanoparticles, improve loading of atoms into optical dipole traps [15], and further research of cold atoms in force-free environments without leaving Earth [16]. Finally, and of particular interest to our group, the proposed method of magneto-optical cooling, which relies on cycles of optical pumping and one-dimensional pulsed magnetic kicks, will compress atomic phase space one dimension at a time without loss of atoms [17].

A one-dimensional Stern-Gerlach effect can be created if we consider a cloud of atoms each with a magnetic dipole moment $\boldsymbol{\mu}$ in the presence of a spatially dependent magnetic field $\mathbf{B}(\mathbf{r})$. Atoms will experience the combination of rectilinear motion and precession of the magnetic moment caused by the force $\nabla(\boldsymbol{\mu} \cdot \mathbf{B})$ and torque $\boldsymbol{\mu} \times \mathbf{B}$, respectively. For sufficiently fast precession ($\gtrapprox$ 100 MHz for fields greater than 10 G), an adiabatic approximation is valid in which the magnetic moment is taken to be always parallel to the magnetic field. In this approximation the average force $\mathbf{F} = \mu \nabla |\mathbf{B}|$ determines the motion of each atom, which indicates the existence of magnetic field configurations that provide an approximately one-dimensional kick over the finite extent of the atomic cloud. One such configuration was considered in the design of magnetic mirrors [5, 7]. An alternative configuration that we employ is the sum of a strong bias field and a gradient. In this case, as long as the size of the atomic cloud d satisfies the condition $|d \nabla B| \ll B_{\text{bias}}$, where $B = |\mathbf{B}| = |\mathbf{B}_{\text{bias}} + \mathbf{B}_{\text{gradient}}|$ and $B_{\text{bias}} = |\mathbf{B}_{\text{bias}}|$, then all atoms in the cloud experience the same force and undergo a *one-dimensional* kick. Additionally, for an atomic beam experiment like the original Stern-Gerlach demonstration, the above condition is not

satisfied when the cloud enters or exits the field region. One straightforward solution to this problem is to pulse the fields only while the cloud is centered in the kicking region.

In this dissertation, we demonstrate a quasi-one-dimensional Stern-Gerlach effect on a supersonic beam of lithium-7 atoms with a pulsed magnetic field gradient plus a strong bias.

1.1 A closer inspection of the Stern-Gerlach experiment

Before delving into the details of the Stern-Gerlach effect it is instructive to first review the attributes of magnetic moments. Magnetic moments, or more specifically, magnetic dipole moments are the magnetic analog of the electric dipole. For simplicity, consider two magnetic monopoles[1] of charge $\pm m$ which are rigidly connected and separated by a vector $\mathbf{d}$. Exposing this dipole to a magnetic field $\mathbf{B}(\mathbf{r})$ will create a total force

$$\mathbf{F} = m\mathbf{B}(\mathbf{r}_1) - m\mathbf{B}(\mathbf{r}_2) \tag{1.1}$$

where $\mathbf{r}_1$ and $\mathbf{r}_2$ are the positions of the two charged monopoles. In the absence of a inhomogeneous magnetic field there will be no net force since the monopoles act equally and oppositely in the field. Reducing the separation between the monopoles and defining $\boldsymbol{\mu} \equiv m\mathbf{d}$, we can approximate the force as

$$\mathbf{F} = (\boldsymbol{\mu} \cdot \nabla)\mathbf{B}\,. \tag{1.2}$$

[1] though never observed in nature

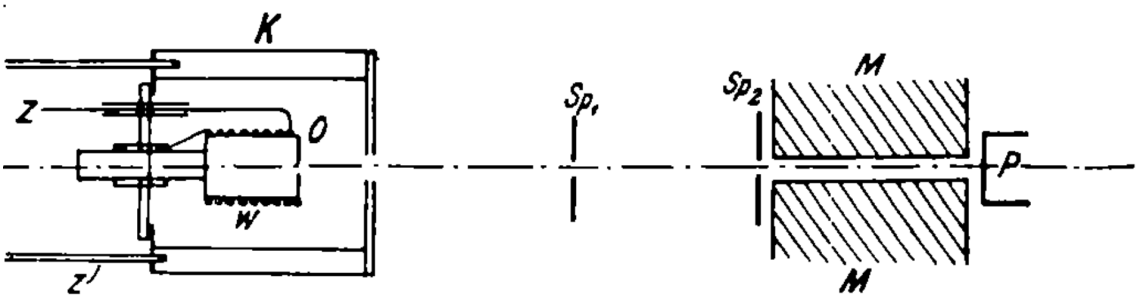

Figure 1.2: Layout of the original Stern-Gerlach experiment [18]. A furnace (O) on the left is heated by a resistive wire (W) to evaporate and produce an effusive beam of silver atoms. Collimation of the beam was done with a 1 mm aperture (Sp_1) and a rectangular 0.8 mm $\times$ $\sim$0.04 mm slit (Sp_2). The collimated beam passes through the magnet (M) before being collected on a cooled detection plate (P).

Under classical physics the magnetic moment is free to assume any orientation with respect to a magnetic field. This would imply a continuous range of possible forces. This assumption, however, is not valid when considering the behavior of atomic magnetic moments. Stern and Gerlach showed in their seminal work in 1922 [2] that the magnetic moment is quantized with respect to the magnetic field. An image of their results is shown in Figure 1.1 where a beam of silver was passed through two magnets that created an inhomogeneous magnetic field. Classically, we would have expected a broadened distribution, but they observed two clearly separated streaks hinting at the quantization of the spatial orientation of angular momentum.

The fact that $\boldsymbol{\mu}\cdot\mathbf{B}$ assumes only discrete values has immediate implications for the control of atoms. Using the methods to be described in Chapter 3 we can optically prepare the state of atoms such that they will behave in a very specific way under a magnetic gradient. More precisely, we write down the interaction Hamiltonian of

the atom in a magnetic field as

$$H_{int} = -\boldsymbol{\mu} \cdot \mathbf{B}\,. \tag{1.3}$$

The semi-classical force can then be easily expressed as

$$\mathbf{F} = -\nabla U = \nabla \langle \boldsymbol{\mu} \cdot \mathbf{B} \rangle = \langle \boldsymbol{\mu} \rangle \nabla B \tag{1.4}$$

where B is the magnitude of the magnetic field and orientation of $\boldsymbol{\mu}$ has been absorbed into the expectation value of $\langle \boldsymbol{\mu} \rangle$. Atoms whose magnetic moments are aligned with the field such that $\langle \mu \rangle > 0$ will be attracted by strong magnetic fields and henceforth denoted as high-field-seeking (HFS) atoms. We focus on these atoms for our experiment as one of the two ^{7}Li $^2S_{1/2}$ ground states that is purely HFS (see Chapter 3 for more details).

An interesting detail of the original Stern-Gerlach experiment is that the inhomogeneous magnetic field also imparts large forces along the axis orthogonal to the propagation. This is simply a side-effect of Maxwell's equations where $\nabla \cdot B = 0$ implies that the instant a nonuniform field is introduced, gradients, and thus forces, must exist along another axis. This important point is often neglected in simple descriptions. For example, Feynman [19] states

> *The beam of silver atoms was directed right along this sharp edge, so that the atoms would feel a vertical force in the inhomogeneous field. A silver atom with its magnetic moment directed horizontally would have no force on it and would go straight past the magnet.*

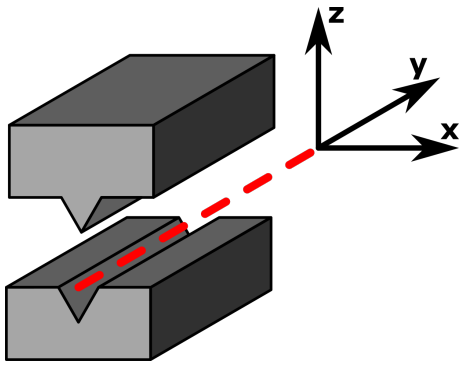

Figure 1.3: Stern-Gerlach magnet arrangement. The silver atoms propagate along the y-axis.

At first glance his statement appears incorrect, but giving Feynman the benefit of the doubt, we assume that his comments are on the *time-averaged* forces rather than any forces. Many have discussed these time-averaged forces in either the semi-classical limit [20, 21, 22] or the fully quantum equivalent [1]. The semi-classical treatment will be sufficient for our system and we will follow the logic presented in the aforementioned references.

1.1.1 Larmor precession

Let us assume a similar magnetic arrangement as that of Stern and Gerlach, shown in Figure 1.3, which produces a magnetic field $\mathbf{B} = \mathbf{B}(x, z)$ as long as we are not near the ends of the magnets. Gauss's law for magnetism, $\nabla \cdot \mathbf{B} = 0$, would then yield

$$\partial_x B_x = -\partial_z B_z \quad \text{and} \quad \partial_x B_z = -\partial_z B_x \,. \tag{1.5}$$

Inserting these two equations into Equation 1.4 we obtain

$$\mathbf{F} = (\mu_x \partial_x B_x + \mu_z \partial_x B_z,\, 0,\, \mu_x \partial_z B_x + \mu_z \partial_z B_z) \tag{1.6}$$

where the force of the x and z components are clearly of similar magnitude. In order to accurately describe the the motion of the atoms, we must also include the torque, $\boldsymbol{\tau} = \boldsymbol{\mu} \times \mathbf{B}$, the atoms experience. Torque, being an axial vector, will create a force orthogonal to $\boldsymbol{\mu}$ and result in a precession of the magnetic moment around the magnetic field $\mathbf{B}$. Noting that the change in the spin $\mathbf{S}$ can be expressed as

$$\dot{\mathbf{S}} = \boldsymbol{\omega} \times \mathbf{S} \tag{1.7}$$

where $\boldsymbol{\omega}$ is the angular velocity with which the spin precesses, we can write the precession of the magnetic moment as

$$\dot{\boldsymbol{\mu}} = \boldsymbol{\omega}_{\mathbf{L}} \times \boldsymbol{\mu} \tag{1.8}$$

where $\omega_{\mathbf{L}} = (\mu_B g_S/\hbar)\mathbf{B}$ using Equation 3.16. This is commonly known as the Larmor precession frequency. It is convenient to pause here and mention an important concept known as adiabatic following. Once an atom has assumed a particular angular momentum eigenstate it will reside in this state indefinitely. For slow variations in the magnetic field the atom will constantly reorient itself maintaining the state it has assumed. This can be stated more rigorously in terms of the Larmor frequency

$$\omega_L \gg \left| \frac{d}{dt}\left(\frac{\mathbf{B}}{B}\right)\right| . \tag{1.9}$$

Only when the direction of the magnetic field changes abruptly at timescales comparable to the Larmor frequency will the atoms leave their eigenstate.

Returning to Equation 1.8 and expanding the general solutions of this equa-

tion we obtain expressions for the magnetic moment projections:

$$\mu_x(t) = \mu_x(0)\left[1 - \frac{2\omega_z^2}{\omega^2}\sin^2\left(\frac{\omega t}{2}\right)\right] - \frac{\omega_z}{\omega}\mu_y(0)\sin(\omega t) + \frac{2\omega_x\omega_z}{\omega^2}\mu_z(0)\sin^2\left(\frac{\omega t}{2}\right),$$
$$\mu_y(t) = \mu_y(0)\cos(\omega t) + \frac{\omega_z\mu_x(0) - \omega_x\mu_z(0)}{\omega}\sin(\omega t),$$
$$\mu_z(t) = \mu_z(0)\left[1 - \frac{2\omega_x^2}{\omega^2}\sin^2\left(\frac{\omega t}{2}\right)\right] - \frac{\omega_x}{\omega}\mu_y(0)\sin(\omega t) + \frac{2\omega_x\omega_z}{\omega^2}\mu_x(0)\sin^2\left(\frac{\omega t}{2}\right).$$

Inserting these expressions into Equation 1.6 and taking the time average, we can express the force that the atoms will experience when traveling between the magnets:

$$\begin{aligned} F_x^{avg} &= \left[\mu_x(0)\left(1 - \frac{\omega_z^2}{\omega}\right) + \mu_z(0)\frac{\omega_x\omega_z}{\omega^2}\right]\partial_x B_x \\ &\quad + \left[\mu_z(0)\left(1 - \frac{\omega_x^2}{\omega}\right) + \mu_x(0)\frac{\omega_x\omega_z}{\omega^2}\right]\partial_x B_z \\ F_z^{avg} &= \left[\mu_z(0)\left(1 - \frac{\omega_x^2}{\omega}\right) + \mu_x(0)\frac{\omega_x\omega_z}{\omega^2}\right]\partial_z B_z \\ &\quad + \left[\mu_x(0)\left(1 - \frac{\omega_z^2}{\omega}\right) + \mu_z(0)\frac{\omega_x\omega_z}{\omega^2}\right]\partial_z B_x \end{aligned} \tag{1.10}$$

with F_y vanishing. In the case of a narrow beam propagating in the plane of the y, z-axis, the ω_x, $\partial_x B_z$, and $\partial_z B_x$ terms will also vanish yielding

$$\mathbf{F}(t) = \Big(-\mu_x(0)\cos(\omega t) + \mu_y(0)\sin(\omega t)\,,\,0\,,\,\mu_z(0)\Big)\partial_z B_z \tag{1.11}$$

where $\omega = \omega_z$. In their original experiment Stern and Gerlach had magnetic fields of order 1000 G [23] which would produce a precession of the magnetic moment at ~ 0.1 THz. Considering the length of the actual magnets, we can estimate the effect that the field has on the change in momentum of the beam:

$$\begin{aligned} \Delta\mathbf{p} &= \int_0^\tau \mathbf{F}(t)dt \\ &= \Big(-\frac{\mu_x(0)}{\omega\tau}\sin(\omega\tau) + \frac{\mu_y(0)}{\omega\tau}(1 - \cos(\omega\tau)\,,\,0\,,\,\mu_z(0)\Big)\partial_z B_z \end{aligned} \tag{1.12}$$

where τ is the length of time the atoms are within the bounds of the magnets. Noting that the x-component is smaller than the z-component by a factor of $\omega\tau$ we can safely say that the net force on the atoms in the transverse x-axis is negligible and essentially 0 for any macroscopic length scale or beam velocities. At first glance, it appears that this simple analysis results in a *one-dimensional force*.

1.1.2 Inclusion of a magnetic bias

In estimating the momentum change and Larmor frequency, we lost much of the richness that the original Stern-Gerlach experiment has to offer. Exploring some of the off-axis effects will provide a natural motivation for the concept of a one-dimensional momentum kick. Let us rewind and return to Equation 1.10.

In general the terms ω_x, $\partial_x B_z$, and $\partial_z B_x$ do not vanish when we move off-axis. While the beam does produce directional motion of the cloud center, the nonzero terms effectively heat or spread the beam. We have naively assumed the magnetic field to be too simple and it would be instructive to look more closely at the construction of the original magnets. While others were attempting to reproduce the results of Stern and Gerlach they note the specific construction of the magnets. Taylor writes [24, 21]

> *A large Dubois type magnet, possibly a duplicate of Stern and Gerlach's, was used to produce the magnetic field. The apparatus for formation, deflection, and detection of the atomic rays was suspended between the flat pole pieces of this magnet... The auxiliary pole pieces for producing the inhomogeneous field were of soft iron... One pole piece was a 60'*

knife edge, the other slotted... Magnetic measurements showed the field produced and the inhomogeneity of the field to be closely that used by Stern and Gerlach...

The implication of this description is that, in order to recreate the original setup, Stern and Gerlach used the auxiliary pole pieces to create the inhomogeneous field component $\mathbf{B}(x, z)$ that we already discussed. They also used a large magnet to produce a near constant field B_0. Together this defines a new field

$$\mathbf{B}_t = \mathbf{B} + B_0 \hat{\mathbf{k}} \,. \tag{1.13}$$

Using this newly constructed field, Equation 1.8 which describes the precession will simplify greatly if $|B_0| \gg |B|$. This allows us to approximate the total magnetic field as just the constant bias ($B_t \approx B_0$). Making this simplification, Equation 1.8 reduces to

$$\dot{\boldsymbol{\mu}} = \left(\frac{g_s \mu_B}{\hbar} B_0\right) \hat{\mathbf{k}} \times \boldsymbol{\mu} \tag{1.14}$$

which also produces the simpler force equations of Equation 1.11. For a sufficiently large bias, the force applied in this case is one-dimensional.

Equation 1.13 is the fundamental basis of the remainder of this dissertation. The two terms, $\mathbf{B}$ and $B_0 \hat{\mathbf{k}}$, address two key items that we require for our definition of one-dimensionality. The first is that $\mathbf{B}$ is the arbiter of directed motion through the force $\mathbf{F} = \langle \boldsymbol{\mu} \rangle \nabla |\mathbf{B}| = \mu_B g_J m_J \nabla B$ which will be used to create a quick impulse, or 'kick,' on the atoms. The second is that the bias $\mathbf{B}_0$ controls the degree of beam heating. At a high bias we expect a kicked cloud to be translationally displaced without influencing its expansion.

We implement a system of pulsed electromagnetic coils to variably select the bias field strength during a magnetic kick and demonstrate a *one-dimensional Stern-Gerlach effect*.

Chapter 2

Atomic Beams

Atomic beams are the foundation of many of the experiments in our lab and are the starting point of the experiment covered in this dissertation. Being such an integral component to all that follows, it is useful to provide a basic description of ideal gases and their behavior in different regimes.

The simplest beam we can envision is that of an effusive beam created by releasing a gas through a hole into vacuum. The source could be a heated vapor oven or a highly pressurized gas line; however, generally all that is required is higher pressure gas flowing to a lower pressure region through an opening. We can divide the characteristics of the gas into two regimes by comparing the mean free path $\overline{\Lambda}$, the average distance between collisions of the gas, to that of the opening diameter d. The mean free path is given by

$$\overline{\Lambda} = \frac{1}{1.4761\rho\,\sigma} \approx \frac{1}{\rho\,\sigma\sqrt{2}}\,, \tag{2.1}$$

where ρ is the particle number density and σ is the collision cross section of the particles in the hard sphere model [25, 26, 27]. When the dimensions of the mean free path are much larger than that of the opening, $\overline{\Lambda} > d$, the gas is said to be in the effusive regime. In the case of an ideal gas the mean free path can be restated as

$$\overline{\Lambda} \approx \frac{k_B T}{P\sigma\sqrt{2}}\,, \tag{2.2}$$

where P is the pressure, k_B is the Boltzmann constant, and T is the temperature of the gas in Kelvin. The speed distribution within the reservoir will follow the Maxwell-Boltzmann distribution [28]

$$f(v) = \frac{4}{\sqrt{\pi}} \left(\frac{m}{2k_B T} \right)^{3/2} v^2 \exp\left(\frac{-mv^2}{2k_B T} \right), \tag{2.3}$$

where m is the mass of a single particle and v is the magnitude of the velocity. The probability of a particle exiting the reservoir through the opening will be proportional to its velocity. Thus, the beam will acquire an extra dependence on velocity yielding a beam intensity [29]

$$I(v) = I_0 \left(\frac{m^2}{2k_B^2 T^2} \right) v^3 \exp\left(\frac{-mv^2}{2k_B T} \right), \tag{2.4}$$

where I_0 is the full beam intensity. Furthermore, since the last collision that the gas undergoes is far from the reservoir, the beam is not significantly affected by the geometry of the opening.

Increases in pressure will lead to a reduction of the mean free path. Once $d > \overline{\Lambda}$ the reservoir opening will begin to influence the dynamics of expansion. This is known as the continuum regime and the gas begins to act like a compressible fluid. Operating in this regime offers many advantages over the effusive regime: beams are brighter as a result of higher reservoir pressures, gas temperatures are much cooler, and the gas is more focused and directional. The following sections will further substantiate this claim by summarizing discussions presented in [28, 30].

2.1 Thermodynamics

The desirable properties of the supersonic regime can be seen by examining flow of an ideal gas through an opening such that $d > \overline{\Lambda}$. We start with the ideal gas law

$$P = \rho\, k_B T\,. \tag{2.5}$$

We can express the first law of thermodynamics in terms of the internal energy e and heat q per unit mass:

$$dq = du + P\, d(\rho^{-1})\,, \tag{2.6}$$

where ρ^{-1} is specific volume corresponding to the volume of unit mass. The enthalpy per unit mass h is the sum of the internal energy and mechanical energy per unit mass,

$$h = u + \frac{P}{\rho}\,. \tag{2.7}$$

In the case of isentropic flow, there is no heat exchange between the gas and its surroundings during expansion ($dq = 0$). Then Equation 2.6 and Equation 2.7 become

$$0 = du + Pd(\rho^{-1}) \tag{2.8}$$

and

$$0 = dh + \frac{1}{\rho} dP\,. \tag{2.9}$$

The definitions of the specific heats at constant volume, c_V, and at constant pressure, c_P, are defined as

$$c_V \equiv \left(\frac{\partial e}{\partial T}\right)_V = \left(\frac{de}{dT}\right)_V \qquad \text{and} \qquad c_P \equiv \left(\frac{\partial h}{\partial T}\right)_P = \left(\frac{dh}{dT}\right)_P \tag{2.10}$$

where the replacement of the partial derivatives is valid for ideal gases. Using Equation 2.7, Equation 2.10, and the convenient ratio of specific heats $\kappa = c_P/c_V$ the following relation is obtained:

$$\kappa \frac{d\rho}{\rho} = \frac{dP}{P}\,. \tag{2.11}$$

Integration and appropriate use of the ideal gas law will yield the well-known relation

$$\frac{P_2}{P_1} = \left(\frac{T_2}{T_1}\right)^{\kappa/(\kappa-1)}\,, \tag{2.12}$$

which is a concise description of an adiabatic expansion where $P_2 < P_1$. This simplified treatment with ideal gases reveals that expansions into a vacuum will cool the gas.

2.2 Gas flow in one dimension

The claim that supersonic beams are more directional is ultimately a result of the transfer of random thermal energy into forward directional velocity. To arrive at this conclusion we consider the steady flow of a gas as a flow of a homogeneous, compressible medium where the velocity of the flow $\mathbf{w}$, the density ρ, and the pressure P are functions of space only. We will recast three conservation laws into a form more suitable for continuum mechanics:

Conservation of Mass:	$\nabla(\rho\,\mathbf{w}) = 0$	(2.13)
Conservation of Momentum:	$\rho\dfrac{D\mathbf{w}}{Dt} = -\nabla P$	(2.14)
Conservation of Energy:	$\dfrac{D}{Dt}\left(h + \dfrac{w^2}{2}\right) = 0\,.$	(2.15)

The operator seen in the last two equations is known as the material derivative and is defined as

$$\frac{D}{Dt} \equiv \frac{\partial}{\partial t} + (\mathbf{w}\nabla) \tag{2.16}$$

where the time derivative is separated into two components: a purely temporal change of a property and a change originating from the flow. We note that the second equation is vectoral and will lead to three partial differential equations for each momentum component. Furthermore, including the other two equations will result in a set of nonlinear equations in all three variables of space and time. To make further progress we will impose the assumption that the flow is one-dimensional and only depends on the distance through the flow. This simplification is valid while the rate of change of the cross-sectional area A is small in the direction of the flow. The conservation laws under this assumption yield the following equations:

$$\text{Conservation of Mass:} \qquad \frac{dw}{w} + \frac{d\rho}{\rho} + \frac{dA}{A} = 0 \tag{2.17}$$

$$\text{Conservation of Momentum:} \qquad w\,dw = -\frac{dP}{\rho} \tag{2.18}$$

$$\text{Conservation of Energy:} \qquad w\,dw + dh = 0\,. \tag{2.19}$$

2.3 Mach numbers and supersonic flow

Before using the one-dimensional conservation laws introduced above to describe some of the properties of supersonic flow there are additional concepts to address: the speed of sound c and the Mach number M_a. Information in the flow is

transmitted as a pressure disturbance whose speed for an ideal gas is

$$c = \sqrt{\frac{\kappa P}{\rho}}\,. \tag{2.20}$$

This equation assumes that there is no motion of the medium; however, motion of the frame can be included through a simple Galilean addition of velocities. Consequently, in the case of one-dimensional motion the disturbance would propagate with a velocity of $c \pm w$ where the sign depends on whether the wave travels with or against the flow. In the case where flow velocity exceeds the speed of sound ($w > c$), information can no longer propagate backwards through the flow and the flow is then termed supersonic. A convenient quantity is the ratio of the flow velocity to the local speed of sound

$$M_a = \frac{w}{c}\,, \tag{2.21}$$

which is a measure of the directed flow to that of the random thermal motion of the gas.

Combining the momentum conservation law with Equation 2.11 yields:

$$\frac{dA}{A} + \frac{dw}{w}\left(1 - M_a^2\right) = 0\,. \tag{2.22}$$

Many of the details of one-dimensional flow can be gleaned from this single equation. For flows such that $w < c$ ($M_a < 1$), the increases in the cross-sectional area A lead to decreases in the velocity, and vice versa. Once the flow exceeds the speed of sound ($M_a > 1$) the behavior flips: increases in the area lead to increases in flow velocity, and vice versa. To transition from sonic to supersonic M_a must cross unity and thus the channel will have a minimum cross-sectional area ($dA = 0$) known as the 'throat.'

Therefore, a supersonic flow can only emerge if a convergent-divergent nozzle, often called a Laval nozzle, is used.

Upon integrating the one-dimensional energy equation, we obtain the expression

$$\frac{w_2^2 - w_1^2}{2} = h_2 - h_1 \,, \tag{2.23}$$

illustrating how the enthalpy of the original gas is transferred to translational kinetic energy. Using the definition of the heat capacity at constant pressure, Equation 2.23 can be expressed as

$$w_2^2 - w_1^2 = 2c_P T_1 \left(1 - \frac{T_2}{T_1}\right) . \tag{2.24}$$

In the case of our supersonic nozzle, the point of origin of the gas is assumed to be within a reservoir where the flow velocity is negligibly small ($w_1 \approx 0$). Under this assumption, an expression for the final speed of the gas can be written as a function of either gas temperature or pressure of the reservoir with the help of Equation 2.12

$$w = \sqrt{2\frac{\kappa}{\kappa-1}\frac{RT_0}{M}\left[1 - \left(\frac{T}{T_0}\right)\right]} = \sqrt{2\frac{\kappa}{\kappa-1}\frac{RT_0}{M}\left[1 - \left(\frac{P}{P_0}\right)^{(\kappa-1)/\kappa}\right]}, \tag{2.25}$$

Since we will be releasing the gas into vacuum with a negligible pressure the maximum speed we can expect to obtain is

$$w_{\max} = v_{\mathrm{mp}}\sqrt{\frac{\kappa}{\kappa-1}} = \sqrt{2\frac{\kappa}{\kappa-1}\frac{k_B T_0}{m}} \,, \tag{2.26}$$

where v_{mp} is the most probable speed of the distribution in the gas phase. The modifying constant is greater than unity and shows that the supersonic expansion will have a higher maximum speed than gas held within the reservoir.

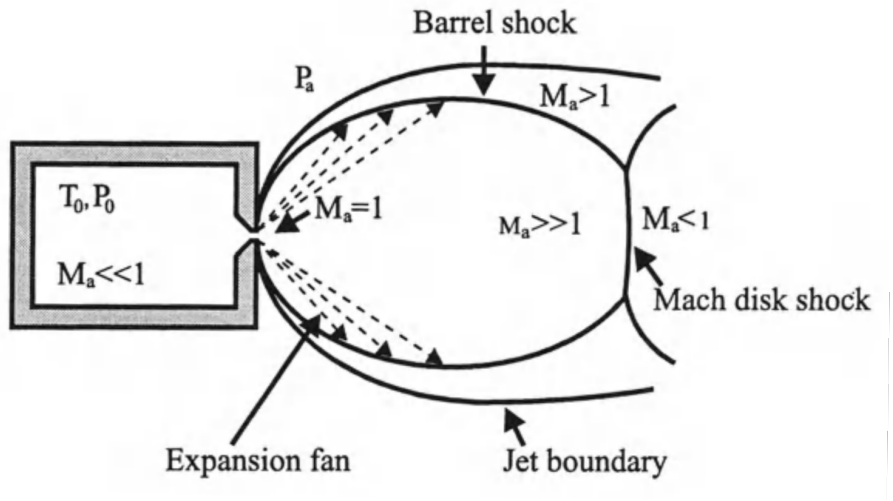

Figure 2.1: Expansion of a free jet of gas. Image reproduced from [28].

2.4 Supersonic beams as a cold, fast source of atoms

The preceding sections illustrate many of the features of adiabatic expansions in one dimension, primarily a supersonic beam will be both fast and cold. However, realistic beams expand in three dimensions and exhibit more complicated behavior. Despite this, much of the previous discussion is still valid and has been simulated and measured[31, 32, 33]. Many details seen in Figure 2.1 such as the angular extent of the supersonic flow, the barrel shock, and Mach disks can found in [28].

We can model the velocity distribution as an anisotropic Maxwellian distribution

$$f(\mathbf{v}) = \sqrt{\frac{m}{2\pi k_B T_\parallel}} \left(\frac{m}{2\pi k_B T_\perp}\right) \exp\left[-\frac{m}{2k_B}\left(\frac{(v_\parallel - w)^2}{T_\parallel} + \frac{v_\perp^2}{T_\perp}\right)\right], \tag{2.27}$$

where $T_\parallel$ and $T_\perp$ are the temperatures of the beam parallel and perpendicular to the axis of propagation, respectively. Likewise, the notation holds for the velocities $v_{\parallel,\perp}$.

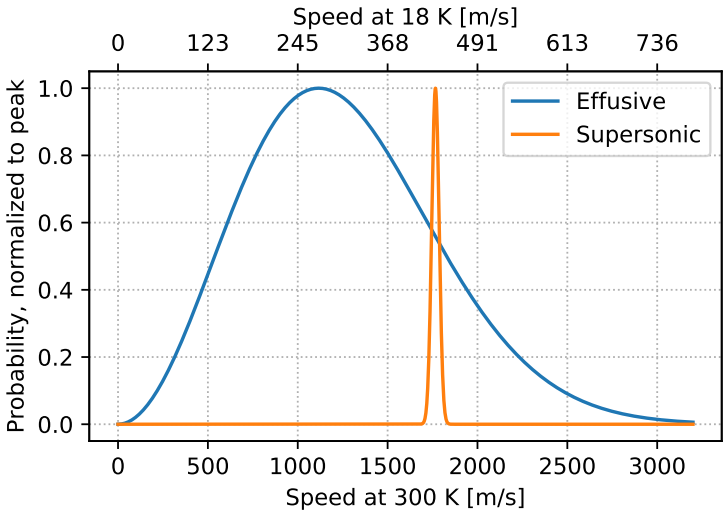

Figure 2.2: Velocity distributions of effusive and supersonic beams from a helium source held at 300 K and 18 K. Because both distributions have been normalized to their peak values, the difference in brightness of approximately three orders of magnitude is obscured [28].

In order to produce very cold transverse beams, the beam is passed through skimmers and apertures to extract the cold interior. Effectively, the transverse temperature manifests as a loss of atoms, so it is appropriate to focus on only the parallel component of the anisotropic Maxwellian distribution

$$f_{\parallel}(v_{\parallel}) = \sqrt{\frac{m}{2\pi k_B T_{\parallel}}} \exp\left[-\frac{m(v_{\parallel}-w)^2}{2k_B T_{\parallel}}\right] . \tag{2.28}$$

This velocity distribution is compared with a standard Maxwellian velocity distribution in Figure 2.2 for helium with the same reservoir temperatures. Immediately apparent is the stark difference in the widths of the two distributions with the supersonic beam being much narrower. At room temperature helium will be a few Kelvin; however, cryogenically cooling the reservoir to ∼20 K produces beams with temper-

atures as low as 200 mK. Furthermore, the distribution is shifted up in velocity by a factor $\sqrt{\kappa/(\kappa-1)} \approx 1.6$ in the case of helium.

2.5 Time-of-flight analysis

For an isolated supersonic beam, it is possible to predict its expansion solely from the properties of the source reservoir. We will, however, be using the beam as a vehicle for entrainment of other atomic species (entraining lithium into a helium beam). It is useful to have an additional independent method available to measure the beam expansion and quantify its temperature without explicit knowledge of the properties of the source reservoir. Following the work of [34, 35, 36], we adopt a model describing the evolution of a beam. Assuming once again that expansion is Maxwellian in velocity and Gaussian in space, we can express the probability distribution of locating an atom in the phase space volume $(\mathbf{x_0}, \mathbf{v_0})$ as [35, 36]

$$\mathcal{N}(x_0, y_0, z_0, v_{x0}, v_{y0}, v_{z0}) = \prod_{i \in \{x,y,z\}} g(i_0, \sigma_{i0})\, g(v_{i0}, \sigma_i v)\,, \tag{2.29}$$

where $g(x, \sigma) = (2\pi\sigma^2)^{-1/2} \exp(-x^2/(2\sigma^2))$ is the general function for a normalized Gaussian distribution with a variance of σ^2. In principle each dimension of the distribution can be initialized with its own spatial variance σ_{i0}^2 and thermal variance σ_{iv}^2. Likewise, the temperature of each axis is related to the thermal velocity of the distribution as

$$T_i = \frac{m}{k_B}\sigma_{iv}^2 \tag{2.30}$$

where $i \in \{x, y, z\}$. A time-of-flight model of the atomic cloud can be created by relating the velocity components to the cloud's position and time

$$v_{x0} = \frac{x - x_0}{t - t_0}\,, \quad v_{y0} = \frac{y - y_0}{t - t_0}\,, \quad v_{z0} = \frac{z - z_0}{t - t_0} + w\,, \tag{2.31}$$

where $\mathbf{x_0}$ and t_0 are the initial positions and times of the beam, respectively. The z-component includes the initial propagation velocity w of the beam. Making the above transformation and integrating Equation 2.29 over all initial positions yields the probability distribution of finding an atom at position (x,y,z) after time t

$$\mathcal{N}(x, y, z, t) = g(x, \sigma_t)\, g(y, \sigma_t)\, g(z + w, \sigma_t), \tag{2.32}$$

where, importantly, $\sigma_t = \sqrt{\sigma_{i0}^2 + \sigma_{iv}^2 t^2}$ for $i \in \{x, y, z\}$. We will directly measure σ_t at various points in our experiment in order to extract σ_{iv}. This will be subsequently used to calculate the heating that is caused by the magnetic gradient forces generated from our kick. From this expression it is readily apparent that the temperature T of a cloud can be measured from two positions:

$$\begin{aligned} T &= \frac{m}{k_B} \frac{\sigma_2^2 - \sigma_1^2}{t_2^2 - t_1^2} \\ &= \frac{m}{k_B} \frac{(\sigma_0^2 + \sigma_v^2 t_2^2) - (\sigma_0^2 + \sigma_v^2 t_1^2)}{t_2^2 - t_1^2} \\ &= \frac{m}{k_B} \sigma_v^2\,. \end{aligned} \tag{2.33}$$

Chapter 3

Atomic Physics with Lithium

Lithium, derived from the Greek word λιθος meaning 'stone', is the lightest metal and solid in the periodic table. As a member of the alkali group, it is highly reactive to water and must be handled with care in atmosphere to prevent oxidation or spontaneous ignition in humid environments. Some of its physical properties are shown in Table 3.1. Many of the experiments related to this work start with an effusive beam of lithium requiring vaporization of the metal. The vapor pressure of lithium below the melting point as a function of temperature follows

$$\log(P) = 10.673 - \frac{8310}{T} \tag{3.1}$$

where the pressure P and the temperature T are measured in Pa and K, respectively. Beyond the melting point the vapor pressure is better described by

$$\log(P) = 10.061 - \frac{8023}{T} \tag{3.2}$$

Property	**Symbol**	**Value**	**Reference**
Density	ρ	$0.534\,\mathrm{g/cm^3}$	[37]
Melting Point	T_M	$453.69\,\mathrm{K}$	[37]
Boiling Point	T_B	$1615\,\mathrm{K}$	[37]

Table 3.1: Physical properties of lithium.

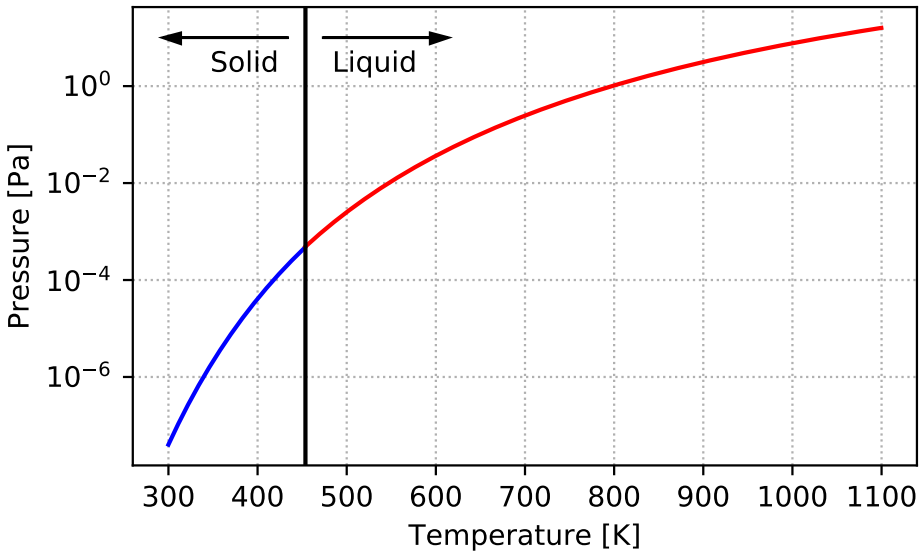

Figure 3.1: Vapor pressure of lithium as a function of temperature. The vertical black line delineates the melting point T_M of lithium at 453.69 K.

with only slight changes of the constants. Both fits are accurate to within five percent of measured data [37]. These fits are displayed in Figure 3.1 across a broad range of temperatures representative of typical operating conditions addressed throughout this dissertation.

3.1 Atomic structure of lithium-7

Elemental lithium has only two naturally occurring stable isotopes: ^{6}Li and ^{7}Li with abundances of 7.6% and 92.4%, respectively. This work addresses only the properties of the heavier variety ^{7}Li and henceforth will be assumed if not explicitly stated. Many of the fundamental properties of the element are summarized in Table 3.2.

Property	Symbol	Value	Reference
Atomic Number	Z	3	
Nucleons	$Z+N$	7	
Natural Abundance	η	92.4%	[37]
Atomic Mass	m	7.016003 u	[37]
Total Electronic Spin	S	1/2	
Total Nuclear Spin	I	3/2	[37]

Table 3.2: Atomic properties of ^{7}Li

Like all alkali metals in the first column of the periodic table, ^{7}Li has only a single valence electron that will be the main contributor of the atomic physics. In the ground state configuration, $1s^2 2s^1$, the electron will reside in the s orbital with zero angular momentum. Under an excitation the electron will be promoted upward into the $1s^2 2p^1$ configuration and acquire a unit of angular momentum. These two states are commonly referred to by their spectroscopic notation as ^{2}S and ^{2}P for the ground and excited states, respectively, and comprise all of the commonly known D-line transitions. The emergence of these two states are most simply seen from the central-field approximation [38] where the valence electron is taken to be independent during calculations of the energy of the atom. An image of the energy levels of lithium is shown in Figure 3.2.

Within the D-line are two distinct sub-groups, the D_1- and D_2-lines, that result from the intrinsic spin of the electron interacting with the orbital angular momentum. This interaction, aptly named the spin-orbit coupling, divides the D-lines into the two subgroups and is termed the fine structure. The interaction Hamiltonian can be written as

$$\hat{\mathbf{H}}_{\text{S-O}} = (g_s - 1)\frac{\hbar^2}{2m_e^2 c^2}\left(\frac{1}{r}\frac{\partial \phi(r)}{\partial r}\right)\hat{\mathbf{S}}\cdot\hat{\mathbf{L}} \tag{3.3}$$

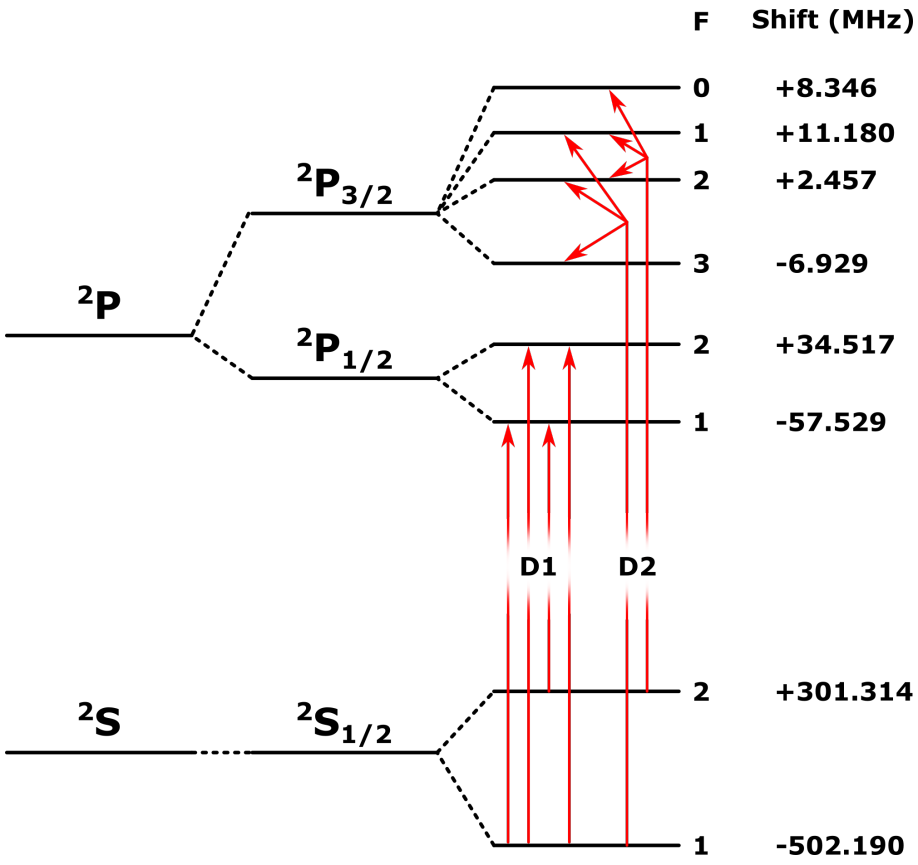

Figure 3.2: Energy level diagram of ^{7}Li ground and excited states. We optically pump on the ^{7}Li D1 transition to shift atoms from the F = 1 state into the F=2 state or vice versa. Frequency shifts are from [39].

where m_e is the mass of the electron, c is the speed of light, $\hbar$ is the reduced Planck's constant, r is the radial distance from the center of the atom, $\phi(r)$ is the potential produced by the nucleus and inner electrons, and $\hat{\mathbf{L}}$ and $\hat{\mathbf{S}}$ are the orbital and spin angular momentum operators, respectively. In the absence of strong electric or magnetic fields it is convenient to define the total angular momentum operator

$$\hat{\mathbf{J}} = \hat{\mathbf{L}} + \hat{\mathbf{S}}\,, \tag{3.4}$$

where the magnitude of J may only take values in integral steps in the range of

$$|L - S| \leq J \leq |L + S|\,. \tag{3.5}$$

This interaction leads to the splitting of the ^{2}P excited state into the $^2\mathrm{P}_{1/2}$ and $^2\mathrm{P}_{3/2}$ states which correspond to the D_1- and D_2-line respectively. We are using the Russell-Sanders notation to denote the states of S, L, and J as $^{2S+1}L_J$ where L historically is converted from $L = 0, 1, 2, \ldots$ to S, P, D, etc.[40, 38]. These two states are split by roughly 10.05 GHz [41].

Earlier it was alluded that there is further substructure within the D-lines. This *hyperfine* structure is a result of the nucleus being not necessarily spherically symmetric and thus has an associated nuclear spin. This interaction is much weaker than spin-orbit coupling resulting in a much smaller splitting of the states. The ^7Li ground state bifurcates into two groups of states separated by 803.5 MHz. The operator for this interaction can be written [40] as

$$\hat{\mathbf{H}}_{\mathrm{HF}} = -\hat{\boldsymbol{\mu}} \cdot \hat{\mathbf{B}}(0) + \frac{1}{6} e \sum_{\alpha,\beta} \hat{\mathbf{Q}}_{\alpha\beta} \frac{\partial^2 \phi(0)}{\partial x_\alpha \partial x_\beta}\,, \tag{3.6}$$

where $\hat{\mu}$ and $\hat{\mathbf{Q}}$ are the nuclear magnetic dipole moment and nuclear electric quadrupole moment operators respectively. The magnetic field operator $\hat{\mathbf{B}}$ and electric potential ϕ are evaluated at the location of the nucleus. The first term is entirely analogous to the spin-orbit interaction. The latter term will only contribute in the case of a non-spherically symmetric electric field present in the $^2P_{1/2}$ and $^2P_{3/2}$ states. However, for the $^2S_{1/2}$ with an orbital angular momentum $L = 0$ the term will be 0.

3.2 Zeeman splitting

The Zeeman splitting of the ^{7}Li ground state in the presence of a magnetic field is shown in Figure 3.3. The magnetic field interacts with the total electronic and nuclear magnetic moments of the $^2S_{1/2}$ state of the lithium atom and the interaction energy can be captured by the Hamiltonian

$$\hat{\mathbf{H}}_Z = -\left(\hat{\mu}_J + \hat{\mu}_I\right) \cdot \vec{B} \tag{3.7}$$

where $\hat{\mu_J}$ and $\hat{\mu_I}$ represent the total electronic and nuclear magnetic moments, respectively. The total magnetic moment $\hat{\mu}$ can be expressed in terms of the electronic $\hat{\mathbf{J}}$ and nuclear $\hat{\mathbf{I}}$ spins by

$$\hat{\mu} = \hat{\mu}_J + \hat{\mu}_I = \frac{\mu_B}{\hbar}\left(g_J\hat{\mathbf{J}} + g_I\hat{\mathbf{I}}\right) \tag{3.8}$$

where μ_B is the Bohr magneton, $\hbar$ is the reduced Plank's constant, and g_J and g_I represent the electronic and nuclear Landé-g factors.

To fully describe the Zeeman splitting we include hyperfine interactions whose Hamiltonian can be represented by the sum of the dipole and quadrupole contribu-

tions as

$$\hat{\mathbf{H}}_{\mathbf{hfs}} = hA_J\hat{\mathbf{I}}\cdot\hat{\mathbf{J}} + hB_J\frac{6(\hat{\mathbf{I}}\cdot\hat{\mathbf{J}})^2 + 3(\hat{\mathbf{I}}\cdot\hat{\mathbf{J}}) - 2I(I+1)J(J+1)}{2I(2I-1)2J(2J-1)}\,, \tag{3.9}$$

where A_J and B_J are the dipole and quadrupole constants respectively dependent on the given state [42, 43, 44]. For the case of $J = 1/2$, as with ground state ^{7}Li , the quadrupole constant is identically zero leaving hyperfine splitting dependent only on the dipole contribution. Generally, the electric quadrupole interaction is present for states $I, J \geq 1$. With this simplification the total Hamiltonian can be rewritten as

$$\hat{\mathbf{H}} = \hat{\mathbf{H}}_{hfs} + \hat{\mathbf{H}}_Z = hA_J\hat{\mathbf{I}}\cdot\hat{\mathbf{J}} - \frac{\mu_B}{\hbar}\left(g_J\hat{\mathbf{J}} + g_I\hat{\mathbf{I}}\right)\cdot\mathbf{B}\,. \tag{3.10}$$

For the case of the $^2\mathrm{S}_{1/2}$ ground state of ^{7}Li where $J = 1/2$ and $I = 3/2$, diagonalization of the Hamiltonian will yield the following expression

$$\frac{E(F_\pm, m_F)}{\Delta E_{hfs}} = -\frac{1}{2(2I+1)} - \left(\frac{m_F}{g_J/g_I - 1}\right)x \pm \frac{1}{2}\sqrt{1 + \left(\frac{4m_F}{2I+1}\right)x + x^2} \tag{3.11}$$

known as the Breit-Rabi formula [45] for the energies as a function of the dimensionless parameter

$$x = \frac{(g_J - g_I)\,\mu_B B}{\Delta E_{hfs}}\,. \tag{3.12}$$

The value for the hyperfine splitting ΔE_{hfs} can be found by diagonalizing Equation 3.9 and calculating the difference between the eigenvalues. In the case of the $^2\mathrm{S}_{1/2}$ state, diagonalizing produces

$$E_{hfs} = \frac{1}{2}A_J\left(F(F+1) - I(I+1) - J(J+1)\right) \tag{3.13}$$

and upon differencing

$$\Delta E_{hfs} = A_J F\,. \tag{3.14}$$

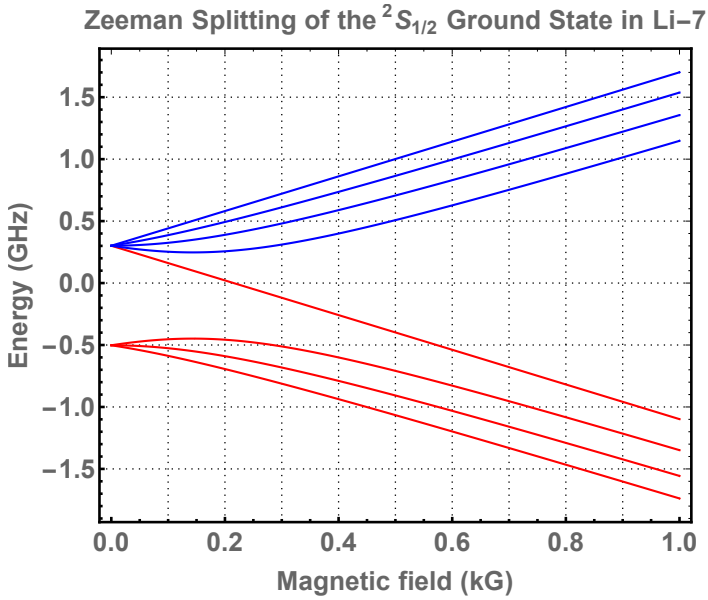

Figure 3.3: Breit-Rabi diagram for the ^{7}Li ground state. Red and blue lines denote high-field and low-field seeking states respectively. The upper and lower clusters of lines correspond to the F=2 and F=1 states respectively. Beyond 144 G all F = 1 states are entirely high-field-seeking.

Plotting this formula in Figure 3.3 shows that four m_F states within the F=2 manifold of the ^{7}Li $^2S_{1/2}$ state monotonically increase in energy with increasing magnetic field strength. We term these atoms as 'low-field-seeking' (LFS) as they will travel against the gradient of magnetic fields to minimize their energy. Conversely, atoms in the F=1 manifold of the $^2S_{1/2}$ state find high fields to be energetically favorable and are hence termed 'high-field-seeking' (HFS). It is important to acknowledge in the case of ^{7}Li one m_F state in the F=2 manifold ($m_F = 0$) is always high-field-seeking and must be avoided when applying forces with magnetic field gradients. Atoms in the F=2 manifold have the natural tendency to react to forces in opposite directions. This makes them poorly suited for magnetic manipulation in states of mixed m_F.

From Figure 3.3 we see that at sufficiently large magnetic fields the nuclear spin decouples from $\hat{\mathbf{J}}$ and the Hamiltonian can be more simply expressed as

$$\hat{\mathbf{H}} = \hat{\mathbf{H}}_Z = -\frac{\mu_B}{\hbar}(g_J\hat{\mathbf{J}} + g_I\hat{\mathbf{I}}_z)\cdot\mathbf{B} \tag{3.15}$$

$$= -\frac{\mu_B}{\hbar}(g_J\hat{J}_z + g_I\hat{I}_z)B \tag{3.16}$$

where the Landé g-factor g_J is given by

$$\begin{aligned} g_j &= g_L\frac{J(J+1)-S(S+1)+L(L+1)}{2J(J+1)} + g_S\frac{J(J+1)+S(S+1)-L(L+1)}{2J(J+1)} \\ &= 1 + \frac{J(J+1)+S(S+1)-L(L+1)}{J(J+1)}\,. \end{aligned} \tag{3.17}$$

In the last step values $g_L \approx 1$ and $g_S \approx 2$ have been used. The nuclear contribution of the Landé g-factor g_I in g_J is sufficiently small at the level of 0.1% and can be safely neglected. Using Equation 3.16 to find the energy, we obtain

$$\Delta E = \langle H_z\rangle = \mu_B g_J m_J B\,, \tag{3.18}$$

which will be sufficient for the field strengths accessible in our experiment.

3.3 Optical transitions

In order to prepare the quantum state of lithium in our experiment we use lasers tuned to specific frequencies to drive optical transitions on the D1 line. We provide a brief overview showing how these states are connected through electric dipole interactions with near resonant light that follows the discussions presented in [13, 44, 46].

The strength of a transition from the state $|(JI), F, m_F\rangle$ to the excited state $|(J'I'), F', m'_F\rangle$ is proportional to the square of the electric dipole matrix element and is given by

$$|\langle (J'I'), F', m'_F| \hat{\mathbf{d}} |(JI), F, m_F\rangle|^2 . \tag{3.19}$$

Evaluating this integral is relatively complicated, however, usage of the Wigner-Eckart theorem can greatly aid in simplifying the calculations. Recasting the electric dipole operator into an irreducible rank-1 spherical tensor, the previous expression can be written now as

$$D^2 = |\langle (J'I'), F', m'_F| d^1_q |(JI), F, m_F\rangle|^2 , \tag{3.20}$$

where q is dictated by the selection rules defined by the polarization of light ($q = 0$ and ± 1 correspond to linear and circular polarizations, respectively). Through

repeated application of the Wigner-Eckart theorem we obtain

$$\begin{aligned} D^2 = \quad & |\langle (J'I'), F', m'_F || \, d \, || (JI), F, m_F \rangle|^2 \\ & \times (2J+1)(2J'+1)(2F+1)(2F'+1) \\ & \times \begin{Bmatrix} L' & J' & S \\ J & L & 1 \end{Bmatrix}^2 \begin{Bmatrix} J' & F' & I \\ F & J & 1 \end{Bmatrix}^2 \begin{pmatrix} F & 1 & F' \\ M_F & q & -M'_F \end{pmatrix}^2 \end{aligned} \tag{3.21}$$

where the terms in the curly braces and parentheses are the 6-j and 3-j symbols respectively and the first term is the reduced matrix element that is determined by radial contributions of the atoms' wavefunctions. If we just consider the D1 transition from the ground state $|2^2S_{1/2}, F, m_F\rangle$ and excited state $|2^2P_{1/2}, F', m'_F\rangle$ of lithium, we can simplify Equation 3.21 to

$$\begin{aligned} D^2 = \quad & \langle 2^2P_{1/2}, F', m'_F || d || 2^2S_{1/2}, F, m_F \rangle \\ & \times 4(2F+1)(2F'+1) \\ & \times \frac{1}{6} \begin{Bmatrix} 1/2 & F' & 3/2 \\ F & 1/2 & 1 \end{Bmatrix}^2 \begin{pmatrix} F & 1 & F' \\ M_F & q & -M'_F \end{pmatrix}^2 . \end{aligned} \tag{3.22}$$

A summary of the relative strengths for the ^{7}Li D1 transition is shown in Figure 3.4 originating from the F=1 and F=2 manifolds of the $^2S_{1/2}$ state. Through polarization of the laser we can *optically pump* the atoms into different m_F sublevels. Rather than pumping the atoms into a single m_F state for our experiment, we are only concerned with avoiding the $m_F = -2$ state of the $^2S_{1/2}$ F=2 ground state. As mentioned in section 3.2, only the $m_F = -2$ state is high-field-seeking unlike the rest of the F=2 manifold that is low-field-seeking. For this reason, we only kick and measure atoms in the F=1 manifold. The stages of state preparation that are described later in section 5.3 are simply navigating around this quirk of lithium.

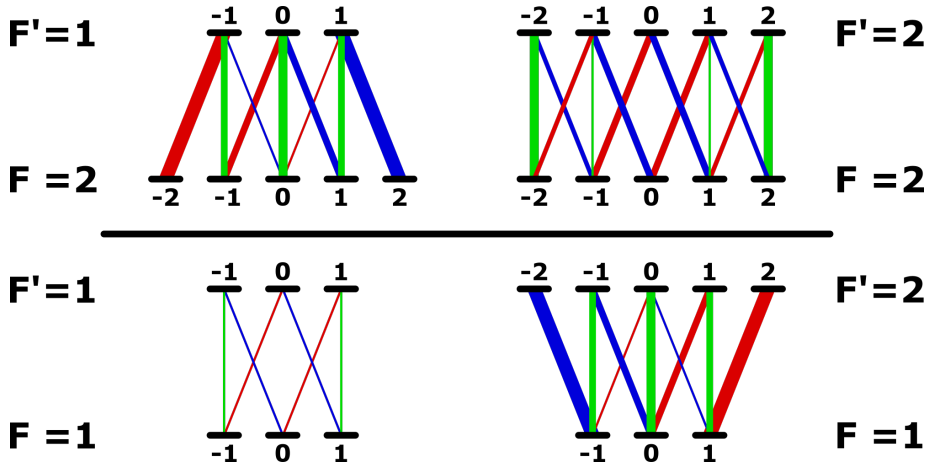

Figure 3.4: Summary of the transition strengths for ^{7}Li D1 line from both F=1 and F=2 states. The green lines indicate linear polarization and the red and blue lines represent σ_+ and σ_- circular polarizations respectively. Linewidths represent the relative strength of the transitions.

Returning to Equation 3.21 we can express the spontaneous emission rate [47] for a particular transition $(F', m') \to (F, m)$ as

$$A(F', m' \to F, m) = \frac{4\overline{\omega}^2}{3\pi\epsilon_0\hbar c^3} |\langle (J'I'), F', m'_F | \, d^1_q \, | (JI), F, m_F \rangle|^2 \, . \tag{3.23}$$

where $\overline{\omega}$ is the average transition frequency due to the smallness of the hyperfine splitting and c is the speed of light. By summing over all the transitions of a given line we will obtain the Einstein A coefficient for the line,

$$A_{D1} = \sum_{F,m} A(F', m' \to F, m) \, , \tag{3.24}$$

which is inversely related to the natural lifetime τ of the transition. Lithium has a relatively small lifetime of 27.102 ns which implies that it also has a large linewidth of 5.872 MHz. Finally, some related optical properties of ^{7}Li are summarized in Table 3.3.

D-line	Property	Symbol	Value	Reference
D_1,D_2	Lifetime	τ	27.102 ns	[48]
	Natural Linewidth	Γ	5.8724 MHz	[48]
D_1	Wavelength (vacuum)	λ	670.976 655 nm	[39]
	Frequency	ν	446.800 132 THz	[39]
D_2	Wavelength (vacuum)	λ	670.961 560 nm	[39]
	Frequency	ν	446.810 184 THz	[39]

Table 3.3: Optical properties of the ^{7}Li D-line transitions.

Chapter 4

Kicking with Electromagnetic Coils

4.1 Electromagnets

At this point we have formulated the approach to make a one-dimensional kick in Chapter 1 and will now discuss the tools used to generate our pulsed magnetic biases and kicks. The pulsed electromagnetic coil, our main tool, is used to generate the large magnetic fields necessary to kick and deflect the lithium atoms. Starting from the differential form of Ampère's law,

$$\nabla \times \mathbf{B} = \mu_0 \mathbf{J}\,, \tag{4.1}$$

where $\mathbf{J}$ is the current density and μ_0 is the permeability of free space, we recast the equation into its integral form, known as the Biot-Savart law [49],

$$\mathbf{B} = \frac{\mu_0}{4\pi} \int \mathbf{J}(\mathbf{x}') \times \frac{(\mathbf{x} - \mathbf{x}')}{|\mathbf{x} - \mathbf{x}'|^3} d^3x' \tag{4.2}$$

where the current density $\mathbf{J}(\mathbf{x}')$ is present at position $\mathbf{x}'$. For coils of wire it is more useful to rewrite the equation as

$$\mathbf{B} = \frac{\mu_0 I}{4\pi} \int_C \frac{\mathbf{dl} \times (\mathbf{x} - \mathbf{l})}{|\mathbf{x} - \mathbf{l}|^3} \tag{4.3}$$

where the current density $\mathbf{J}(\mathbf{x}')$ in the wire has been reduced to a constant current I pointing in direction $\mathbf{dl}$ and $(\mathbf{x} - \mathbf{l})$ is the displacement vector pointing from the

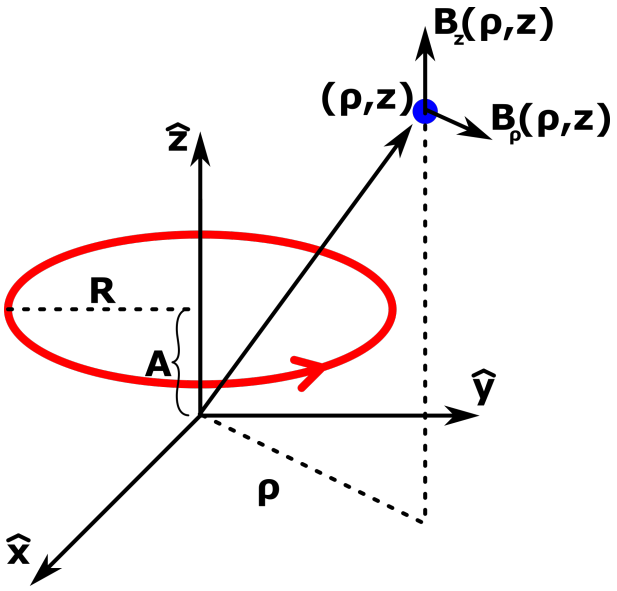

Figure 4.1: Illustration of the geometry of a current loop in cylindrical coordinates.

infinitesimal length element of the current path to the measurement point. From this equation, the magnetic field from an arbitrary current path can be calculated. The magnetic field created from a single coil loop of radius R at position $z_{coil} = A$ is given by the following formulas in cylindrical coordinates [50]:

$$B_z = \frac{\mu_0 I}{2\pi} \frac{1}{[(R+\rho)^2 + (z-A)^2]^{1/2}} \left[K(k^2) + \frac{R^2 - \rho^2 - (z-A)^2}{(R-\rho)^2 + (z-A)^2} E(k^2) \right],$$

$$B_\rho = \frac{\mu_0 I}{2\pi\rho} \frac{z-A}{[(R+\rho)^2 + (z-A)^2]^{1/2}} \left[-K(k^2) + \frac{R^2 + \rho^2 + (z-A)^2}{(R-\rho)^2 + (z-A)^2} E(k^2) \right],$$

where

$$k^2 = \frac{4\,R\,\rho}{(R+\rho)^2 + (z-A)^2}$$

and $K(k^2)$ and $E(k^2)$ are the complete elliptic integrals of first and second kind correspondingly. Figure 4.1 illustrates the arrangement described by these equations.

g_0	1
g_1	$3\,A$
g_2	$3\,(4\,A^2 - R^2)/2$
g_3	$5\,A(4\,A^2 - 3\,R^2)/2$
g_4	$15\,(R^4 - 12\,A^2R^2 + 8A^4)/8$

Table 4.1: First few expansion coefficients $g_n(A, R)$. Further expressions can be found in [50].

For the case of a point along the axis of the coil ($\rho = 0$) the z-component can be simplified to

$$B_z(\rho = 0) = \frac{\mu_0 I R^2}{2\,[R^2 + (A - z)^2]^{3/2}}\,. \tag{4.4}$$

Near the center of the coil we can express the magnetic field along the z-axis as a Taylor expansion in powers of z [50] as

$$B_z = \frac{\mu_0 I R^2}{2\,[R^2 + A^2]^{3/2}} \sum_n g_n(A, R) \left(\frac{z}{R^2 + A^2}\right)^n\,, \tag{4.5}$$

where the first few homogeneous polynomials $g_n(A, R)$ are listed in Table 4.1.

4.2 A simple implementation of bias and kicking coils

Unlike the Stern-Gerlach experiment, where both terms of

$$\mathbf{B}_t = \mathbf{B} + B_0\,\hat{\mathbf{k}} \tag{4.6}$$

are fixed by the physical dimensions and magnetizations of the permanent magnets, we have direct control over the first term using anti-Helmholtz coil configuration and the second term using a Helmholtz coil configuration. In an anti-Helmholtz coil pair currents circulate in opposite directions, whereas, in a Helmholtz configuration currents flow in the same direction.

4.2.1 Helmholtz coils

As a first step let us consider the simplest case of two coils of the same radius R located at distance $2A$ from each other. If the current in the two coils flow in the same direction then only the even terms of Equation 4.5 will be present in the magnetic field expansion:

$$B_z^{HH}(z) = \frac{\mu_0 I R^2}{[R^2+A^2]^{3/2}}\left[1 + 3(4A^2-R^2)\frac{z^2}{(A^2+R^2)^2} + 15(R^4-12A^2R^2+8A^4)\frac{z^4}{(A^2+R^2)^4} + O(z^6)\right] \quad (4.7)$$

$$= \frac{8\mu_0 I}{5\sqrt{5}R}\left[1 - \frac{144}{125}\frac{z^4}{R^4}\right] + O(z^6) \quad \text{for A=R/2}\,. \quad (4.8)$$

An ideal Helmholtz coil is one such that the field near the center of the coils is most homogeneous. Our goal then is to eliminate z^2 dependence by an appropriate choice of coil separation which is found to be $A_H = R/2$ through simple algebra. A plot of the total magnetic field along the z-axis for this configuration is shown in Figure 4.2 with the two underlying single-coil fields from which it is composed.

4.2.2 Anti-Helmholtz coils

The currents in an anti-Helmholtz pair will flow in opposing directions and will only have odd non-zero terms in its expansion:

$$B_z^{AH}(z) = \frac{\mu_0 I R^2}{[R^2+A^2]^{3/2}}\left[3A\frac{z}{R^2+A^2} + 5A(4A^2-3R^2)\frac{z^3}{(R^2+A^2)^3} + O(z^5)\right] \quad (4.9)$$

$$= \frac{48}{49}\sqrt{\frac{3}{7}}\frac{\mu_0 I}{R^2}z + O(z^5) \quad \text{for } A = \frac{\sqrt{3}R}{2}\,. \quad (4.10)$$

Depending on the application, there are two coil separations that can provide interesting gradient characteristics. First, by setting $A = R/2$ we can maximize the

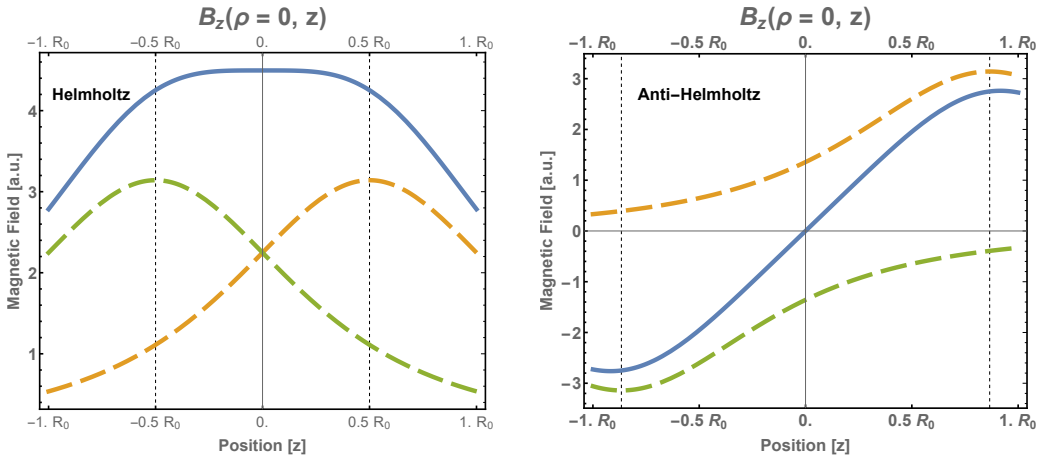

Figure 4.2: Magnetic field along the coil axis for a Helmholtz and anti-Helmholtz configuration respectively. Solid lines are the sum of the two single-coil fields (dashed) with radii R_0 at locations indicated by the dotted vertical lines. B_z has units of $\mu_0 I/(2\pi R_0)$.

gradient. This would allow us to achieve larger kicks but at the cost of gradient uniformity. Instead, we want to eliminate the z^3 term so that the field will be linearly proportional to z such that the gradient will be more uniform over space. As we are more interested in suppressing the heating of the beam, a small reduction in gradient strength is acceptable in order to improve kick uniformity. Setting the third order term to zero and solving yields $A_{AH} = \sqrt{3}R/2$. The resulting optimized magnetic field along the z-axis is again shown in Figure 4.2. Examining the slopes of the total fields in Figure 4.2 near the center of coils in a region of $0.25R_0$ to $0.35R_0$ show that the Helmholtz pair introduces a negligible gradient while the anti-Helmholtz pair provides a constant gradient.

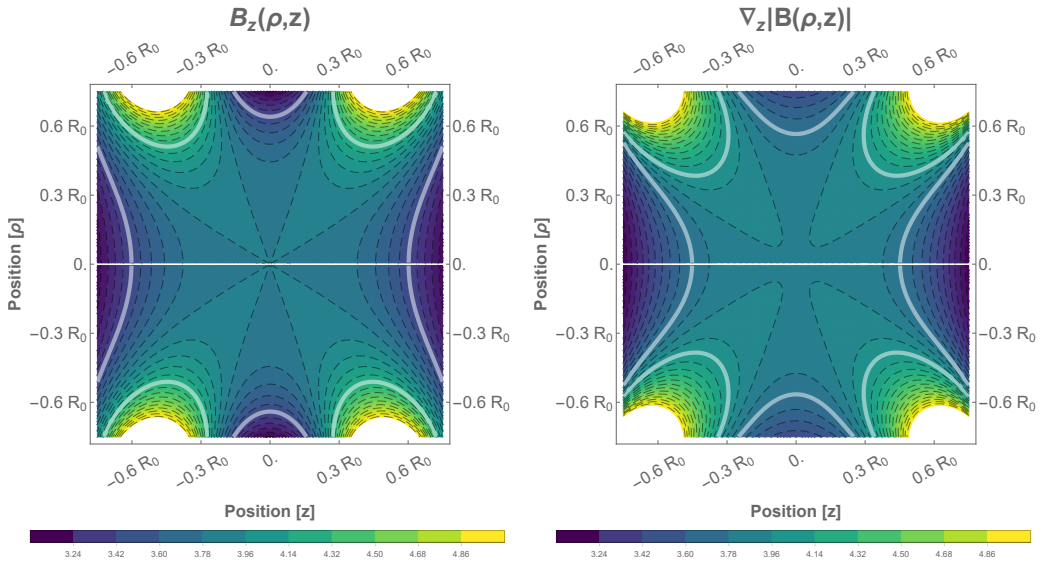

Figure 4.3: Magnetic field for a Helmholtz configuration (left) and the gradient of the magnetic field for an anti-Helmholtz configuration (right) in both ρ and z coordinates. Solid white lines indicate the threshold of a 10% variation. B_z scale has units of $\mu_0 I/(2\pi R_0)$ and $\nabla_z|B|$ scale has units of $\mu_0 I/(2\pi R_0^2)$.

4.2.3 Helmholtz variations in two dimensions

The preceding plots in Figure 4.2 focused solely on the axial z dependence of the fields and gradients; however, we can extend this discussion to include the radial ρ dependence. Shown in Figure 4.3 is the magnetic field and gradient of the Helmholtz and anti-Helmholtz configuration respectively as a function of both z and ρ. The solid white contours delineate the region where the variation of field and gradient is less than 10%. Atomic clouds in this region ($\sim 0.5R_0$) will experience a uniform force.

Before preceding, it is also useful to note that a single coil offset from the origin like those that compose the Helmholtz or anti-Helmholtz configurations can

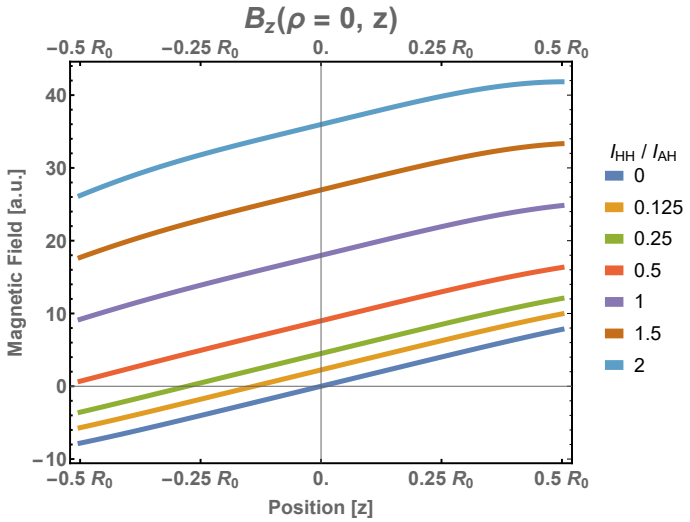

Figure 4.4: Creating a one-dimensional kick with a combination of Helmholtz and anti-Helmholtz coils. The current of the Helmholtz pair is held fixed. As the bias field is increased the zero-point crossing of the field is progressively pulled farther to the left. This causes the atoms to polarize and align in a single direction while maintaining a uniform gradient near the center of the coils. This is the regime of a one-dimensional kick.

also function as a bias or gradient. The key difference is that a single coil will couple these two effects together and will also result in a smaller region of uniformity. This will ultimately be the manner in which we create a bias in the actual coils due to experimental factors discussed later.

4.2.4 The combination of a bias and a gradient

Assuming that the placement of the two sets of coils are at the optimal distances as mentioned, it is useful to discuss the conceptual idea of the one-dimensional kick with these fields and gradients. Shown in Figure 4.4 is the field along the z-axis with the kicking current held at a fixed value. The bias currents are allowed to vary

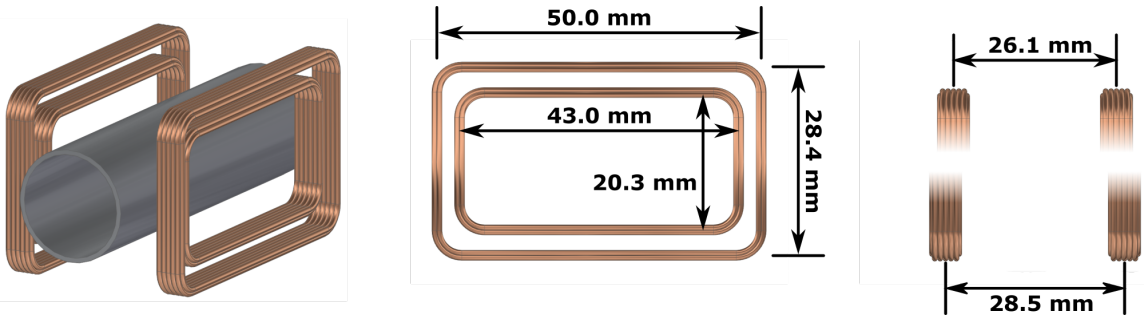

Figure 4.5: Dimensions of bias and kicking electromagnetic coils. The two outer larger coils are used for creating the magnetic bias. The inner coil pair function in a anti-Helmholtz configuration. All coils use 20 AWG Kapton-coated copper and are composed of 11 windings, 6 on the inside and 5 on the outside.

from being completely disabled ($I_{HH} = 0$) to twice that of the anti-Helmholtz currents ($2I_{AH}$). Increasing the bias strength effectively shifts the zero-point crossing progressively outside the center of the coils. This is important as atoms in a single atomic state will precess around the direction of the total magnetic field. In the absence of a bias atoms will experience a uniform force proportional to $\nabla|\mathbf{B}|$ (see Chapter 1). However, due to the sign inversion at $z = 0$ the atoms will be separated due to the magnetic moments aligning in opposing directions. By increasing the Helmholtz bias fields to be greater than that of the anti-Helmholtz fields, we enter the regime of one-dimensionality where the atoms are aligned or polarized in the same direction by the bias field while experiencing a uniform force.

4.3 Experiment coils

Coil dimensions shown in Figure 4.5 were chosen to satisfy the competing criteria of maximizing field uniformity along the propagation axis of the atomic beam

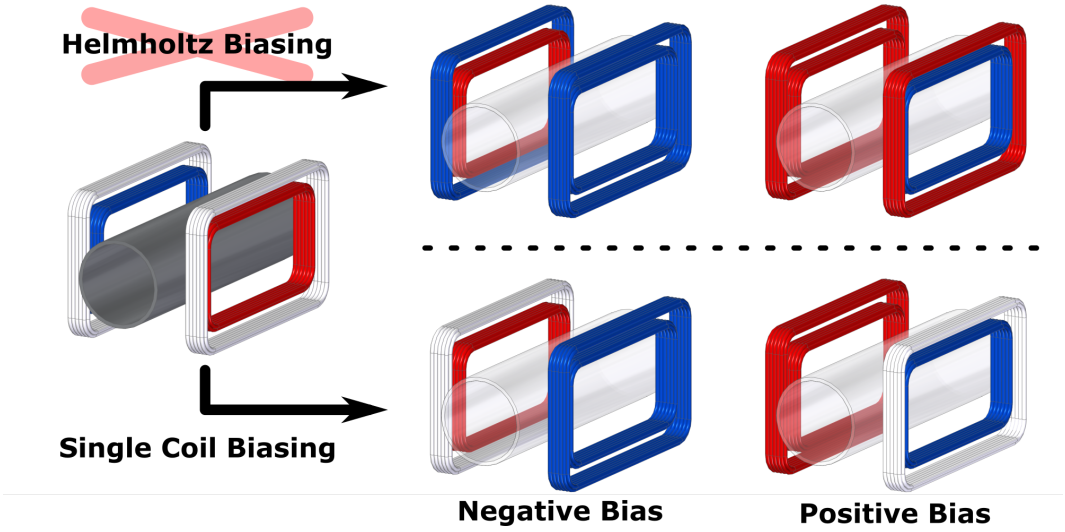

Figure 4.6: Bias field configuration for coils. Colors indicate the direction of current flow. Red and blue are clockwise and anti-clockwise respectively and white represents no current. The kick is generated by the anti-Helmholtz configuration shown on the left. Due to mutual inductances we avoid using a Helmholtz configuration.

while minimizing the inductance of the coils which lengthens the pulse duration. As a result the general coil geometry was elongated and deformed into a rectangular shape in order to better operate on a moving beam of atoms. The smaller, 43.0 mm $\times$ 20.3 mm, inner coils function as a pulsed anti-Helmholtz pair to create a strong magnetic field gradient. The larger, 50.0 mm $\times$ 28.4 mm, outer coils are pulsed individually to provide a magnetic bias of either sign. All four coils consist of two layers of Kapton coated 20 AWG wire with the inner and outer layers having 6 and 5 windings respectively. The inner anti-Helmholtz pair is separated by 26.1 mm and the outer is separated by 28.5 mm.

For any particular experiment three coils are pulsed. In theory the bias coils should be operated in a Helmholtz configuration in order to produce a large uniform

field near the coil centers. However, in practice, mutual inductances between adjacent inner and outer coils lead to strong coupling of the currents. This makes calibration of the current flow through each coil both involved and difficult. To illustrate this difficulty refer to Figure 4.6 where the four coils are drawn in a series of operational conditions. The colors denote the flow of current with white being zero current and red and blue indicating clockwise or anti-clockwise flow respectively. The inner anti-Helmholtz coils are operated in the same way across all of the current configurations shown.

The mutual inductance of two coils follows the form

$$M = k\sqrt{L_1 L_2} \tag{4.11}$$

where $L_{1,2}$ are the inductances of the individual coils and k is the coupling coefficient. The coupling coefficient can take any value in the range from 0 to 1 for magnetically isolated and tightly coupled coils respectively. For sake of analysis we will assume that our coils are ideal tightly coupled coils ($k = 1$). In the case of the Helmholtz configuration shown along the upper row of Figure 4.6, the inductance of the coils will have an increased and decreased value for currents aligned and anti-aligned respectively. At low to moderate biases the coupling of the coils (specifically the anti-aligned coils) cause the currents to deviate from expected isolated behavior and would require careful calibration. Rather than attempting to calibrate all of the currents for this complicated arrangement, we instead simplify the system to the single coil bias configuration. As previously mentioned, the single coil will introduce its own additional gradient; however, this effect was not a concern in our demonstration experiment.

4.3.1 Coil holders

Early proof-of-concept prototypes consisted of simple coils wound to specific dimensions that were liberally epoxied to a piece of nylon or Delrin. Initial tests revealed that the magnetic forces generated by the inner and outer coils ($\sim$1 T) were sufficient over prolonged operation to damage the unrestrained epoxy, separate the coils, and tear the insulating Kapton on the copper wires.

To combat such degradation, we designed the final coil holders, shown in Figure 4.7 to provide structure on all sides. The two coil holders and the retaining spacer are held together with nylon screws and clamped around the 0.75 in stainless steel vacuum chamber. Plastic is chosen for all structural parts to avoid eddy currents that limit magnetic fields at the center of the coils. The inner holder and retaining spacer are made of Delrin while the outer holder is printed out of PLA plastic[1].

Small holes seen in Figure 4.7 on the top of the retaining spacer and the flat surface of the inner coil holder are included in the design to facilitate the injection of epoxy[2] into the coil gaps. The epoxy is added to prevent any motion of the coils during a pulse. It is mixed and loaded into a syringe and then injected through a gauge 15 needle into the gaps colored in green shown in Figure 4.8. Due to the high viscosity of the epoxy a pneumatic piston is used to apply a constant force on the syringe. Holes are plugged with wooden applicator rods to prevent leakage of the epoxy during curing.

[1]The outer holder was 3D printed on a LulzBot TAZ 6 at The Foundary in the Fine Arts library due to lead times associated with the physics machine shop.

[2]We used an epoxy from Epoxies, Etc. (50-3150 FR). We chose this epoxy for its high thermal conductivity.

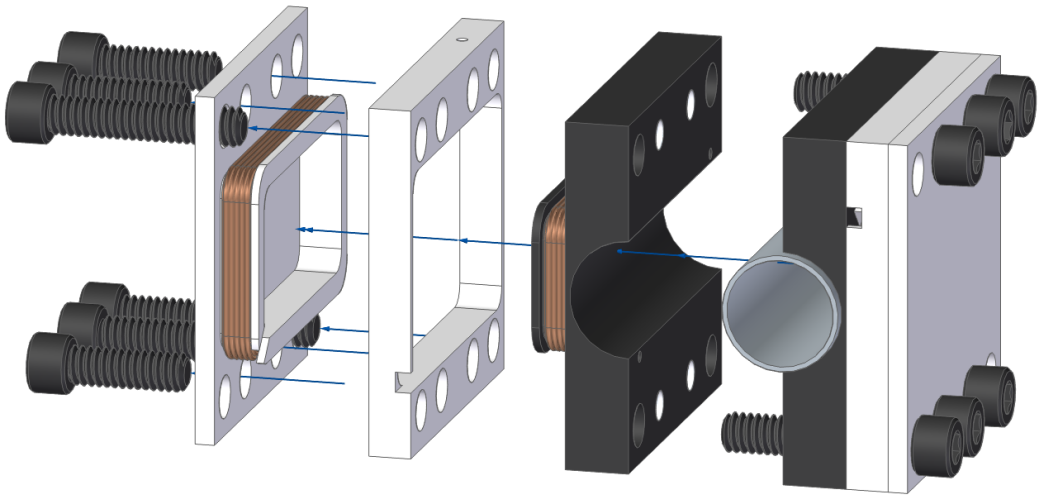

Figure 4.7: Exploded view of the coil holder. The holder is composed of two identical units of three major pieces. Coils are wound on separate mandrels and inserted into each other for precise alignment. In order to kick along both transverse orthogonal axes, the coil holder is capable of rotating around the vacuum chamber to realign the coils relative to the measurement system.

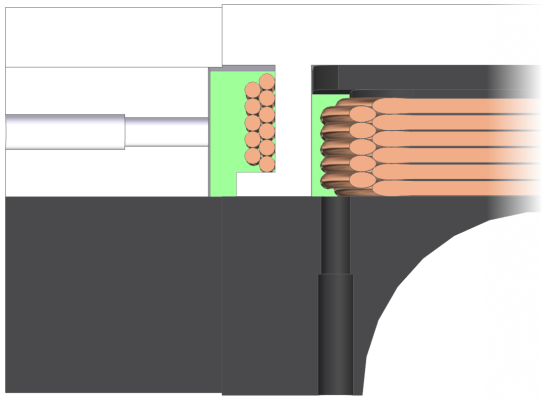

Figure 4.8: Coils are cemented inside the Delrin holder via epoxy injected through small holes shown via a section view.

4.4 Switching the coils

We operate our coils in a pulsed fashion to produce sizable magnetic fields and minimize the interaction time with the beam. Creating such current pulses that can be switched on and off within seconds is difficult in practice. The Maxwell-Faraday equation,

$$\nabla \times \mathbf{E} = -\frac{\partial \mathbf{B}}{\partial t}\,, \tag{4.12}$$

shows that a changing magnetic field will generate a corresponding electric field. Applying this to a coil of wire leads to Lenz's law,

$$\mathcal{E} = -N\frac{d\Phi}{dt}\,, \tag{4.13}$$

where $\mathcal{E}$ is the electromotive force, N is the number of windings in the coil, and Φ is the magnetic flux which passes through the coil. Switching a coil will produce a potential that induces a current that opposes changes in the magnetic field. This effect is not limited only to the wires of circuits, but also surrounding materials where eddy currents form in bulk materials such as metal heat sinks that might be near the coils.

4.4.1 Underdamped oscillator

Abrupt changes in current cause large unwanted voltage spikes that are very taxing to circuitry and coils. As a result, we avoid using circuits that directly dump currents to ground through a switch. Instead we exploit the properties of an RLC oscillator circuit to create more graceful switching characteristics in combination with a thyristor (see subsection 4.4.2). Ignoring the thyristor for now, we derive the

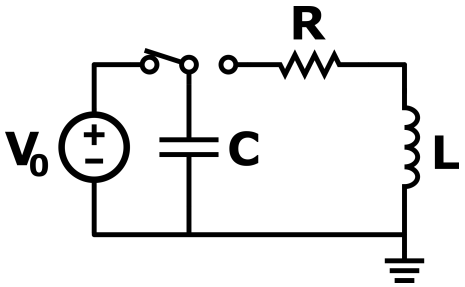

Figure 4.9: RLC circuit.

expected current in the RLC circuit. Using Kirchhoff's voltage law on the series circuit shown in Figure 4.9 we obtain

$$\frac{d^2}{dt^2}I(t) + 2\alpha\frac{d}{dt}I(t) + \omega_0^2 I(t) = 0 \tag{4.14}$$

where the attenuation is defined as $\alpha = R/2L$ and the resonant frequency $\omega_0 = 1/\sqrt{LC}$. The damping parameter

$$\zeta = \frac{\alpha}{\omega_0} = \frac{R}{2}\sqrt{\frac{C}{L}}\,, \tag{4.15}$$

is useful in separating the equation into the different regimes of operation. For $\zeta < 1$ the circuit behaves as an underdamped oscillator which exhibits a current that oscillates under a decreasing exponential envelope given by

$$I(t) = B_1 e^{\alpha t}\cos(\omega_d t) + B_2 e^{\alpha t}\cos(\omega_d t) \tag{4.16}$$

where $\omega_d = \sqrt{\omega_0^2 - \alpha^2} = \omega_0\sqrt{1-\zeta^2}$ is the modified oscillation frequency and $B_{1,2}$ are constants determined by the initial conditions of the circuit. Setting the inductor voltage and loop current to V_0 and $I = 0$ respectively at t=0 we can express the current flow as

$$I(t) = \frac{V_0}{L\,\omega_d}e^{-\alpha t}\sin(\omega_d t) \tag{4.17}$$

Coil	Inductance [μH]	Resistance [mΩ]
Small Coil #1	7.7	56.3
Small Coil #2	7.6	56.8
Large Coil #1	10.2	63.7
Large Coil #2	10.2	67.8

Table 4.2: Electrical parameters of the coils.

For $\zeta \ll 1$ the circuit behaves almost like that of an undamped oscillator.

4.4.2 Coil pulse circuitry

As described above, the large inductive spikes associated with switching large current sources represent a serious design consideration. The values for inductances and resistances of our coils are summarized in Table 4.2. Overall our circuit implements an underdamped RLC oscillator whose current is gently clamped after one half-cycle. A schematic of the circuit is shown in Figure 4.11 and is separated into two main sections - charging and discharging. At the top a 1 kV variable power supply[3] provides the current used to charge a 100 μF capacitor bank. Charging is initiated by closing the integrated gate bipolar transistor[4] (IGBT) and connecting it to the capacitor bank. The parallel flyback diode[5] protects the IGBT by preventing any voltage spikes generated from switching events from inducing reverse currents within the IGBT. Charging occurs on the order of 10 ms.

Once charged the IGBT is opened to disconnect the top branch from the bottom to leave essentially an RLC circuit with an additional component known as

[3]Analog Modules, Inc. Isolated Capacitor Charging Power Supply model 5724
[4]IXYS (now Littlefuse) IXGK120N120A3
[5]IXYS (now Littlefuse) DSEP 30-12A

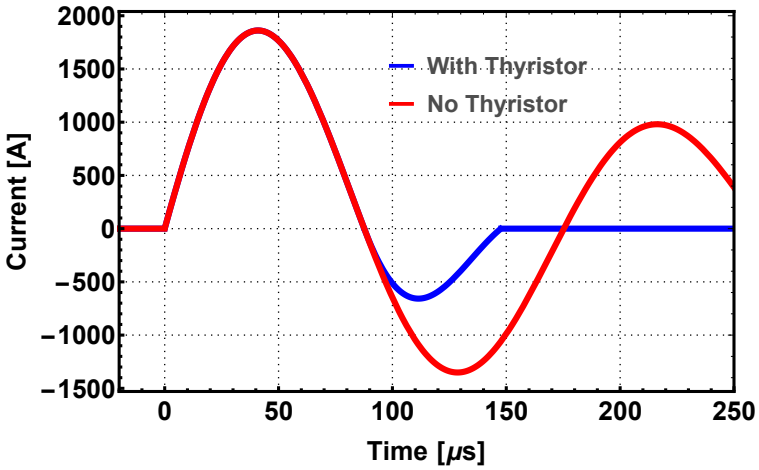

Figure 4.10: Plot of calculated currents representative of our coils and circuits. The red trace shows a normal under damped circuit with R, L, C values of 56.3 Ω, 7.7 µH, 100 µF, respectively. The blue curve represents the behavior expected from the thyristor clamping the reverse current.

a thyristor[6] in series. The thyristor is a bistable switch that conducts upon receiving a current trigger on its gate. Even after the trigger is removed, current will continue to flow until the device becomes reverse biased. In our circuit, charge stored in the capacitor bank is dumped to ground upon activation of the thyristor. The current passes through our coil and creates a magnetic field. After one half-cycle, the current is clamped to prevent multiple underdamped oscillations from 'ringing' in the coil. Furthermore, another flyback diode[7] is placed in parallel with the thyristor to absorb any reverse current.

On-board power for the IGBT and thyristor is supplied by two DC-DC con-

[6]IXYS (now Littlefuse) CLA80E1200HF
[7]IXYS (now Littlefuse) DSEP12-12B

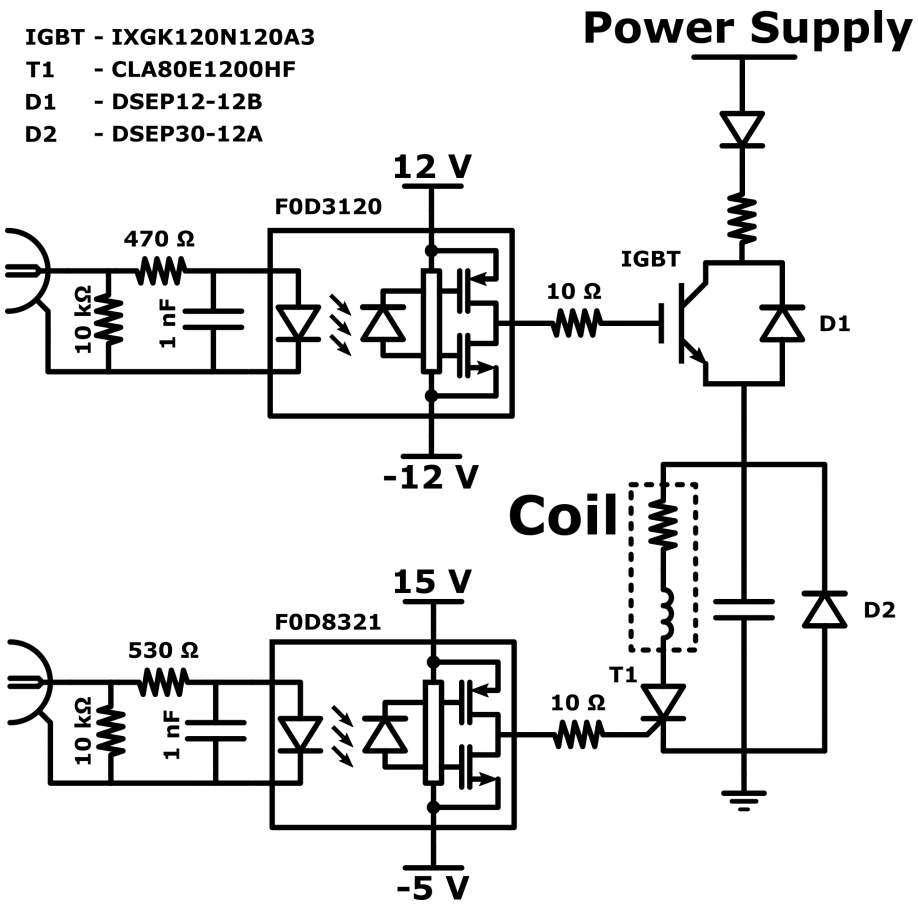

Figure 4.11: Schematic of the coil pulse circuitry. The circuit is divided into two main functions: charging and discharging. Charging is accomplished by connecting a 1 kV power supply to a capacitor bank. After charging, the IGBT is disconnected and a thyristor is activated that depletes the capacitor bank. The triggers for both the IGBT and thyristor are isolated from digital electronics via optocouplers.

verters[8] with 0.1 µF and 100 µF capacitors placed across both the inputs and outputs. The capacitors help provide a steady supply of current across a broad range of frequencies during large current draws. Both the IGBT and thyristor receive 5 V transistor - transistor logic (TTL) pulses from LabVIEW data acquisition (DAQ) hardware to control the precise timing of switching events. The circuit filters these pulses before passing the signal to an isolating optocoupler[9]. The optocoupler physically divides the low voltage digital circuitry from the high current switches through an optical transmission of the signal within the circuit element.

Each of the coils has a dedicated charging and discharging circuit with a corresponding capacitor bank, however, all four circuit boards share the 1 kV power supply. Charging is managed by selectively connecting each board temporarily via the charging IGBTs through automation software in LabVIEW. Furthermore, during each charging cycle the power supply can be configured to a different voltage to independently set the voltage on each capacitor bank. Configuring for non-equal voltages enables access to different gradient and bias fields generated by each coil.

All the circuits sans the high voltage power supply are packaged into a standard 19 in rack mount unit[10] (see Figure 4.12). Power for the low voltage circuitry (optocouplers) is supplied by a set of -5, 5, and 15 V switching power supplies[11] and distributed via bus bars to the four boards. One important detail necessary to

[8]Motien 1 W unregulated DC-DC converter model VL-1209SH6

[9]Both optocouplers in the circuit are made by On Semiconductor. The IGBT uses a F0D3120 optocoupler and the thyristor uses a F0D8321 optocoupler.

[10]Hammond Manufacturing provides many boxing options and replacement components for most of the product lines they sell. Useful for modifying existing equipment.

[11]TDK-Lambda LS series

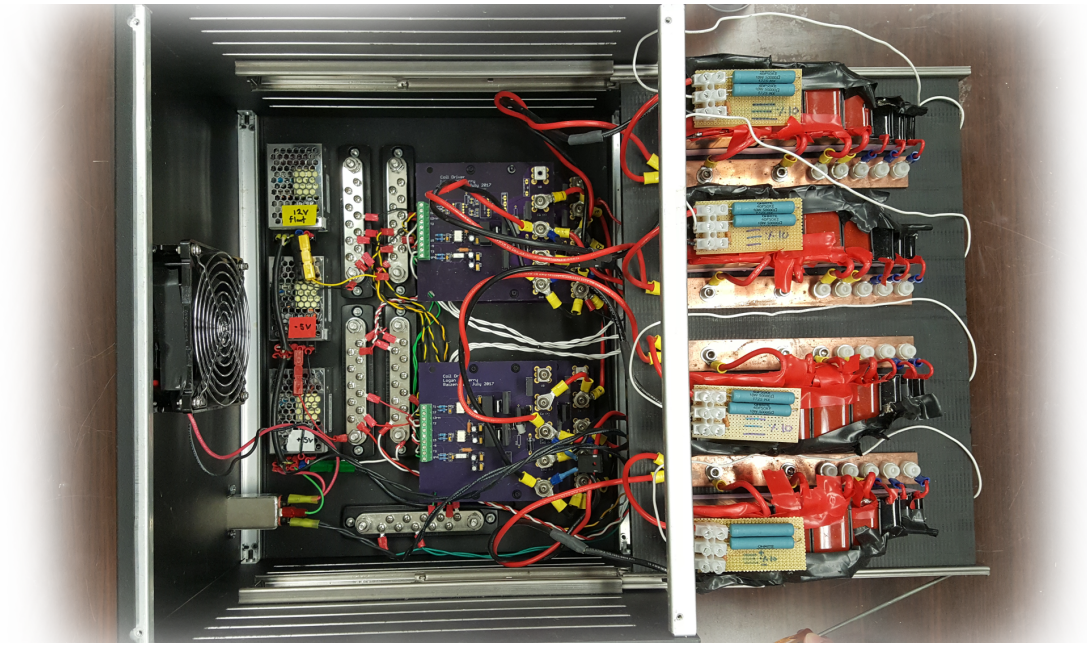

Figure 4.12: Interior of the coil pulse box. The capacitor bank slides out to reveal power supplies and the switching boards. The three switching power supplies are supplied by external wall voltage and distribute power to four switching boards (two boards are stacked below the other two).

prevent coil switching from interfering with the digital circuitry is to reference the power supplies connected to the thyristor optocoupler to the cathode of the thyristor. It is also important to ensure that the DC voltage reference is not connected to the AC wall ground. This would create a ground loop that would couple to other equipment connected to the wall. Dumping a large current to ground will effectively shift the reference point temporarily and cause interference in peripheral equipment in addition to spurious digital triggers.

4.5 Simulation of fields

Calibration of the currents for the coils are carried out with Hall-effect current transducers[12]. Each lead to a coil has its own transducer as seen in Figure 4.13. Since the transducers are only rated to 200 A, all capacitor voltages were scaled proportionally downward to operate within the maximum current range. Scaling these voltages up to typical operational conditions (600 V on kicking coils and a max of 800 V on bias coils) we can use these currents as inputs into a theoretical model that calculates the fields. Shown in Figure 4.14 is a plot of the gradient zero-point crossing as a function of the voltage allowing us to gauge the linearity of the bias behavior. Furthermore, the norm of the magnetic field along the symmetry planes is summarized in Figure 4.15. The fields exhibit the same qualitative behavior seen in section 4.2. In the absence of a bias the anti-Helmholtz field generates a field gradient that is directed outward from the center of the coils. Upon applying a strong bias field the gradient becomes directional and uniform once the zero-crossing of the total

[12]Tamura L31S200S05FS Current Sensor

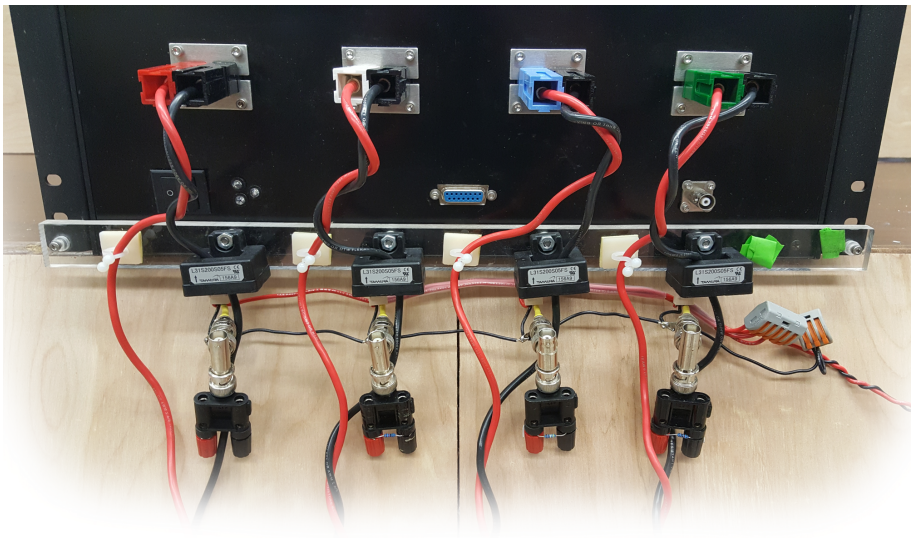

Figure 4.13: Current transducers surround the wires for each coil to monitor the current during pulses. All transducers are powered by a power supply not shown.

field has been shifted outside the center of the coils.

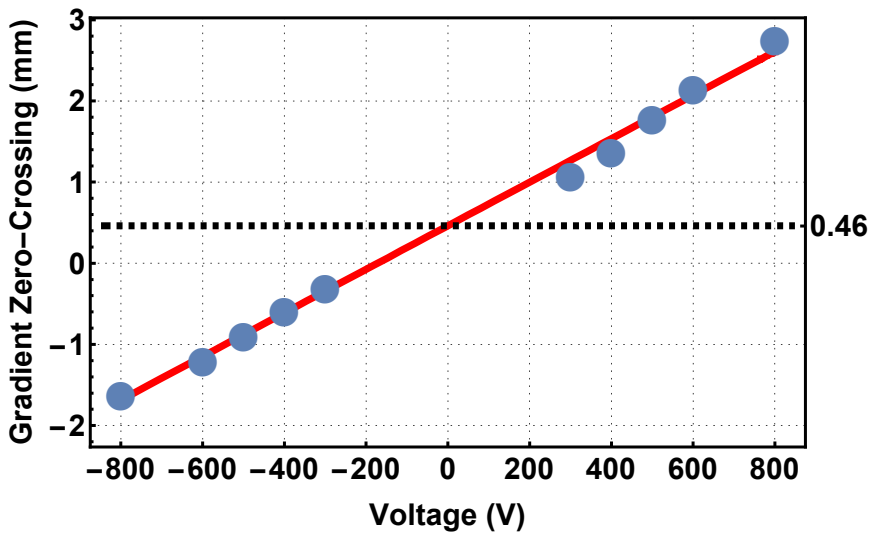

Figure 4.14: Total field zero-point crossing as a function of bias voltage. Behavior is roughly linear albeit with a slight offset towards positive biases.

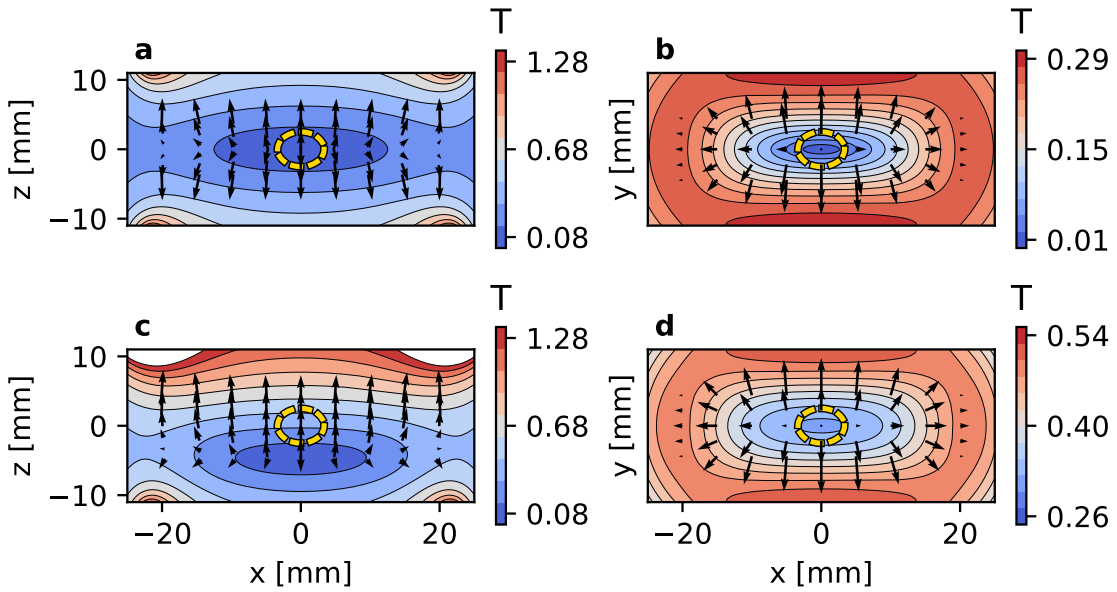

Figure 4.15: Simulation of the magnetic fields in the final coil design. Contour plots of the norm of the magnetic field are overlaid by a vector plot indicating the direction and strength of the magnetic force on high-field-seeking atoms. Axes are aligned such that the kick is along the z-axis and the atomic beam propagates along the x-axis. The dotted yellow region represents the extent of the lithium cloud at the peak of the magnetic kick. (a, b) Only the anti-Helmholtz coils are active at 1500 A producing a symmetric field and force profile about the axis of propagation. (c, d) An additional 1800 A bias coil has been included which shifts the field zero-point off the propagation axis and weakens xy-dispersion. The result is a uniform force in the region of the atoms.

Chapter 5

Experiment Overview

5.1 Even-Lavie cryogenic valve

All supersonic helium beams in this work are produced from a valve developed by Nachun Lavie and Uzi Even[1]. Shown in Figure 5.1, the valve consists of a conical 100 µm opening that flares near the edges and a magnetic plunger that is actuated by a solenoid electromagnet. This arrangement is capable of producing gas pulses as short as 8 µs. Due to the dynamics detailed in Chapter 2 and careful engineering [51], the resulting beam is both brighter and colder than comparable effusive expansions at the expense of an increased forward velocity.

A schematic of the Even-Lavie valve is shown in Figure 5.1. High pressure, high purity helium gas (200-400 psi) is introduced on the left through a 1/16 in stainless steel tube. The pressurized gas is contained within a thin-walled cylinder that is compressed between two Kapton gaskets to create a high-pressure seal. Within the tube the valve is opened via a precision machined plunger that is actuated by a solenoidal electromagnet. During a 12 - 17 A current pulse the plunger is retracted by ∼100 µm from a ∼2 T field to release a brief puff of gas with pulse widths ranging from 8 µs to 50 µs. After the pulse, the plunger is forced closed through a combination

[1] https://sites.google.com/site/evenlavievalve/

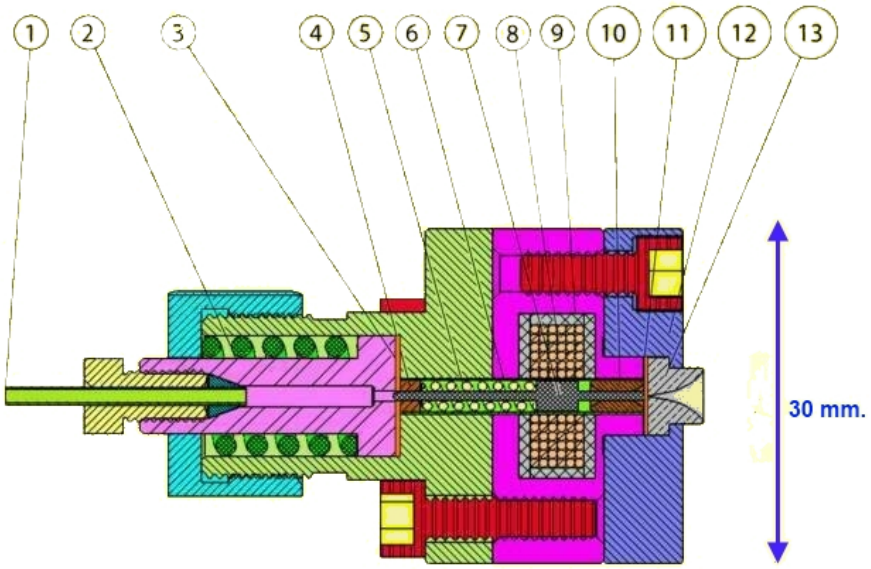

Figure 5.1: Cross section of the Even-Lavie cyrogenic valve [33]: (1) Stainless steel gas inlet tube (1/16 in); (2) Tightening spring (180 N) and pressure relief valve; (3) Kapton foil gasket (rear, 125 µm); (4) Ceramic (Zirconia) guiding ferrule; (5) Return spring (Stainless steel alloy); (6) Thin-walled pressure vessel (stainless steel); (7) reciprocating plunger (magnetic stainless steel alloy); (8) Kapton insulated copper coil; (9) Permedure magnetic shield and field concentrator; (10) Ceramic (zirconia) guiding ferrule; (11) Kapton foil gasket (front, 125 µm; (12) Front flange and valve body (copper); (13) Conical shape expansion nozzle (hardened stainless steel).

Figure 5.2: Cooling the supersonic nozzle with a liquid nitrogen dewar (left) and a helium cyrocooler (right).

of gas pressure and a compression spring.

We avoid operating the nozzle at room temperature for two reasons: (1) the velocity of the gas will be extraordinarily fast in comparison to that of an effusive beam and (2) the fast-moving gas will also be hotter in the moving frame (see Figure 2.2). As detailed in Chapter 2, we can counteract these undesirable effects by cryogenically cooling the nozzle and thus the gas in the valve. Initially, cooling was accomplished by mounting the nozzle to a cold finger on a liquid nitrogen dewar (seen in Figure 5.2 on the left). The dewar was capable of lowering the nozzle temperature to $\sim$100 K. Parallel experiments demanded more stringent velocity requirements and

forced a transition from the dewar to a helium cyrocooler[2] (shown in Figure 5.2 on the right) to further reduce temperatures to as low as 12 K.

At these coolest temperatures, however, helium begins to exhibit cluster growth that limits the cooling effects expected from adiabatic expansion [33]. For this reason we wrapped the cold head of the cryocooler with a flexible Kapton planar heater[3] and heated it via a power supply with roughly 10 W to raise the temperature to 18 K. Below 30 K Type-K thermocouples become unreliable without calibration, so we substituted our thermocouple for a silicon diode[4] to gain both speed and improved reliability. The diode was mounted just above the nozzle on the sloped back side of the clamp seen in Figure 5.2. Thermal noise in the wires was mitigated by wrapping the leads of the diode around the base of the cold head before interfacing with the electrical feedthroughs.

Operationally, pushing towards frigid temperatures requires care with regards to gas line management and materials. Contamination in the tubing can not only cause degradation of the beam but also outright operational failure of the nozzle. While operating at 100 K with liquid nitrogen, it was sufficient to use a high purity cylinder and to pulse the nozzle every few seconds to prevent the plunger from 'sticking' from the condensation of contaminants such as water. Lower temperatures, however, demand more care and attention. It is essential to evacuate the gas line with a pump before cooling. Freezing of various impurities ultimately lead to irreversible

[2]Sumitomo CH-210 10 K cryocooler
[3]Omega Kapton Insulated Flexible Heaters
[4]Lake Shore Cryotronics DT-670 silicon diode operated with a Model 211 Temperature Monitor

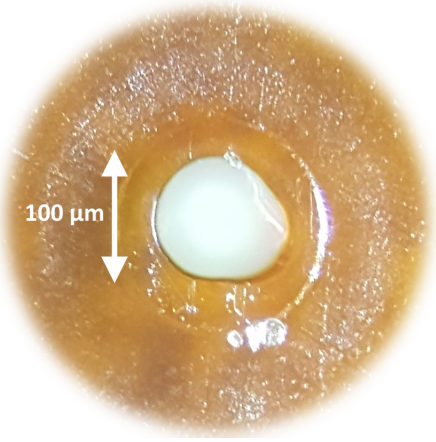

Figure 5.3: Example of a gasket failure. This gasket (item (11) in Figure 5.1) sealed the front of the nozzle as noted by the slightly visible circular indentation near the opening. The deformation seen on the lower right prevented the plunger of the nozzle from creating a flush seal against the Kapton thus causing a leak. This is an example of poor quality Kapton.

damage of the gaskets requiring disassembly[5] of the nozzle for gasket replacement. Furthermore, due to variations in Kapton manufacture, it is possible for certain lots of gaskets to degrade prematurely in a matter of hours. See Figure 5.3 for an example of a failure representative of poor quality Kapton. High quality Kapton will create seals easily lasting for months and hundreds of thousands of pulses.

5.2 Atomic source

Over the evolution of our experiment and its many goals, we used a variety of sources and means to introduce atomic lithium into our supersonic beam. Initial entrainment investigations were conducted through ablation of lithium from a solid

[5]Manual to the Even-Lavie nozzle

target with a pulsed laser[6]. In a parallel project whose goal was to push the limits of entrainment, we abandoned laser ablation due to poor flux and lithium clustering and instead adopted an effusive lithium source where we heat a sample of lithium to produce a flux via the vapor pressure.

5.2.1 Directional oven

Incorporating lessons learned from previous oven designs, we transitioned from non-standard custom parts to standard ConFlat (CF) flange dimensions for simplicity and versatility. Furthermore, we chose to place all heating elements within vacuum in order to avoid excessive insulation and cooling that is required with out-of-vacuum heating.

The reservoir dimensions were set to an inner diameter of 1.6 in and an inner length of 3.2 in for a total volume of 6.4 in^3 to accommodate the lithium rods[7] (equivalent to roughly 50 g of lithium). The oven reservoir terminates with a standard 1.33 in CF flange pattern for mounting of different exit apertures. The base of the oven has five fins with through-holes for easy mounting.

5.2.2 Directional aperture

Rather than use a simple singular opening for the output of the oven, we were inspired by directional oven designs [52] that minimize the atom flux off the directional axis of the oven. These designs are based on the early work by King and

[6]Continuum Minilite II (now Amplitude Laser)
[7]ESPI metals lithium rods

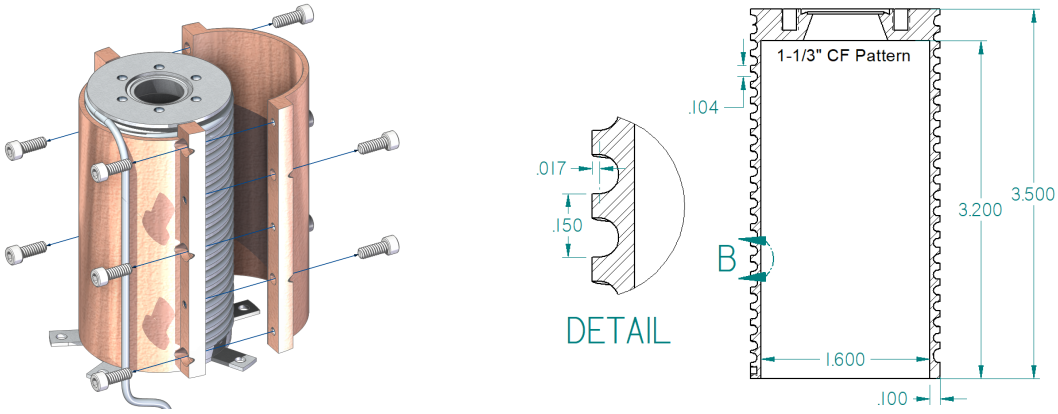

Figure 5.4: Oven reservoir for lithium. The source consists of a stainless steel reservoir with a helical groove on the outer surface. Heater wires are wound in the groove and held fixed with a copper clamp. The opening of the reservoir terminates with a standard tapped and bored 1.33 in CF flange.

Zacharias [53] who constructed a matrix of channels through stacking of corrugated nickel foils. By choosing the channel diameter such that the mean free path is greater than the channel length, then the angular spread of the flux is determined by the channel's aspect ratio [54]. Due to the large aspect ratios of the channels, flux is diminished in comparison to that of a pinhole of the same channel diameter. Atoms that enter the tube are highly likely to exit at the entrance. The channel will preferentially allow only the highly directional atoms to escape. By making a large matrix of these channels we can counteract the loss of atoms due to the geometry.

Our design, shown in Figure 5.5, uses 2485 pieces[8] of 33 RW gauge (200 µm diameter) hypodermic tubing sourced from MicroGroup cut to 5 mm lengths. We hexagonally packed the tubing into a triangular groove cut into the center of a

[8]Feel free to count. The resolution is sufficient.

Figure 5.5: Image of the assembled nozzle of the directional oven. Within the triangular cutout are 2485 capillaries in a hexagonal packing arrangement and are fixed with a small clamp.

1.33 in custom CF flange to facilitate optimal circle packing. The physics machine shop used an electrical discharge machine to create the sharp 60 deg groove. The tubing is held in place via small wedge which applies pressure via two #4-40 set screws (see Figure 5.6 for more details). We opted to use nuts rather than tapping the stainless steel as previous experience showed that screws tend to gall and become stuck after many heating cycles. This design allows removal of the screws with an end mill machine in the event of a worst-case situation. Furthermore, we coated the screws with a boron nitride aerosol for lubrication and galling prevention. Boron nitride can both withstand temperatures up to 850 °C and suffers minimal outgassing in vacuum.

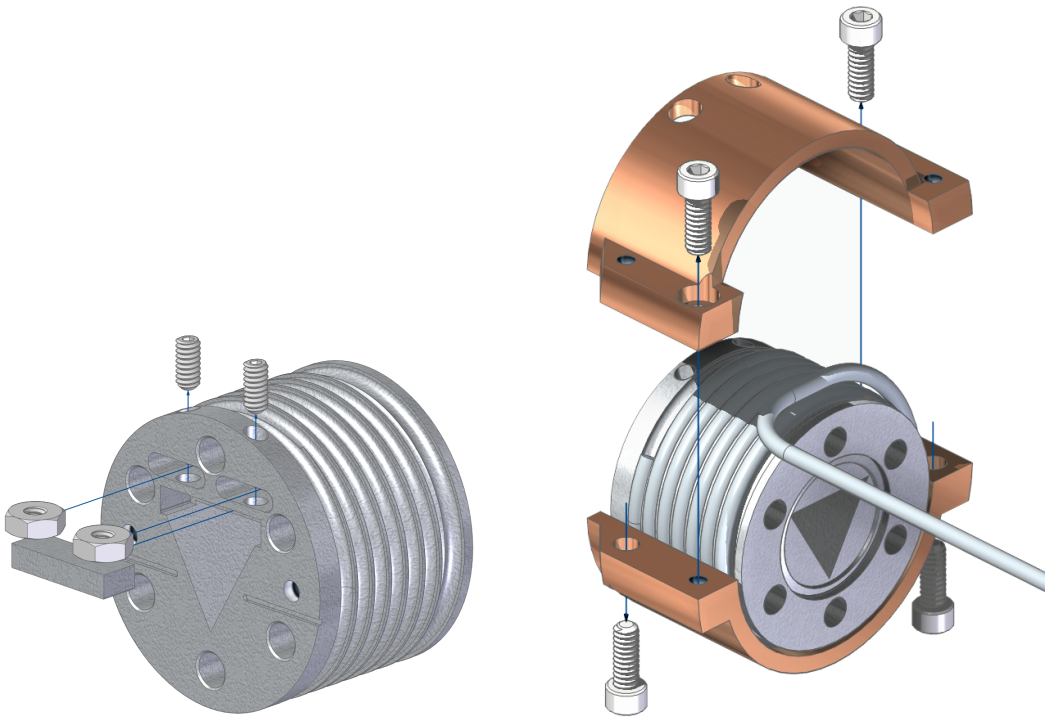

Figure 5.6: Design of the direction nozzle for the reservoir. The nozzle is composed entirely of stainless steel and also features a 1.33 in CF flange at the base for interface to the reservoir. Similar to the reservoir, a helical groove is used to wrap a heater wire around the nozzle for independent control of nozzle temperature. Copper clamps hold the heater wire fixed. The nozzle is typically kept 50 °C greater the temperature of the reservoir in order to prevent clogging. The triangular cutout in the center is filled with hexagonally packed microtubes used to preferentially select more directional atom flux. The tubes are held fixed with a small block that applies pressure via two #4-40 set screws. A small groove on the face of the nozzle allows for secure mounting of a Type-K thermocouple for temperature monitoring.

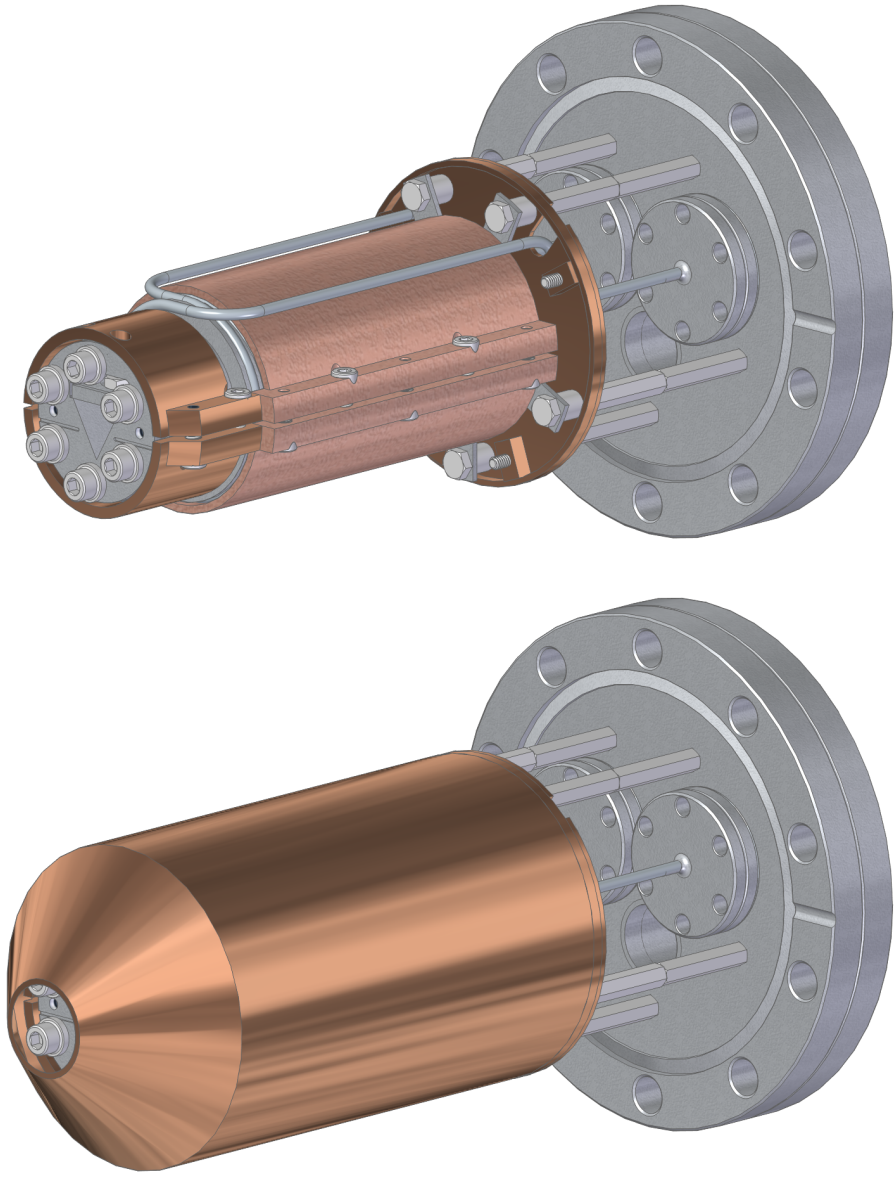

Figure 5.7: Fully assembled oven. The oven mounts on 5 stainless steel standoffs affixed to a 4.63 in CF flange. Ceramic screws and alumina spacers provide thermal isolation for all directly connected structural supports. A copper heat shield surrounds the oven to prevent radiative loss.

Alignment of the tubing was *problematic*[9] for several reasons. We fabricate a triangular mandrel to plug the hole and create a working surface to support the tubes during assembly. Tilting the nozzle slightly upward and using gravity allows the tubing to self-align for the initial ~ 20 layers. After completing the initial layers the risk of dropping tubes into the vacant recess is an issue. This risk is alleviated somewhat by clumping many of the tubes with surface tension after sonication in water. Circle packing defects and vacancies are easily fixed with dental probes, and *non-magnetic*[10] tweezers.

Both the reservoir and nozzle of the directional oven are heated with flexible heater cables[11]. The two cables, composed of a resistive wire embedded within magnesium oxide, are enclosed in Inconel 600 sheaths that are wrapped around the diameters of the reservoir and nozzle of the oven. Both cables terminate with a 1.33 in CF flange oriented such that the knife edge is facing the electrical connections of the heater. This choice allowed us to remove the oven from the chamber for maintenance and lithium replenishment without unwinding the heater assembly.

5.3 Beam line and optical pumping

Shown in Figure 5.8 is a cross-sectional outline of the beam line inside the vacuum system. Included is everything from the production of helium and lithium to the magnetic kick at the coils. The Even-Lavie nozzle is mounted on a cyrocooler

[9]Substitute any of the following: annoying, aggravating, *infuriating*.

[10]All tubing is Type 304 stainless steel, so it is *very* easy to pull out roughly 2000 tubes by accident... twice.

[11]AeroRod heaters were sourced from ARi Industries Inc.

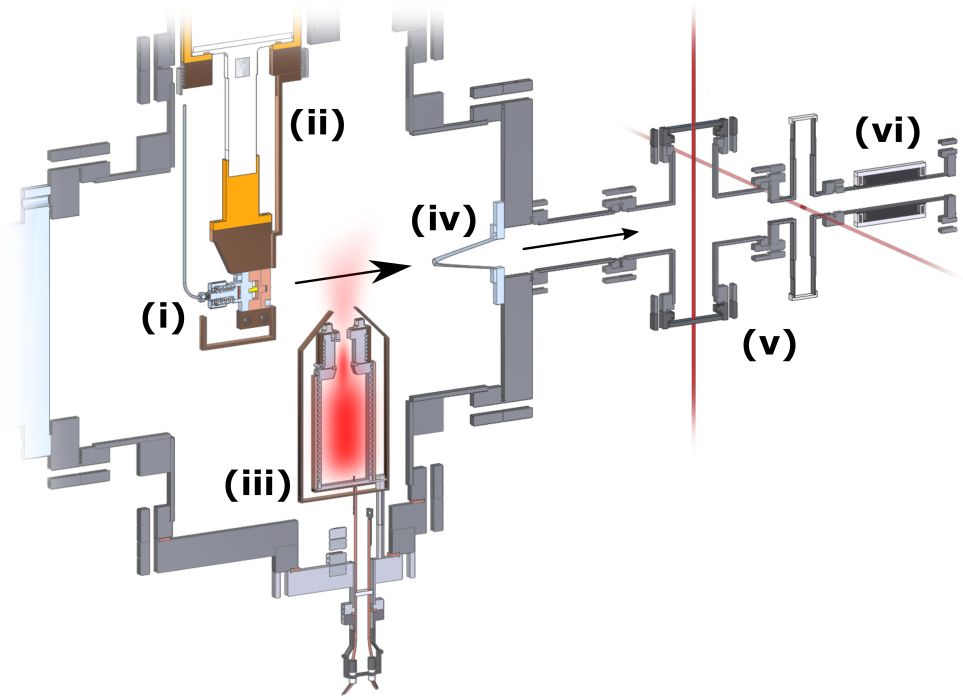

Figure 5.8: The helium beam originates from a supersonic nozzle (i) cooled by a 10 K cryocooler (ii). The helium beam passes through a cloud of lithium created by a directional oven (iii) and entrains lithium into the flow. To prevent heating of the nozzle from the oven, copper shields surround both the oven and the nozzle with the latter also being cooled by a separate 60 K high-load base of the cryocooler. The helium and lithium mixture passes through a 5 mm skimmer (iv) and enter a region of optical pumping (v) for state selection. Finally, the beam is kicked by the set of coils in (vi) before continuing towards detection (not shown).

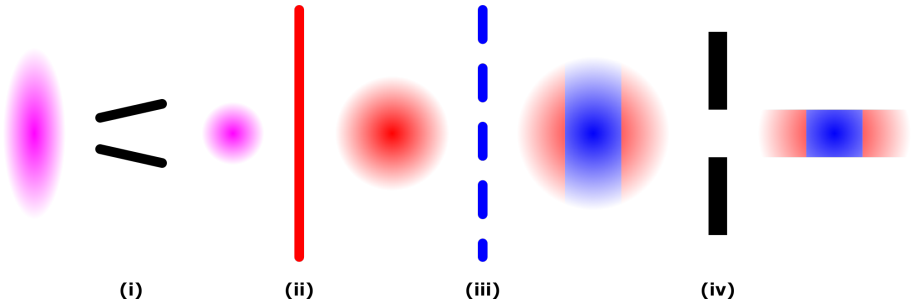

Figure 5.9: State preparation of the lithium cloud before entering the magnetic coils. Initially the beam is a mix of both $2S_{1/2}$ F = 1 and 2 states. The beam passes through a 5 mm skimmer (i) before encountering a laser (ii) tuned to remove all atoms in the beam from the F=1 ground state. The second laser (iii) then pulses 15 µs to transfer a longitudinal slice of the beam back into the F=1 state. Tagging only a narrow slice of atoms will reduce the effects of field inhomogeneities present near the wings of the electromagnets. Finally, the beam is spatially cropped with a 5 mm pinhole (iv) machined into a CF gasket.

and suspended along the central axis of a 10 in stainless steel CF chamber. Below the axis of the nozzle and slightly offset (6.25 cm) along the propagation axis, the oven is oriented facing upward to dose passing helium. Heat from the 550 °C oven is managed by copper heat shields on both the oven and cryocooler. A 5 mm skimmer[12] is placed 17.5 cm away from the nozzle face relative to its knife edge to select the cold interior of the supersonic beam while also providing the added benefit of differential pumping.

The lithium passes through a series of CF crosses where both the spatial and magnetic states of the atoms are prepared. This preparation process is illustrated in Figure 5.9. The lithium produced by the oven occupies all the m_F sublevels in the $^2S_{1/2}$ ground state. We first use a sheet of laser light tuned to the $F = 1 \rightarrow F' = 2$

[12]Beam Dynamics model 50.8 nickel skimmer

D1 transition to empty and clean the high-field-seeking $2S_{1/2}$ F=1 state from the entire spatial extent of the lithium beam. The second laser sheet, tuned to the $F = 2 \rightarrow F' = 1$, is then flashed for 15 µs to transfer a thin slice of the expanding lithium back into the $2S_{1/2}$ F=1 ground state. Laser light for both optical pumping stages was set above the saturation intensity of lithium at 7.59 mW/cm^2. Finally before entering the magnetic coils, the diameter is further culled by a 5 mm pinhole situated 44 cm away from the nozzle face. The pinhole was machined from a blank 2.75 in copper gasket.

5.4 Laser system

Our system consists of two commercial grating-stabilized external-cavity diode lasers[13] (ECDLs) and a tapered amplifier[14]. A general outline of the optical elements used to stabilize and select the frequencies is shown in Figure 5.10. The separate ECDL (spectroscopy laser) is used solely as a frequency reference, while the other laser is used to seed the tapered amplifier for power amplification. Much of the locking electronics and optics were based on the designs from previous experiments within the lab and further details can be found in other dissertations [46, 55, 56].

We stabilize the frequency of our spectroscopy laser through frequency modulation spectroscopy using ^{7}Li D-lines as a reference [57]. Output from the spectroscopy laser is elevated before passing through a pair of anamorphic prisms to correct for astigmatism in the beam shape. The beam passes through an optical

[13]Toptica Photonics DL pro and a seed laser within the TA pro
[14]Toptica Photonics TA pro

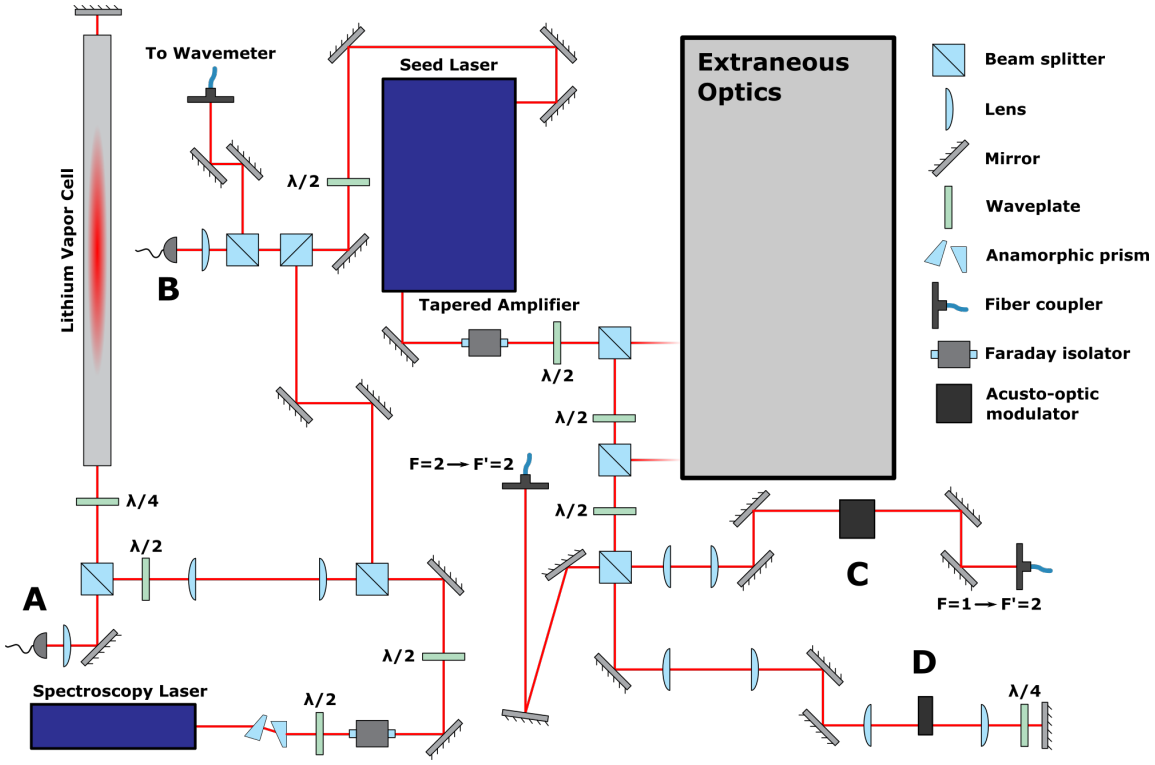

Figure 5.10: Laser system used for state preparation and measurements. (A) The spectroscopy laser double-passes through a lithium vapor cell in order to stabilize the frequency to the ^{7}Li D1 line. (B) We superimpose the spectroscopy and seed lasers onto a photodiode to generate a beat frequency. The frequency is then used to create an error signal that determines the frequency offset between the two lasers. (C) A 95 MHz acousto-optic modulator (AOM) shifts the frequency to F=1→F'=2 D1 transition. (D) A 420 MHz AOM is double-passed to produce the ∼800 MHz offset necessary to necessary to reach the F=2→F'=2 D1 transition. The RF source of both AOMs can be switched to pulse the laser.

isolator[15] to prevent reflections from subsequent optics from re-entering the ECDL and causing feedback in the laser diode. A half-wave plate and a polarizing beam-splitter cube are used to split the laser into two branches. One branch is allowed to double-pass through a lithium vapor cell before being collected on a photodiode that is used to feedback and stabilize the spectroscopy laser. The diverted branch is merged with the seed laser generated within the tapered amplifier and is collected by another photodiode. The output of this photodiode is sent through a series of electronics to extract a beat frequency that can be used to lock the frequency of the tapered amplifier relative to the spectroscopy laser.

The lithium vapor cell consists of a long stainless steel tube with two 2.75 in CF viewports at each end and has a section in the middle that protrudes outward where lithium (natural abundance) is contained. Heating this section in excess of 400 °C will produce a lithium vapor pressure that will absorb a sufficient portion of light to be detectable on our photodiode. To prevent coating of the end viewports with lithium we initially evacuate the vapor cell of all gas through a roughing pump at room temperature and introduce argon into the cell to the level of 35 mTorr. This small amount of buffer gas is sufficient to prevent lithium from traversing the length of tube to the viewports.

To lock our laser to a fixed transition in the ^{7}Li spectra we create an error signal through the addition of frequency sidebands by adding a modulation to the diode current. We use a photodiode to monitor the spectroscopy laser intensity after

[15]Conoptics Inc. 712B Optical Isolator

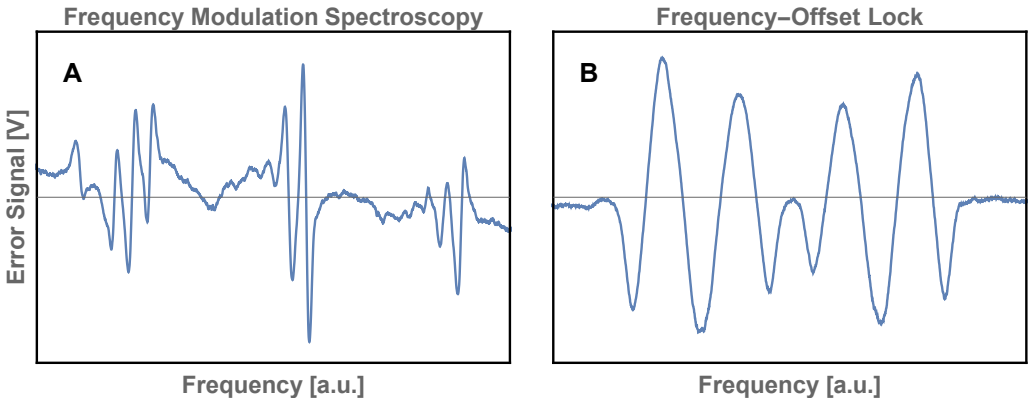

Figure 5.11: Error signals generated for stabilization of the spectroscopy and seed lasers. (A) The spectroscopy laser error signal after double-passing through a lithium vapor cell. Zero-crossings correspond to features of the ^{7}Li D1 line. (B) We generate a beat frequency by overlaying the spectroscopy laser and seed laser onto a photodiode. This frequency is then mixed with a known frequency from a voltage-controlled oscillator. The mixed output is split and recombined after one branch of the output is passed through a fixed phase delay. This results in an error signal whose zero-crossings provide particular detunings between the spectroscopy and seed lasers.

double passing through the vapor cell. Initially, we sweep the central frequency of the laser by applying a triangular waveform on the piezo to adjust the cavity length in order to identify a specific locking frequency. The photodiode signal is passed through a series of electronics detailed in [46, 55] and the resulting error signal is shown in Figure 5.11. The zero-crossings of this error signal correspond to the spectral features of the ^{7}Li D1-line.

After stabilizing the spectroscopy laser to a transition, we then reference the seed laser of the tapered amplifier to the spectroscopy laser via a frequency offset lock by superimposing the two lasers onto a photodiode [58]. Similar to the spectroscopy laser we apply a voltage ramp on the piezo of the seed laser to produce

a beat frequency on the photodiode. We then mix the beat frequency with the output of a voltage-controlled oscillator (VCO) through a frequency mixer. This output is split and recombined on a phase detector after one branch passes through a cable of a known delay length. This recombination will produce an error output as seen in Figure 5.11 where the zero-crossings correspond to the detunings between the spectroscopy laser and the seed laser. Each of these detunings can be shifted through adjustment of the voltage applied on the VCO allowing for precise targeting of frequency.

The output of the tapered amplifier is first passed through an optical isolator to again reduce feedback and protect the amplifier chip. The laser passes through a series of polarizing beam splitters that direct the light to other optics for parallel experiments. For this experiment the $\lambda/2$ waveplates were set to avoid loss on these branches during operation. At the final polarizing beam splitter cube the laser is split into two branches. Locking the tapered amplifier will introduce a frequency offset away from the ^{7}Li D1 transition. We address this by shifting the frequencies of the two branches with two different acousto-optic modulators[16] (AOM). The upper branch in Figure 5.10 simply shifts the frequency back onto the $F = 1 \rightarrow F' = 1$ resonance before coupling into a fiber. In order to address the large (803.5 MHz) offset of the ^{7}Li $^2S_{1/2}$ ground state, we double-pass through a 420 MHz AOM to double the frequency shift accumulated before coupling into a fiber. Both AOMs can be adjusted in the range of $\pm$20 MHz with the RF-source controllers to target the specific transitions shown in Figure 3.2.

[16]IntraAction models ATM-951A1 and ATM-420

5.5 Fluorescence

An illustration of the detection portion of the vacuum system is shown in Figure 5.12. After the coils are pulsed, lithium is allowed to travel through the vacuum system in order to let the deflection and spreading of the lithium cloud evolve in time. Lithium propagates either 40 cm or 58.5 cm before it arrives at the first detection chamber or second detection chamber respectively. A narrow 2 mm laser beam crosses orthogonal to the beam line through a 2.75 in or 4.5 in vacuum cross respectively. The laser is tuned to the $F = 1 \rightarrow F' = 2$ D1 transition in order to excite the thin slice of tagged lithium atoms mentioned in section 5.3. The rest of the cloud remains in the $^2S_{1/2}$ $F = 2$ state and will not interact with the laser nor measurement of lithium. The excited atoms will spontaneously decay and produce a fluorescence signal proportional to the total number of atoms crossing the beam. As the atoms travel through the laser we will also receive temporal information of the atom number in what is commonly referred to as a time-of-flight measurement. We collect a portion of the spontaneously emitted light with a lens after leaving the vacuum chamber. This light is focused onto a fast, highly sensitive avalanche photodiode[17] (APD).

In order to extract more spatial information of the beam the laser light is configured to translate perpendicular to the laser and beam line. We accomplish this by reflecting the excitation laser off of a mirror mounted on a linear slide assembly[18]. Translation is automated through stepper motors driven by commercial

[17]Hamamatsu C5460-01 APD module
[18]Velmex Motorized UniSlide Assembly

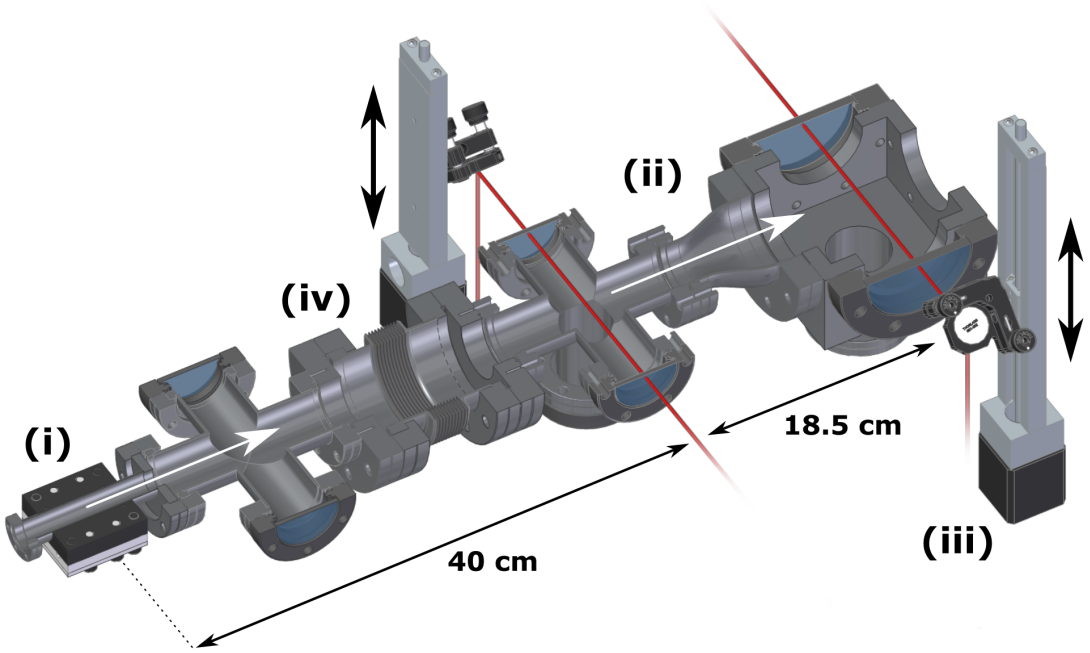

Figure 5.12: Beam line of fluorescence detection. After the lithium is kicked by the coils (i) it is allowed to propagate freely for either 40 cm or 58.5 cm before entering the first or second detection chamber (ii) respectively. Laser light excites the lithium passing through and is collected by avalanche photodiodes (not shown) mounted above the vacuum crosses. Automated linear motion mounts (iii) translate the mirrors vertically to reflect the laser through different sections of the lithium beam to produce time-of-flight line cuts of fluorescence. A bellows (iv) separates the detection chambers from kicking coils. Both detection chambers are mounted on a large homebuilt translation stage capable of shifting both chambers back 5 cm.

stepper controllers[19] and controlled via LabVIEW.

5.6 Summary of apparatus

Figure 5.13 summarizes the entire apparatus. The beam line begins at the top of the image and travels downward. A supersonic helium beam is produced from an Even-Lavie nozzle and entrains lithium emitted from an effusive oven. The helium and lithium mixture passes through a skimmer before the lithium magnetic state is prepared with two lasers. The coils pulse and deflect the beam which is then measured at two different locations via fluorescence collected on an avalanche photodiode. The final chamber consists of an assortment of diagnostic equipment not relevant to this experiment.

[19]Velmex produces the VXM series of stepper controllers with drivers for many programming languages.

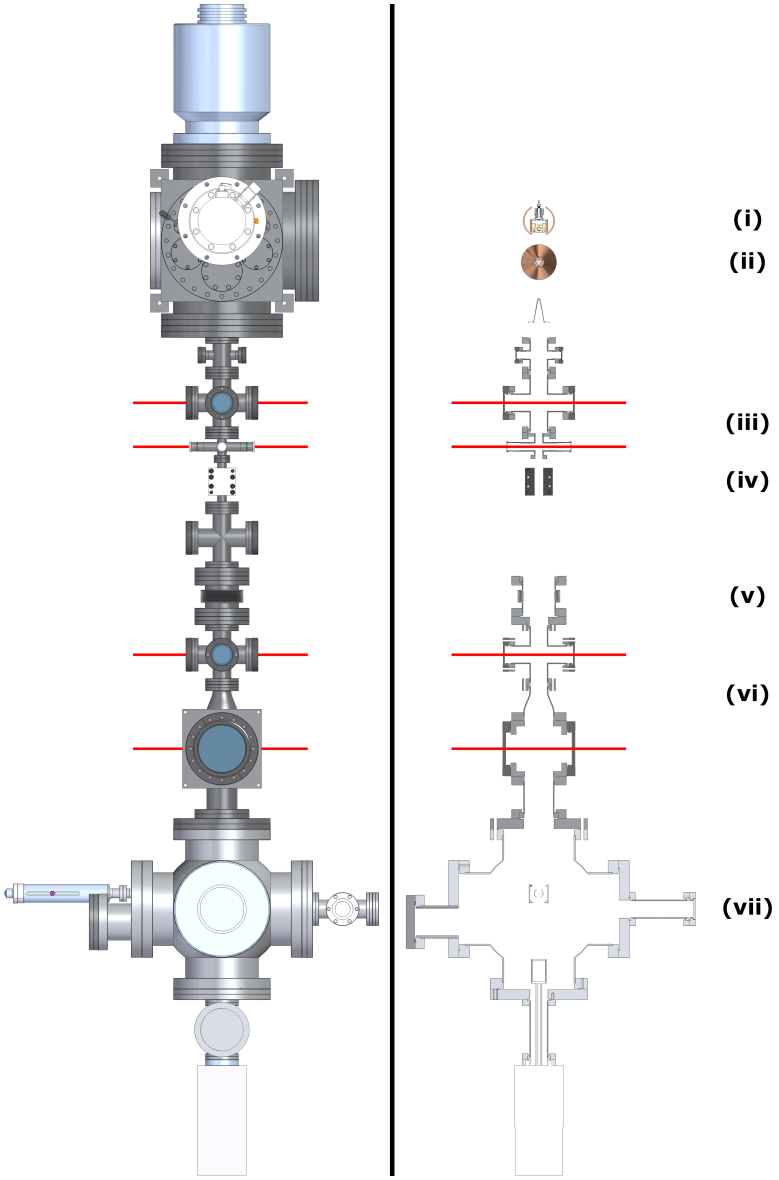

Figure 5.13: Complete experimental setup. The beam line consists of a supersonic helium source (i), a lithium entrainment oven (ii), optical pumping to select the atomic state (iii), and the bias and kicking coils (iv). A flex bellows (v) is included to allow adjustment of the fluorescence lasers (vi). The final chamber (vii) includes a Langmuir-Taylor surface ionization detector and residual gas analyzer for further diagnostics.

Chapter 6

Measurements

6.1 Imaging lithium

We accumulate a series of many fluorescence time-of-flight measurements to characterize the lithium cloud's expansion and deflection. These measurements are compiled together to form a two-dimensional time-of-flight density image similar to that of Figure 6.1. By rotating the coils 90 deg around the vacuum chamber we can capture the effects of the other axis and produce a full three-dimensional snapshot (one temporal and two spatial components) of the lithium for a given kick configuration. After propagating nearly 50 cm from the 5 mm pinhole the lithium cloud has a transverse extent typically of ~ 1 cm and temporal range from 50 µs to 300 µs depending upon the state preparation.

6.2 Optical tagging

Using the acousto-optic modulators detailed in Chapter 5 we can independently toggle the laser light on and off by adding or removing the RF source. We exploit this aspect during the second optical pumping stage during state preparation in order to highlight a thin longitudinal slice (see Figure 5.9) of the lithium cloud for fluorescence imaging along the propagation axis. Tagging proved to be a useful

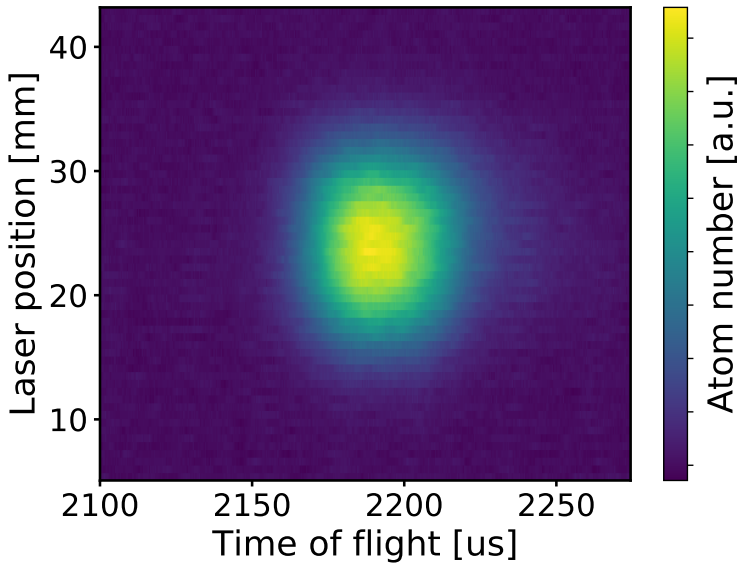

Figure 6.1: False color time-of-flight fluorescence images of lithium. The image is composed of 61 time-of-flight traces at laser positions spaced 0.025 in apart.

means of selecting the comparatively colder interior longitudinal temperatures of the beam. Three different tagging lengths are summarized in Figure 6.2 along with their corresponding full width at half maximum (FWHM) values. All measurements that follow use a 15 µs pulse length to maximize the fluorescence current signal on the APD without tagging a large portion of the cloud.

6.3 Extracting beam parameters

After the aforementioned optimizations of the previous section, we systematically extract the beam properties from the time-of-flight density plots. Fitting the

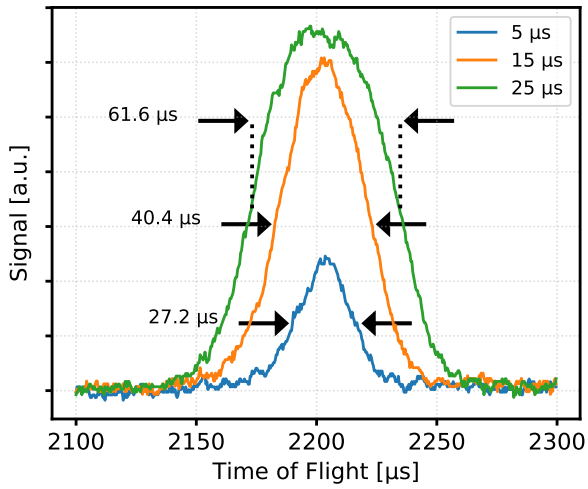

Figure 6.2: Time-of-flight plots of different optical tagging lengths. The laser was set on the center of the lithium cloud and tagged at the peak signal. Optimizing the tagging length is a balance between achieving a sufficiently large signal while minimizing the effects of field inhomogeneities from affecting the cloud during propagation. The FWHM width for each signal is indicated.

data to a two-dimensional normal distribution

$$f(t,x) = A\exp\left[-\frac{1}{2}\left(\frac{(t-t_0)^2}{\sigma_t^2} + \frac{(x-x_0)^2}{\sigma_x^2}\right)\right], \tag{6.1}$$

we extract, specifically, four parameters of the beam: the temporal cloud center t_0, the temporal spread radius σ_t, the spatial cloud center x_0, and spatial spread radius σ_x. An example of such an analysis is shown in Figure 6.3 on a freely propagating beam with the various fitting parameters summarized for each imaging location. As expected, the beam expands both in time and space as it propagates from the first detection location to the second along the beam axis. The closer measurement at 40 cm was compiled from 41 TOF traces whereas the farther 58.5 cm measurement combines 63 traces. The different number of traces reflects the optical access provided by the 2.75 in and 4.5 in viewports of the first and second detection chambers respectively (see Figure 5.12). The range of laser positions in the first chamber is restricted as a result.

6.4 Two-point measurements: kicks and thermal spreading

We start first with the more straightforward of the two measurements - the kick. The kick is simply a measure of the strength of the impulse imparted by the pulsed magnetic coils. Unconcerned with the overall shape of the cloud at this stage, we calculate the velocity of the center of the lithium cloud from the fitted normal distribution. Each kick measurement is referenced to a freely propagating beam of similar conditions. Being only specifically interested in the change in velocity Δv in both transverse directions created by the coils, we use the two imaging locations in

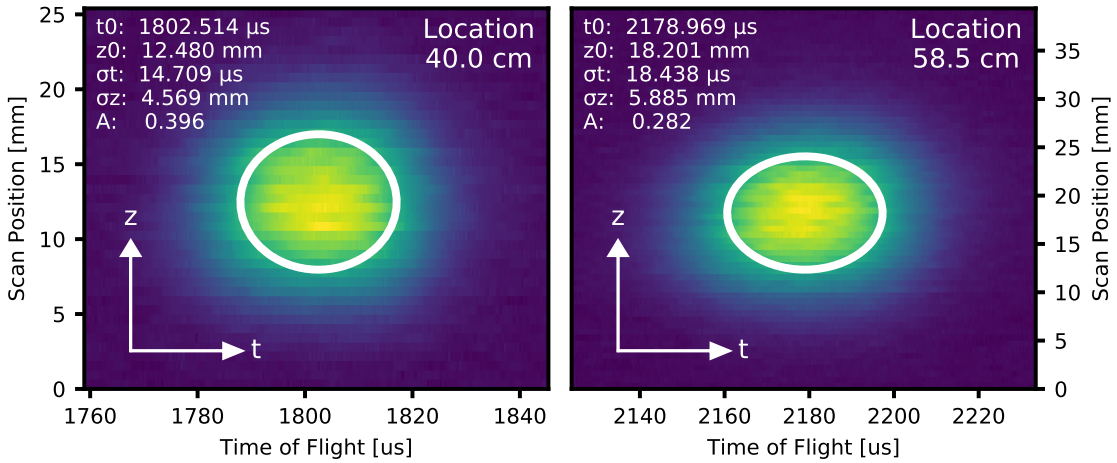

Figure 6.3: Extracting beam parameters from fluorescence time-of-flight images of lithium. Fluorescence data was taken 40 cm and 58.5 cm away from the center of the kicking coils. A two-dimensional normal distribution is fitted to the data to extract the various parameters summarized in the upper left of each image. The white ellipses superimposed on the data represent the 1-sigma radii of the fits using the extracted parameters σ_t and σ_z from each image according to Equation 6.1.

our experiment at 40 cm and 58.5 cm to calculate Δv via a simple difference quotient

$$\Delta v = \frac{z_2 - z_1}{t_2 - t_1} \tag{6.2}$$

where the indices indicate the two measurement positions.

The second measurement, the thermal spreading, is more involved and hides some complexity. We know from Chapter 2 that the beam will expand following

$$\sigma(t) = \sqrt{\sigma_0^2 + v_{th}^2 t^2}\,, \tag{6.3}$$

where the σ_0 and $\sigma(t)$ represent the Gaussian width of the beam initially and after time t respectively. In principle, if the beam has been allowed to expand across a long distance, the initial size will cease to be a dominant factor and growth in σ will be proportional to $v_{th}t$. Under such conditions a similar difference quotient would be sufficient to extract the thermal velocity. To be conservative, we instead make use of Equation 6.4

$$v_{th} = \sqrt{\frac{k_{\mathrm{B}}T}{m}} = \sqrt{\frac{\sigma_2^2 - \sigma_1^2}{t_2^2 - t_1^2}}\,,$$

to extract the thermal velocity where k_{B} is the Boltzmann constant, m is the mass of lithium atom, T is the transverse temperature, and $\sigma_{1,2}$ are the transverse widths of the lithium cloud at times $t_{1,2}$ since passing the skimmer.

6.5 Adding pulsed magnetic fields

Using the current pulsing circuitry of Chapter 4 we systemically apply different currents to the electromagnet coils as the lithium travels through the coil centers.

While all of the circuit components are rated to handle at least 1 kV, we limit voltages to a max of 800 V in order to preserve the coils and circuitry. Furthermore, during initial stress testing at 1 kV, equipment in the vicinity of the pulsing box was coupling to the capacitor bank as it was charged and discharged. This led to sporadic triggering of LabVIEW and misfiring of the supersonic beam.

In order to examine the qualitative behavior of the kick from a purely dispersive force to the regime of one-dimensionality we allow the bias field to vary from being completely disabled to exceeding that of the anti-Helmholtz gradient fields. For this reason, we set the anti-Helmholtz kicking coils to fixed pulsing voltages at 600 V. This allows us the freedom to select bias voltages ranging from 0 to 800 V, thus satisfying the aforementioned desired conditions.

To illustrate the qualitative effects of the two kicking regimes, refer first to Figure 6.4. This shows a time-of-flight density plot of the lithium cloud measured at the far detector to highlight any expansion and/or deflection Δz from the freely expanding reference beam. The left plot is of the freely expanding beam, whereas the right plot shows the current conditions where only the kicking coils are activated. For ease of comparison the centroid of the freely expanding lithium cloud is projected onto the kick as a red dot. The blue dot similarly indicates the centroid of the kicked beam. The most apparent difference between the two is the noticeable increase in transverse radius (1.7 mm) that is expected from a purely dispersive gradient field. Though slight, there is small displacement of centroid that could be the result of either coil or beam misalignment.

The regime of one-dimensionality plotted in Figure 6.5 reflects the same ex-

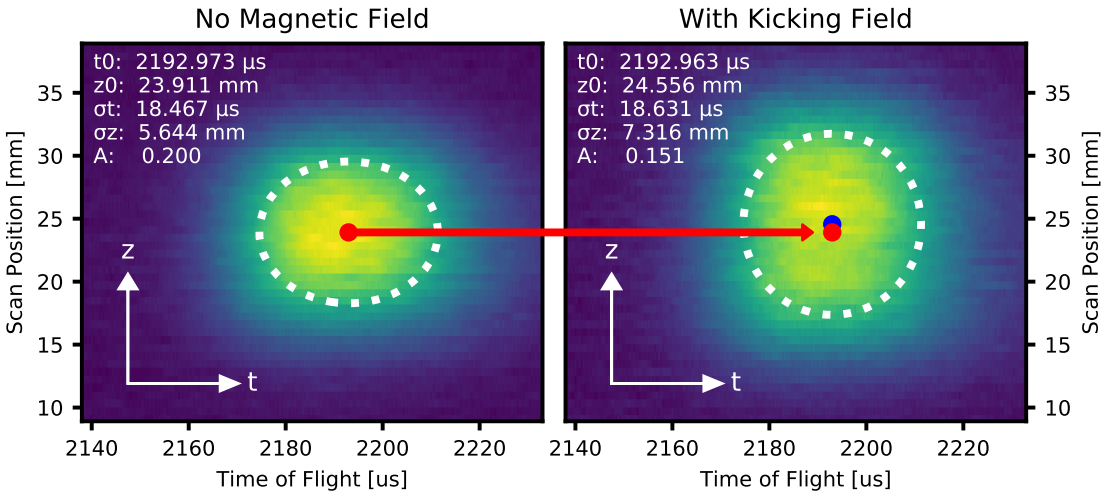

Figure 6.4: Demonstration of a dispersive kick with both bias coils disabled and the kicking anti-Helmholtz coil pair both set at 600 V. The plots contrast a freely propagating cloud to one undergoing a dispersive kick, revealing a sizable increase in the transverse radius σ_z.

perimental conditions as the dispersive kick with the following exception; the bias coil is now set at its maximum of 800 V to produce the strongest deflection Δz capable in our current system. Under these conditions we see a strong deflection (blue dot) of $\sim$3.5 mm. The distinguishing characteristic besides the deflection is that transverse heating has been suppressed as seen by the smaller σ_z value.

Rather than analyze each density individually, we process and compile all of the fitting parameters into values for the kick Δv and the spreading Δv_{th}. We focus specifically on the changes in v and v_{th} to highlight the effects our coils introduce on the beam. Measurements were taken from 0 to 800 V in increments of 100 V to adequately see the transitions from a dispersive kick to one-dimensionality. Furthermore, measurements for both orthogonal transverse directions were collected via

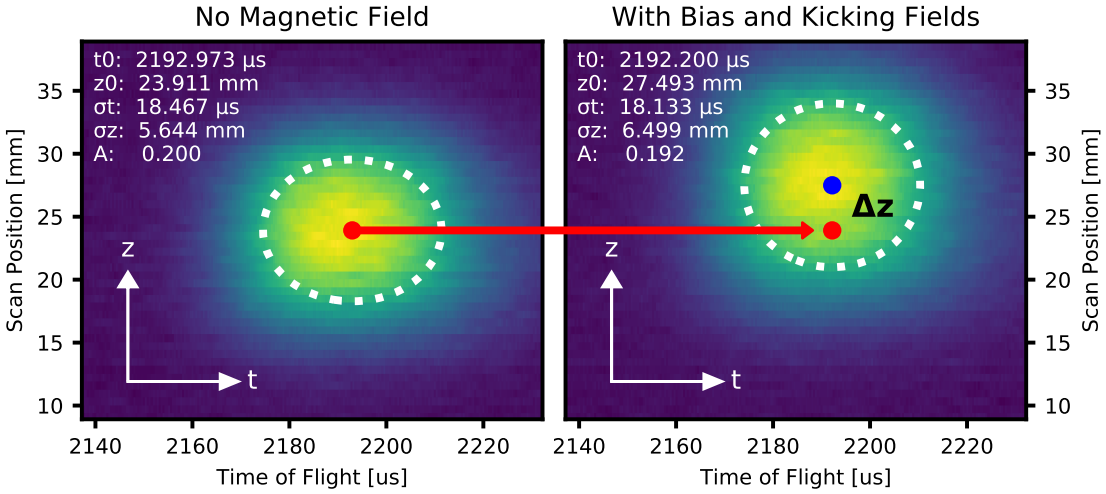

Figure 6.5: Demonstration of one-dimensional kick with one bias coil set to 800 V and the kicking anti-Helmholtz coil pair set both to 600 V. The left plot contrasts a freely propagating beam to a one-dimensional kick on the right revealing a sizable transverse shift Δz while reducing heating as seen in Figure 6.4.

rotation of the kicking coils 90 deg around the beam axis (see Chapter 5). Each data point accumulates three separate measurements to produce an estimate on the error of our measurement. These results are summarized in Figure 6.6.

We focus first on the z-axis (rightmost column) where the kicking coils are aligned. The preceding qualitative discussion for the limiting cases is still valid. As expected, no noticeable kick is observed at zero bias, but as the magnitude of the bias voltage is increased, stronger kicks are observed along the z-axis. A maximum kick of $\Delta v = 2.5 \pm 0.3(-2.3 \pm 0.3)$ m/s at +800(-800) V bias has been achieved, constrained only by the limits of the electronics. The change in thermal velocity peaks around low biases at 1.2 ± 0.1 m/s and tapers off at high biases to 0.5 ± 0.1 m/s at +800 V and 0.6 ± 0.1 m/s at -800 V.

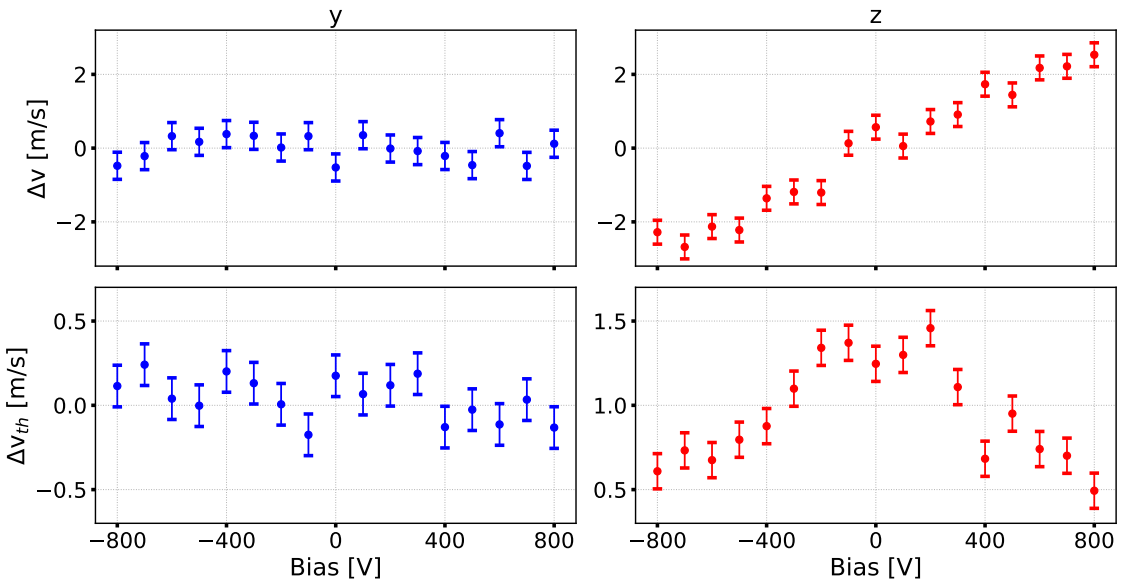

Figure 6.6: Transverse kick strength and change in thermal velocity for the two orthogonal directions are shown as a function of bias coil voltage. Note the vertical axis of two lower Δv_{th} plots are the same scale, however the values are offset.

These results are consistent with the conceptual idea that the bias field shifts the zero-crossing of the total magnetic field (see Figure 4.15). The magnetic moments of the individual atoms align along the field lines, which sets the directionality of the applied force $\mathbf{F} = \mu\nabla|\mathbf{B}|$. The magnitude of the total magnetic field only influences the strength of the kick.

Shifting focus to the other orthogonal transverse axis (y-axis) shows no apparent dependence on the bias field for either Δv or Δv_{th}. Kicks along this axis remain small over all voltages not exceeding 0.5 m/s. Likewise, thermal velocity changes are negligible with no apparent structure.

Worth noting, due to the bias configuration employed, the kick will continue to grow with increasing bias field. This side-effect is a result of the creation of a bias field from that of a single coil. Unlike a Helmholtz field, where total magnetic field is constant, a single offset coil will always have an associated magnetic gradient that will impart its own kick to the cloud. If a uniform field was substituted, we would expect kicks to eventually saturate to some fixed value corresponding to the gradient of the anti-Helmholtz pair.

Everything discussed so far is a result of direct spatial measurements obtained via laser scans and their corresponding fluorescence values. However, given that all the data are time-of-flight measurements, we still have access to the temporal shape of the beam as it passes through the laser. Using the distances between the measurement points (18.5 cm) and the time-of-arrival of the freely propagating beams we can calculate the velocity of the lithium beam (498 ± 0.3 m/s) and determine the spatial extent of the cloud along the propagation axis. We can repeat the kick

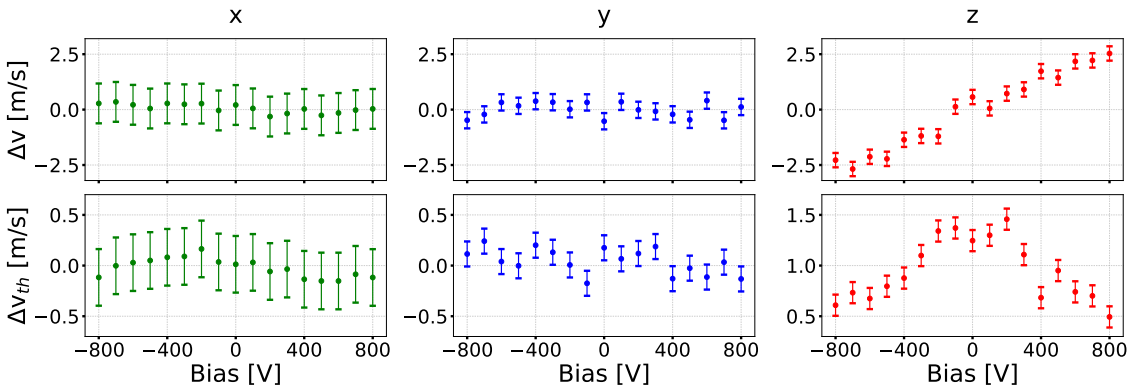

Figure 6.7: Dependence of the change in velocity and thermal velocity of the lithium atoms on bias voltages in three dimensions. Data along the x-axis is extracted from the temporal time-of-arrival of the lithium beam. The changes in velocity are reported relative to the beam with no magnetic fields present. The kicking gradient is oriented along the z-axis.

and heating analyses as previously done on the transverse axes but now on the propagation x-axis. The full three-dimensional results are summarized in Figure 6.7.

Considering the aggregate data, a kick will only impart a net force on atoms along the axis of the anti-Helmholtz pair (z-axis) without influencing trajectories on the other axes. Similarly in the presence of a high bias field, heating is greatly suppressed along axes orthogonal to the kick. Further reduction in heating may be possible by replacing the single bias coils in our setup with either larger coils or implementation of a calibrated Helmholtz field. Both options would improve the uniformity of the bias field.

6.6 Correcting temperature drifts

In producing the results of Figure 6.7 we addressed the stability of our nozzle over time. Shown in Figure 6.8 is a plot of the data taken during an entire day. We supply a constant heat load to the cyrocooler through ohmic heating in order to maintain the nozzle at a fixed temperature. Despite setting the nozzle to roughly 18 K, long time-scale temperature fluctuations manifest throughout the course of each day. These fluctuations in nozzle temperature are a result of variations in the University's chilled 4.5 °C water supply. This water supply is used to cool the helium compressor unit that, in turn, cools the nozzle. This resulting drift in nozzle temperature correlates to the drift in supersonic beam forward velocity as indicated by the arrival times of the Figure 6.8.

Since the deviation in arrival times of the atoms is small in comparison to propagation time, we can remove the correlation through a linear fit of arrival times as a function the temperature variation of the nozzle. Results of this analysis are shown in Figure 6.9 on the same data set. This was an essential step in order to produce error bars consistent with the variation seen in the data.

As an aside, there are minor features present in our data not addressed in the previous discussions. Some of this can be seen through comparison of data in Figure 6.8 and Figure 6.9. When taking the fluorescence images, we typically scan linearly through the various bias voltages. This sort of behavior is representative of the data that was taken after 19:00 that day. There is a clear dependence on the arrival time even after removing the temperature correlations (seen from examination of a complete bias scan indicated by the colors of Figure 6.8). A possible cause of

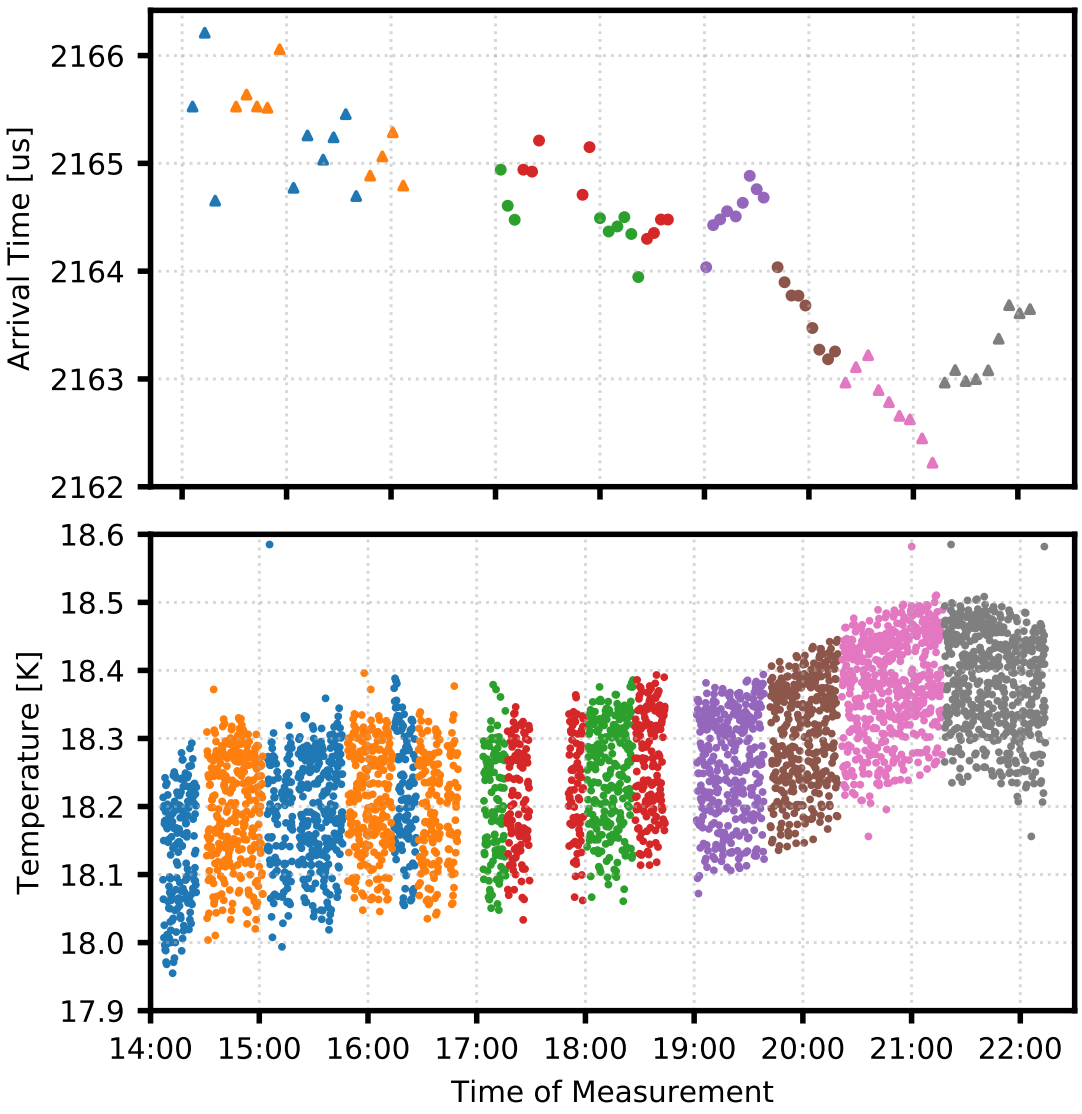

Figure 6.8: Temperature drift of the supersonic nozzle over time. Arrival times shown in the upper plot are averages of the data collected for each bias voltage. Colors indicate the grouping of complete bias voltage scans of different data sets.

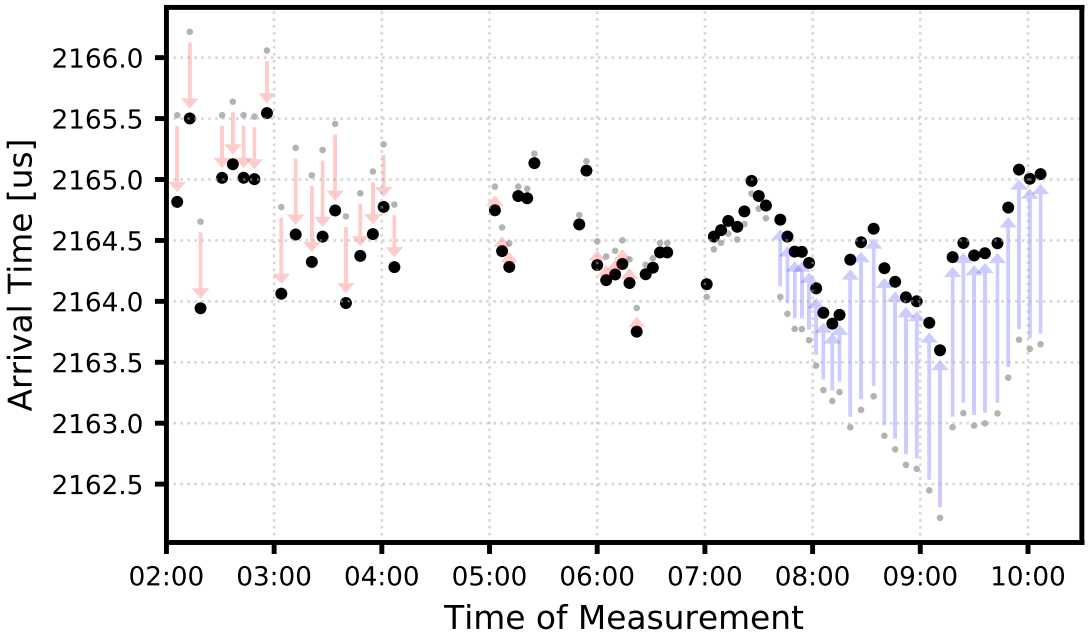

Figure 6.9: Removing time-dependent correlations from the temperature drift data with a linear fit. The corrected data points (bold points) are superimposed on top of the original data.

this correlation is a slight misalignment of the lithium beam axis to the coil axes or inhomogeneities of the beam. This correlation isn't apparent for data sets taken earlier in the day because bias scans were taken non-sequentially.

Chapter 7

The Adiabatic Decelerator and Magneto Optical Cooling

With the successful production of a one-dimensional kick, the experiment is being pushed beyond deflection of atomic beams to ultimate goal of actually stopping, trapping, and cooling lithium for future cold atom experiments. Though not consequential to this work, a large portion of the author's time was spent on another experiment developing a method of slowing atoms to rest through an adiabatic decelerator.

Traditional cold atom experiments use a Zeeman slower (see Figure 7.1) developed to slow atoms directly from an effusive source via a combination of spatially varying magnetic fields and resonant light [38, 44, 46, 55]. The magnetic field shifts the fast moving atoms' resonant frequencies through the Zeeman effect enabling the laser to repeatedly excite the atoms on a closed cycling transition. Through tens of thousands of cycles, the spontaneously emitted photons provide minute momentum kicks ($8.474\,\mathrm{cm/(s \cdot photon)}$ for lithium) to slow the beam to rest. This technique, pioneered by William Phillips [59, 60], has seen widespread use and was a key step towards the experimental realization of Bose-Einstein condensations (BEC). Since the Zeeman slower requires a closed cycling transition, that is, one that excites and

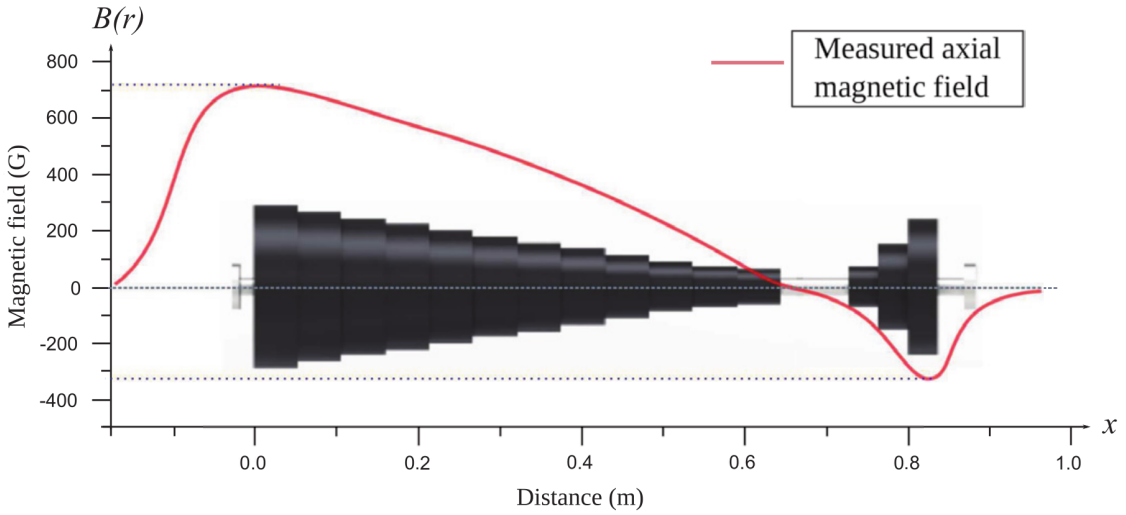

Figure 7.1: Example of a Zeeman slower used in the Bagnato group [61]. A large magnetic field near the left is sufficient to bring the Doppler-shifted fast-moving atoms into resonance with the laser that runs coaxial with the slower. To stay in resonance as the atoms scatter photons and slow, the magnetic field is reduced along the length of the slower.

returns the atom to the original state, only a few elements on the periodic table are amenable to this technique. Complex level structures require multiple lasers at different frequencies to address all the decay channels. Furthermore, atoms are only slowed along the axis of propagation without any confinement for the transverse velocities while within the slower.

Our group has worked on various means of addressing these limitations across several experiments [62]. Specifically, we focused on creating a general slowing method via the atomic coilgun. Rather than rely on the momentum transfer from many photons to an atom, the coilgun instead uses magnetic fields to slow atoms by creating a series of magnetic potential barriers that remove the directional kinetic

energy of the atoms. This technique is inherently more efficient with photons as only a few are needed to transfer the atom into a magnetic state. More importantly, the method is applicable to most atoms on the periodic table since they are either magnetic in their ground state or can be optically pumped into a magnetic metastable state [63]. Furthermore, the technique can even be extended to molecules [64]. Despite the generality of the method, the coilgun, like the Zeeman slower, still suffers from a transverse loss of atoms.

The adiabatic decelerator [65, 66] aims to address this loss and is the evolution of several iterations of the atomic coilgun. Rather than using single coils to generate magnetic potential barriers, the adiabatic decelerator consists of a series of anti-Helmholtz coil pairs that trap and decelerate low-field-seeking atoms to rest. The trap effectively eliminates the transverse loss of atoms and has been recently built and demonstrated in the lab [67].

Our decelerator, shown in Figure 7.2, consists of 480 interleaved anti-Helmholtz coil pairs. By applying timed sinusoidal current pulses generated from circuitry similar to that in subsection 4.4.2 we can effectively shift the trap minimum from one coil pair to the next. By progressively increasing the pulse duration for each subsequent coil pair we can effectively create a decelerating trap. Our group recently showed the deceleration of lithium entrained in a supersonic beam of helium from an initial velocity of 450 m/s to a final velocity of 50 m/s. A summary of the results are shown in Figure 7.3 and additional optimization analyses can be found in [67].

Having successfully slowed lithium atoms we now aim to trap the atoms in a magneto-optical trap (MOT) in order to demonstrate the new technique of magneto-

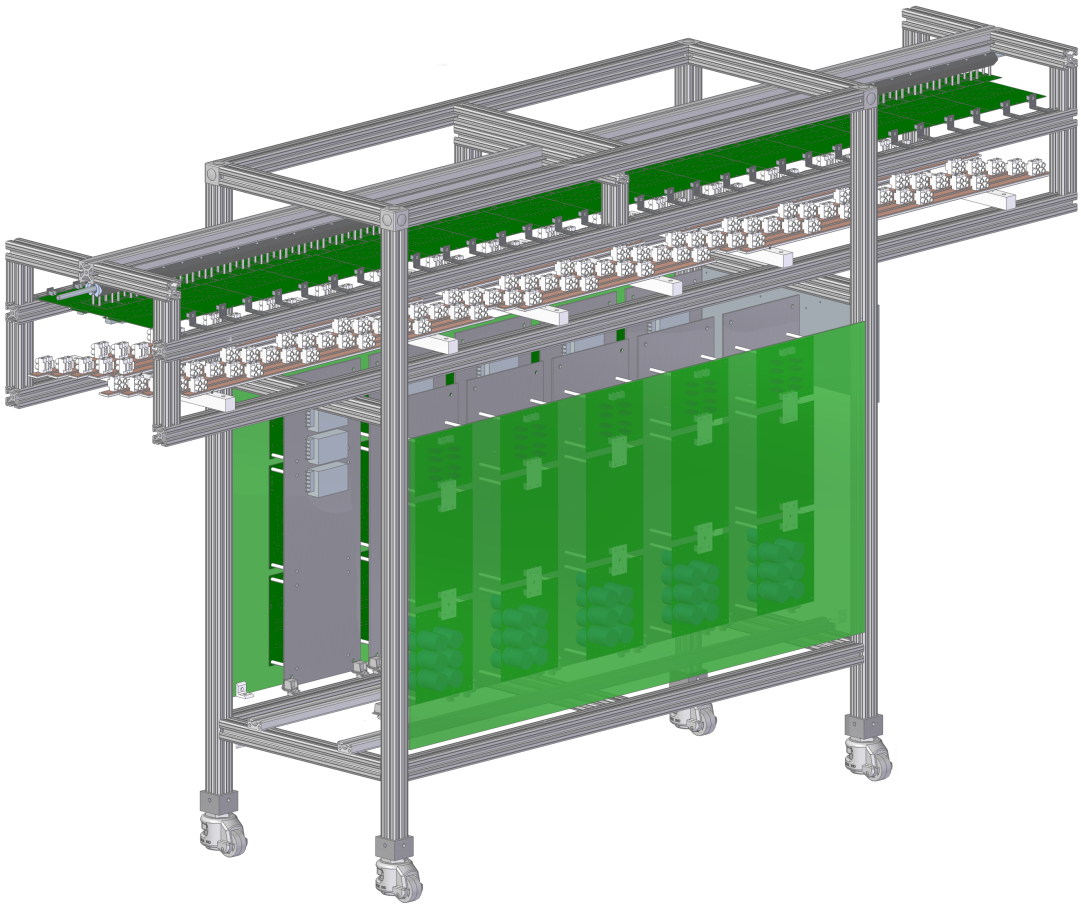

Figure 7.2: Design of the adiabatic decelerator. The decelerator is roughly two meters in length and consists 480 interleaved 1 cm anti-Helmholtz coil pairs that surround a 0.375 in vacuum tube. A series of ten sets of configurable underdamped RLC circuit boards (five for each side) are shared between all the coils. Rotating through each board set provides time for the other four boards to recharge back to $\sim 500\,\mathrm{V}$.

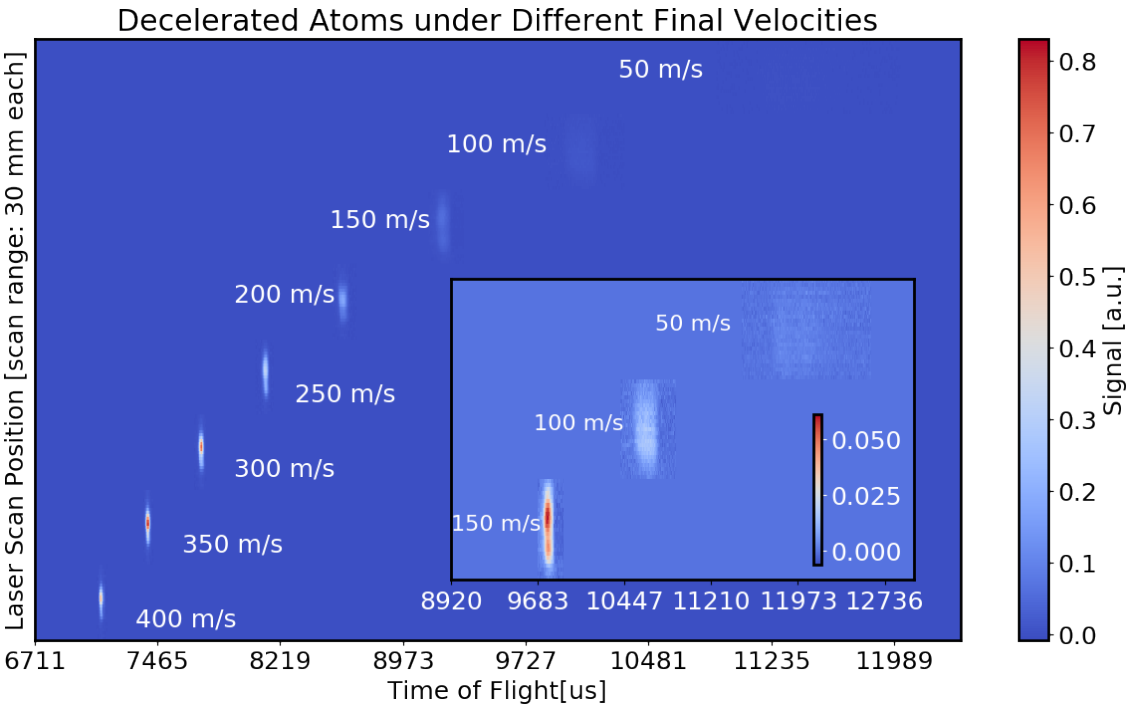

Figure 7.3: Lithium slowing results from the adiabatic decelerator. The initial speed of the lithium beam is 450 m/s. The slower is capable of decelerating the lithium atoms to near rest. Loss of atoms are likely a side effect of the fluorescence measurement occurring several centimeters after the end of the slower after which atoms are allowed to disperse somewhat at the slower velocities. Image is provided courtesy of Yu Lu [67].

optical (MOP) cooling [17] in six-dimensional phase space. Using internal-state optical pumping and stimulated optical transitions combined with one-dimensional kicks we intend to efficiently compress phase space resulting in an ultracold and dense cloud of atoms. The conceptual idea is illustrated in Figure 7.4 for one spatial dimension. Assume a cloud of atoms $\sim 2\,\mathrm{mm}$ that are all in a high-field-seeking state (F=1 for lithium) as indicated by the blue points. We can optically pump half of the spatial distribution into the low-field-seeking state (F=2 for lithium). Using a one-dimensional kick we can apply a force to the two halves in opposite directions in order to merge them. The one-dimensional kick is a necessary ingredient to prevent any heating of the gas (as indicated by the velocity distribution). Once merged a kick of opposite direction is applied to freeze the atoms in their positions. Finally, optical pumping is used to reinitialize all atoms back into the high-field-seeking state in order to repeat the process. This process can not only be applied to all spatial dimensions, but can also be adapted to operate on the velocity components of phase space in a similar manner [17].

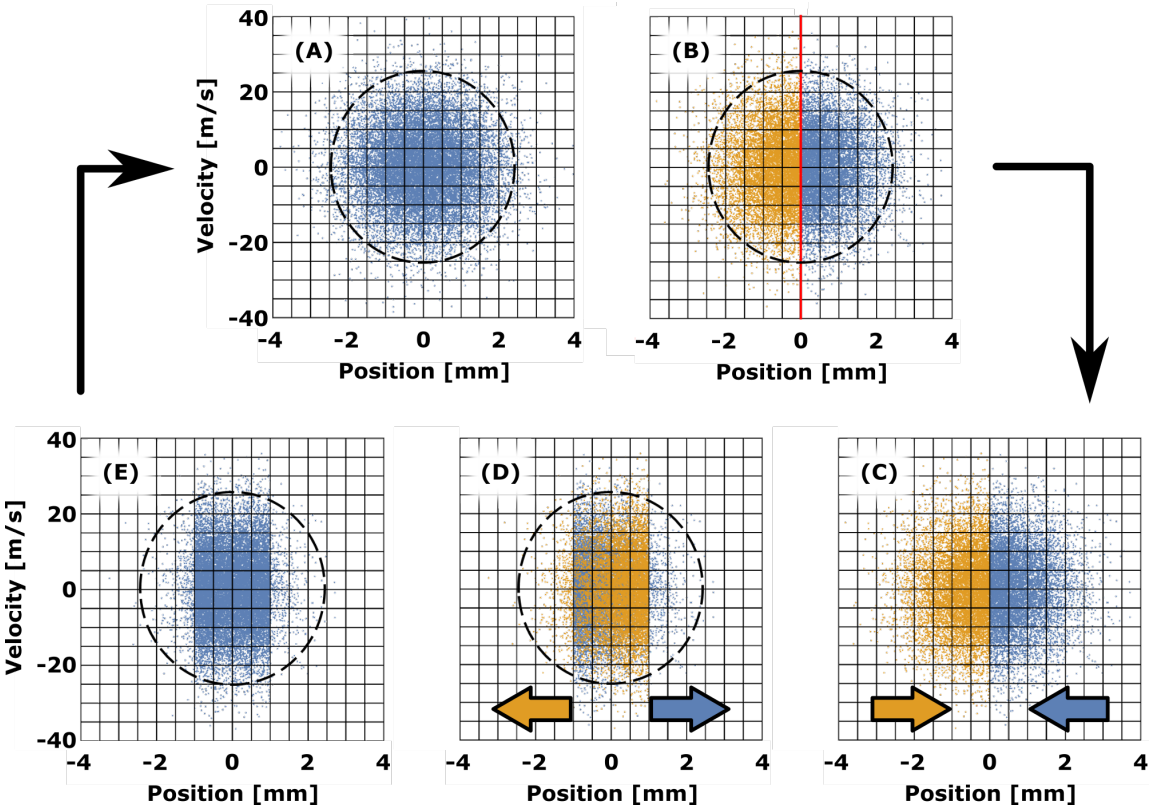

Figure 7.4: Demonstration of the conceptual idea behind magneto-optical cooling. Blue and orange indicate high- and low-field-seeking atoms respectively. (A) Initial distribution of HFS atoms. (B) Half of the spatial distribution is optically pumped into the LFS state. (C) A one-dimensional kick forces the two halves to merge. (D) After the two halves optimally overlap, a reverse kick is a applied to freeze and stop the translational motion. (E) Finally, the entire cloud is reinitialized the HFS state with another cycle of optical pumping. This process can be then repeated to achieve geometric increases in density.

Bibliography

[1] Marlan O. Scully, Willis E. Lamb, and Asim Barut. On the theory of the Stern-Gerlach apparatus. *Found. Phys.*, 17(6):575–583, 1987.

[2] W. Gerlach and O. Stern. Der experimentelle Nachweis des magnetischen Moments des Silberatoms. *Zeitschrift für Phys.*, 8(1):110–111, 1922.

[3] K. S. Melin, P. I. Nagornykh, Y. Lu, L. E. Hillberry, Y. Xu, and M. G. Raizen. Observation of a quasi-one-dimensional variation of the Stern-Gerlach effect. *Phys. Rev. A*, 99:063417, Jun 2019.

[4] T. M. Roach, H. Abele, M. G. Boshier, H. L. Grossman, K. P. Zetie, and E. A. Hinds. Realization of a magnetic mirror for cold atoms. *Phys. Rev. Lett.*, 75(4):629–632, 1995.

[5] K. S. Johnson, M. Drndic, J. H. Thywissen, G. Zabow, R. M. Westervelt, and M. Prentiss. Atomic Deflection Using an Adaptive Microelectromagnet Mirror. *Phys. Rev. Lett.*, 81(6):1137–1141, 1998.

[6] E. A. Hinds and I. G. Hughes. Magnetic atom optics: mirrors, guides, traps, and chips for atoms. *J. Phys. D. Appl. Phys.*, 32(18), 1999.

[7] P. Rosenbusch, B. V. Hall, I. G. Hughes, C. V. Saba, and E. A. Hinds. Manipulation of cold atoms using a corrugated magnetic reflector. *Phys. Rev. A*, 61(3):031404, Feb 2000.

[8] D. Kadio, O. Houde, and L. Pruvost. A concave mirror for cold atoms. *Europhys. Lett.*, 54(4):417–423, May 2001.

[9] Jamie Gardner, Rodrigo Castillo-Garza, and Mark G. Raizen. Note: Manipulation of supersonic atomic beams with static magnetic fields. *J. Chem. Phys.*, 139(9):096103, 2013.

[10] Jamie R. Gardner, Erik M. Anciaux, and Mark G. Raizen. Communication: Neutral atom imaging using a pulsed electromagnetic lens. *J. Chem. Phys.*, 146(8):081102, 2017.

[11] Shimon Machluf, Yonathan Japha, and Ron Folman. Coherent Stern–Gerlach momentum splitting on an atom chip. *Nat. Commun.*, 4(2424):9, Dec 2013.

[12] Yair Margalit, Zhifan Zhou, Or Dobkowski, Yonathan Japha, Daniel Rohrlich, Samuel Moukouri, and Ron Folman. Realization of a complete Stern-Gerlach interferometer. Jan 2018.

[13] Thomas R. Mazur, Bruce Klappauf, and Mark G. Raizen. Demonstration of magnetically activated and guided isotope separation. *Nat. Phys.*, 10(8):601–605, 2014.

[14] Davide Dreon, Leonid A. Sidorenkov, Chayma Bouazza, Wilfried Maineult, Jean Dalibard, and Sylvain Nascimbene. Optical cooling and trapping of highly magnetic atoms: the benefits of a spontaneous spin polarization. *J. Phys. B At. Mol. Opt. Phys.*, 50(6), 2017.

[15] Yuqing Li, Guosheng Feng, Rundong Xu, Xiaofeng Wang, Jizhou Wu, Gang Chen, Xingcan Dai, Jie Ma, Liantuan Xiao, and Suotang Jia. Magnetic levitation for effective loading of cold cesium atoms in a crossed dipole trap. *Phys. Rev. A*, 91(053604):053604, 2015.

[16] Dennis Becker, Maike D Lachmann, Stephan T Seidel, Holger Ahlers, Aline N Dinkelaker, Jens Grosse, Ortwin Hellmig, Hauke Müntinga, Vladimir Schkolnik, Thijs Wendrich, André Wenzlawski, Benjamin Weps, Robin Corgier, Tobias Franz, Naceur Gaaloul, Waldemar Herr, Daniel Lüdtke, Manuel Popp, Sirine Amri, Hannes Duncker, Maik Erbe, Anja Kohfeldt, André Kubelka-Lange, Claus Braxmaier, Eric Charron, Wolfgang Ertmer, Markus Krutzik, Claus Lämmerzahl, Achim Peters, Wolfgang P Schleich, Klaus Sengstock, Reinhold Walser, Andreas Wicht, Patrick Windpassinger, and Ernst M Rasel. Space-borne Bose-Einstein condensation for precision interferometry. *Nature*, 562 (7727):391–395, 2018.

[17] Mark G Raizen, Dmitry Budker, Simon M Rochester, Julia Narevicius, and Edvardas Narevicius. Magneto-optical cooling of atoms. *Opt. Lett.*, 39(15):4502–5, Aug 2014.

[18] Walther Gerlach and Otto Stern. Über die richtungsquantelung im magnetfeld. *Annalen der Physik*, 379(16):673–699, 1924.

[19] Richard P. Feynman. *The Feynman Lectures on Physics*, volume II. Addison-Wesley, 1977.

[20] Preben Alstrøm. Paradox in the classical treatment of the Stern-Gerlach experiment. *Am. J. Phys.*, 50(8):697, 1982.

[21] S. Singh and N.K. Sharma. Comment on "Paradox in the classical treatment of the Stern-Gerlach experiment". *Am. J. Phys.*, 52(1984):274, 1984.

[22] Preben Alstrøm. Concerning S. Singh and N. Sharma: "Comment on 'Paradox in the classical treatment of the Stern-Gerlach experiment"'. *Am. J. Phys.*, 52(3):275, 1984.

[23] Otto Stern. A way towards the experimental examination of spatial quantisation in a magnetic field. *Zeitschrift für Physik D Atoms, Molecules and Clusters*, 10(2):114–116, Jun 1988.

[24] John B. Taylor. Magnetic Moments of the Alkali Metal Atoms. *Phys. Rev.*, 28:576–583, Sep 1926.

[25] P. G. Tait. On the Foundations of the Kinetic Theory of Gasses. II. *Trans. R. Soc. Edinburgh*, 33:251–277, 1887.

[26] L. Boltzmann. Sitzungsber. d. k. akad. d. *Wissensch. zu Wien*, 96(2):1258, 1887.

[27] Paul Rosenberg. Evaluation of Functions Related to Tait's Mean Free Path. *Phys. Rev.*, 61(7-8):528–530, 1942.

[28] Hans Pauly. *Atom, Molecule, and Cluster Beams I*, volume 28 of *Springer Series on Atomic, Optical, and Plasma Physics*. Springer Berlin Heidelberg, Berlin, Heidelberg, 2000.

[29] Norman F. Ramsey. *Molecular Beams*. The International Series of Monographs on Physics. Oxford University Press, 1956.

[30] Wolfgang Christen, Klaus Rademann, and Uzi Even. Supersonic Beams at High Particle Densities: Model Description beyond the Ideal Gas Approximation. *J. Phys. Chem. A*, 114(42):11189–11201, 2010.

[31] J.-S. Wu, S.-Y. Chou, U.-M. Lee, Y.-L. Shao, and Y.-Y. Lian. Parallel DSMC Simulation of a Single Under-Expanded Free Orifice Jet From Transition to Near-Continuum Regime. *J. Fluids Eng.*, 127(6):1161, 2005.

[32] Wolfgang Christen. Stationary flow conditions in pulsed supersonic beams. *J. Chem. Phys.*, 139(15):1–11, 2013.

[33] U. Even. Pulsed Supersonic Beams from High Pressure Source: Simulation Results and Experimental Measurements. *Adv. Chem.*, 2014(Section 3):1–11, 2014.

[34] David S. Weiss, Erling Riis, Yaakov Shevy, P. Jeffrey Ungar, and Steven Chu. Optical molasses and multilevel atoms: experiment. *J. Opt. Soc. Am. B*, 6(11):2072–2083, Nov 1989.

[35] Tomasz M Brzozowski, Maria Maczynska, Michal Zawada, Jerzy Zachorowski, and Wojciech Gawlik. Time-of-flight measurement of the temperature of cold atoms for short trap-probe beam distances. *Journal of Optics B: Quantum and Semiclassical Optics*, 4(1):62–66, Jan 2002.

[36] P. Arora, S. B. Purnapatra, A. Acharya, R. Kumar, and A. Sen Gupta. Measurement of Temperature of Atomic Cloud Using Time-of-Flight Technique. *MAPAN*, 27(1):31–39, Mar 2012.

[37] W. M. Haynes. *CRC handbook of chemistry and physics: A ready-reference book of chemical and physical data*. CRC Press, 99$^{\text{th}}$ edition, 2019.

[38] Christopher J. Foot. *Atomic Physics*. Oxford Master Series in Atomic, Optical and Laser Physics. Oxford University Press, 2006.

[39] Dipankar Das and Vasant Natarajan. Absolute frequency measurement of the lithium D lines: Precise determination of isotope shifts and fine-structure intervals. *Phys. Rev. A*, 75:052508, May 2007.

[40] I.I. Sobel'man. *Introduction to the Theory of Atomic Spectra*. International Series of Monographs in Natural Philosophy. Pergamnon Press, 1972.

[41] J. Walls, R. Ashby, J.J. Clarke, B. Lu, and W.A. van Wijngaarden. Measurement of isotope shifts, fine and hyperfine structure splittings of the lithium d lines. *The European Physical Journal D - Atomic, Molecular, Optical and Plasma Physics*, 22(2):159–162, Feb 2003.

[42] E. Arimondo, M. Inguscio, and P. Violino. Experimental determinations the alkali atoms. *Rev. Mod. Phys.*, 49(1):31, 1977.

[43] A. Corney. *Atomic and Laser Spectroscopy*. Oxford University Press, 2006.

[44] Harold J. Metcalf and Peter van der Straten. *Laser Cooling and Trapping*. Graduate Texts in Contemporary Physics. Springer-Verlag New York, 1999.

[45] G. Breit and I. I. Rabi. Measurement of nuclear spin. *Phys. Rev.*, 38:2082–2083, Dec 1931.

[46] David Medellin. *Towards the creation of high-fidelity Fock states of neutral atoms*. PhD thesis, The University of Texas at Austin, 2013.

[47] Peter W. Milonni and Joseph H. Eberly. *Laser Physics*. Wiley, 2010.

[48] W. I. McAlexander, E. R. I. Abraham, and R. G. Hulet. Radiative lifetime of the $2p$ state of lithium. *Phys. Rev. A*, 54:R5–R8, Jul 1996.

[49] John David Jackson. *Classical Electrodynamics*. Wiley, 3$^{\text{rd}}$ edition, 1999.

[50] T. Bergeman, Gidon Erez, and Harold J. Metcalf. Magnetostatic trapping fields for neutral atoms. *Phys. Rev. A*, 35:1535–1546, Feb 1987.

[51] K. Luria, W. Christen, and U. Even. Generation and propagation of intense supersonic beams. *J. Phys. Chem. A*, 115(25):7362–7367, 2011.

[52] Ruwan Senaratne, Shankari V. Rajagopal, Zachary A. Geiger, Kurt M. Fujiwara, Vyacheslav Lebedev, and David M. Weld. Effusive atomic oven nozzle design using an aligned microcapillary array. *Rev. Sci. Instrum.*, 86(2):1–5, 2015.

[53] John G. King and Jerrold R. Zacharias. Some New Applications and Techniques of Molecular Beams. *Adv. Electron. Electron Phys.*, 8:1–88, 1956.

[54] K. J. Ross and B. Sonntag. High temperature metal atom beam sources. *Rev. Sci. Instrum.*, 66(9):4409–4433, 1995.

[55] Kirsten Viering. *Experiments to Control Atom Number and Phase-Space Density in Cold Gases*. PhD thesis, The University of Texas at Austin, 2012.

[56] Thomas R. Mazur. *Magnetically Activated and Guided Isotope Separation*. Springer Theses. Springer International Publishing, 2016.

[57] G. C. Bjorklund, M. D. Levenson, W. Lenth, and C. Ortiz. Frequency modulation (FM) spectroscopy. *Appl. Phys. B Photophysics Laser Chem.*, 32(3):145–152, 2004.

[58] U. Schünemann, H. Engler, R. Grimm, M. Weidemüller, and M. Zielonkowski. Simple scheme for tunable frequency offset locking of two lasers. *Review of Scientific Instruments*, 70(1):242–243, 1999.

[59] William D. Phillips and Harold Metcalf. Laser deceleration of an atomic beam. *Phys. Rev. Lett.*, 48:596–599, Mar 1982.

[60] The nobel prize in physics 1997. https://www.nobelprize.org/prizes/physics/1997/summary/, 1997. [Online; accessed 24-April-2019].

[61] E. Pedrozo-Peñafiel, F. Vivanco, P. Castilho, R. R. Paiva, K. M. Farias, and V. S. Bagnato. Direct comparison between a two-dimensional magneto-optical trap and a zeeman slower as sources of cold sodium atoms. *Laser Physics Letters*, 13(6):065501, May 2016.

[62] Adam Libson. *General Methods of Controlling Atomic Motion: Experiments with Supersonic Beams as a Source of Cold Atoms.* PhD thesis, The University of Texas at Austin, 2012.

[63] Edvardas Narevicius, Adam Libson, Christian G. Parthey, Isaac Chavez, Julia Narevicius, Uzi Even, and Mark G. Raizen. Stopping Supersonic Beams with a Series of Pulsed Electromagnetic Coils: An Atomic Coilgun. *Phys. Rev. Lett.*, 100:093003, Mar 2008.

[64] Edvardas Narevicius, Adam Libson, Christian G. Parthey, Isaac Chavez, Julia Narevicius, Uzi Even, and Mark G. Raizen. Stopping supersonic oxygen with a series of pulsed electromagnetic coils: A molecular coilgun. *Phys. Rev. A*, 77:051401, May 2008.

[65] Edvardas Narevicius and Mark G. Raizen. Toward Cold Chemistry with Magnetically Decelerated Supersonic Beams. *Chemical Reviews*, 112(9):4879–4889, 2012. PMID: 22827566.

[66] Nitzan Akerman, Michael Karpov, Liron David, Etay Lavert-Ofir, Julia Narevicius, and Edvardas Narevicius. Simultaneous deceleration of atoms and molecules in a supersonic beam. *New Journal of Physics*, 17(6):065015, jun 2015.

[67] Yu Lu. *A Bright Source of Cold Lithium Atoms.* PhD thesis, The University of Texas at Austin, 2019.